FACULTY OF SCIENCE AND TECHNOLOGY

MASTER'S THESIS

Study programme / specialisation: Engineering Structures and Materials - Master's Degree / Structural Engineering	The spring semester, 2023 ~~Open~~ / Confidential
Author: Simen Riise	
Supervisor at UiS: Gerhard Ersdal External supervisor: Mostafa Ahmed Atteya	
Thesis title: Experimental assessment of cracked tubular joints repaired with crack-deflecting holes and weld-toe grinding	
Credits (ECTS): 30	
Keywords: Tubular joints Fatigue cracks Life extension Crack deflecting holes Weld-toe grinding Experimental assessment Numerical analysis Stress concentration factors	Pages: 64 + appendix: 38 Stavanger, 15.06.2023

Acknowledgements

This thesis concludes my Master's degree in Engineering Structures and Materials at the University of Stavanger, Norway. This work would not have been possible without the help and support from several individuals.

First and foremost, I would like to express my gratitude to my supervisors, Professor Gerhard Ersdal and Mostafa Atteya, for the thesis suggestion and all the time they have invested in me and the thesis. Their guidance and advice throughout the course of this work have been of great value to my progress. Moreover, their expertise and feedback have been motivating and facilitated my steep learning curve throughout the work.

Additionally, I want to thank the lab engineers at IMBM for their assistance in the experimental part of the thesis. They go a great distance to support and facilitate in the best possible way for the students. A special thanks go to Swen Romer for the guidance with the instrumentation and Jan-Tore Jakobsen for the assistance with the non-destructive testing.

I would also like to acknowledge RPT-Production's role in fabricating the specimen. Their willingness to support academic research and their outstanding production quality have been crucial to the results and findings in this work.

Finally, I appreciate the contributions of my fellow students and faculty members who offered feedback and assistance during the completion of this thesis.

Abstract

Fatigue-induced cracks in tubular joints represent one of the major threats to the structural integrity of offshore infrastructure. Consequently, developing and researching efficient temporary and permanent repair solutions is essential. Investigation of various technics and methods is ongoing, and the recent advancement in the exploration of crack deflection holes in combination with weld-toe grinding has made a foundation for further investigation of the method.

This thesis investigates the effectiveness of delaying crack propagation in tubular joints subjected to high cycle fatigue with crack-deflecting holes combined with weld-toe grinding. Furthermore, a numerical analysis has been conducted to facilitate a better comprehension of the stress field and stress evolution inherent in the experimental work.

One tubular double T joint was tested experimentally through a three-phased testing scheme. In the initial phase, the specimen underwent cyclic axial loading yielding stresses within the high cycle fatigue regime to the point of achieving a through-thickness crack. The load range throughout the pre-cracking phase was maintained constant with an R-ratio of 0.1. During this phase, an investigation of the stress concentration factor of the intact specimen was also carried out. The next phase of the testing program comprised repairing the cracked specimen by the use of crack-deflecting holes. These crack-deflecting holes were drilled in the crack tip proximity, and the weld toe behind the drilled hole was ground according to DNV-RP-C203 and BS 7608 specifications. In the final testing phase, the performances of the repaired specimen were investigated by subjecting the specimen to further cyclic loading. As the crack induces higher stress concentrations, the load range was reduced to keep the stress levels within the parameters of high cycle fatigue. Upon attaining a clear indication of enhanced fatigue endurance post-repair, the load range was significantly increased to facilitate the examination of subsequent crack initiation and propagation.

In this study, the crack was successfully arrested in the crack-deflecting holes. Furthermore, the repair method indicated an apparent enhancement of the fatigue endurance of cracked tubular joints subjected to stress ranges within the high-cycle fatigue regime. Finally, the recent discovery of reverse coalescence in conjunction with crack initiation after repair with crack deflecting holes was confirmed for both hole reparations in the experimental work. Although a single test is not a proof of anything in fatigue, the results are promising and may justify further investigation.

Table of Contents

Acknowledgements **2**

Abstract **3**

1 Introduction **1**

1.1 Background 1

1.2 Problem Statement 2

1.3 Limitations 2

1.4 Thesis Overview 3

2 Fatigue Analysis of Offshore Structure Tubular Joints **4**

2.1 General 4

2.2 Stress Distribution in Tubular Joints 4

2.3 HSS and SCF Calculation 7

2.4 Fatigue Analysis 11

3 Fatigue Cracks and Repair Methods **18**

3.1 General 18

3.2 Fatigue Cracks in Offshore Structure Tubular Joints 18

3.3 Overview of Repair Methods for Cracked Tubular Joints 19

3.4 Hole Drilling Repair 25

4 Specimen Construction and Fatigue Test Method **29**

4.1 General 29

4.2 DT-Joint Specimen as built 29

4.3 Fatigue Test and Measurement Setup 31

4.4 Fatigue testing of the DT-joint 33

5 Result of Fatigue Test **35**

5.1 Overview 35

5.2 Pre-Cracking Phase 35

5.3 Repair of the Cracked DT-Joint 41

5.4 Performance of the Repaired DT – Joint, First Attempt 44

5.5 Performance of the Repaired DT – Joint, Second attempt 46

6 Evaluation of the Repair's Effectiveness **50**

6.1 General 50

6.2 Repair's Effectiveness First Attempt Based on a Comparison with Existing Tests 50

6.3 Stress Field and Stress Range Analysis 52

6.4 Repair's Effectiveness First Attempt Based Comparison with SN curve 56

6.5 Repair's Effectiveness Second Attempt and Reverse Coalescence 59

7 Conclusion and further work **61**

7.1 Conclusion 61

7.2 Further work 62

8 References **63**

Appendix A Material Properties.....65
Attachment 1 – Tensile Coupon Testing 65
Attachment 2 – Material Certificate 70
Appendix B Specimen Fabrication.....76
Attachment 3 – Fabrication Sheet DT Joint.....76
Attachment 4 – Welding and Fabrication Documentation.....79
Appendix C Calculations.....94
Attachment 5 – Fatigue Life Calculation.....94
Attachment 6 – Burr Diameter Calculation (weld-toe grinding) 99
Attachment 7 – SCF Calculation (DNV RP C203).....100
Appendix D Crack Mapping.....101

Table of Figures

Figure 2-1: Definition of stresses in a welded tubular joint 4
Figure 2-2: The three loading modes in tubular joints, in-plane bending, out-of-plane bending and axial force. 5
Figure 2-3: Strain development near weld toe and linear extrapolation techniques to determine HSS, as illustrated in (Almar-Næss, 1985) 6
Figure 2-4: Illustration of hot spot stress along weld in an axially loaded T-joint, as illustrated in (Waegter, 2009) 7
Figure 2-5: Points for read out of stresses for derivation of hot spot stress in tubular joints (DNV, 2019) 8
Figure 2-6: Classification of simple joints (DNV, 2019) 9
Figure 2-7: Geometrical definitions for tubular joints (DNV, 2019) 10
Figure 2-8: Superposition of stresses with corresponding equations (DNV, 2019) 11
Figure 2-9: S-N curve of material with fatigue limit (a) and without fatigue limit (b) *source (Callister & Rethwisch, 2020)*.....13
Figure 2-10: S-N curves for tubular joints in air and in seawater with cathodic protection (DNV, 2019) 14
Figure 2-11: Illustration of a stress field in front of a crack tip in a large plate, as illustrated in (Lotsberg, 2016) 16
Figure 2-12: Illustration of the three loading modes in fracture mechanics.....16
Figure 2-13: Typical fatigue crack growth curve 17
Figure 3-1: Cause and frequency of damage to fixed offshore structures, *source* (Sharp & Ersdal, 2021) 19
Figure 3-2: Illustration of burr and disc grinding repair of weld, (Braun & Wang, 2021).....20
Figure 3-3: Illustration of weld toe improvement (DNV, 2019) 20
Figure 3-4: Illustration of weld profiling, (DNV, 2019) 20
Figure 3-5: Illustration of a waterproof chamber with an open bottom (Profdivers, n.d.) 22
Figure 3-6: Wet welding (AWS, 2017) 22
Figure 3-7: Grout-filled joint as illustrated in (Sharp & Ersdal, 2021) 22
Figure 3-8: Stressed grout-filled clamp (Trident, 2023).....24
Figure 3-9: Example of doubler plate repair to a jacket structure, *source (Sharp & Ersdal, 2021)*.....25
Figure 3-10: (a) crack, (b) stop hole, (c) crack deflecting hole, (d) crack flack holes 25

Figure 3-11: Specimen geometry (Makabe et al., 2009) 26
Figure 3-12: Schematic representation of the hole arrangement (Makabe et al., 2009) 26
Figure 3-13: Specimen geometry, (Atteya et al., 2020) 27
Figure 3-14: Schematic representation of the hole arrangement (Atteya et al., 2020) 27
Figure 3-15: Cracked tubular joint with stop hole repair (Tubby, 1989) 28
Figure 4-1: DT-joint Geometry *source* (Atteya, to be published) 30
Figure 4-2: DT-joint as built 31
Figure 4-3: Test machine, HPU (MTS, n.d.) and specimen installed in the test system, respectively 31
Figure 4-4: Strain gauge layout at quadrant 1 32
Figure 5-1: SCF at the four quadrants from the experimental work, with ΔP=40 kN. *The SG positioned in saddle-b at Q3 was not measured after installation. Hence, the average SG placement in saddle-b from the other three quadrants is plotted. 36
Figure 5-2: FE model of the intact DT-joint 37
Figure 5-3: Stresses resulting from clamping the specimen in the test rig 38
Figure 5-4: Stress range distribution at strain gauge closest to weld along chord-brace intersection (ΔP=40kN) 38
Figure 5-5: Stress range vs number of cycles. 39
Figure 5-6: Surface crack length vs number of cycles 40
Figure 5-7: Weld scatter at the saddle in Q3 40
Figure 5-8: MPI of the crack in Q3 41
Figure 5-9: Magnetic-based drill 42
Figure 5-10: Carck deflecting holes 42
Figure 5-11: Sanding weld toe 43
Figure 5-12: Weld profile after weld toe repair 43
Figure 5-13: Strain gauge layout in repaired quadrant 43
Figure 5-14: Strain evolution diagram -50˚ hole post-repair testing phase 44
Figure 5-15: Crack propagation into -50˚ hole 45
Figure 5-16: Strain evolution diagram +33˚ hole post-repair testing phase 45
Figure 5-17: Crack propagation into +33˚ hole 45
Figure 5-18: Reverse coalescence phenomena and strain gauge naming 47
Figure 5-19: Crack initiation in front of SG crown-side at +33˚ hole 47
Figure 5-20: Crack initiation in front of SG crown-side at -50˚ hole 48
Figure 5-21: Stress range vs number of cycles post-repair 48
Figure 5-22: Total crack after terminated test 49
Figure 6-1: Standard SN curve and SN curve shifted to pre-crack result 51
Figure 6-2: FE model of the repaired DT-joint, including the crack 52
Figure 6-3: Strain readings from the FE model and SG in the experimental work for different load levels 53
Figure 6-4: FE model of ground weld-toe profile 54
Figure 6-5: Directional strains along paths illustrated in Figure 6-4 54
Figure 6-6: Directional stresses around +33˚ hole 55
Figure 6-7: Time series of the first 930 000 cycles 1st attempt post-repair SG crown-side +33 hole 57
Figure 6-8: Rainflow matrix histogram (w/strain range in μm) of time-series Figure 6-7 57
Figure 6-9: Calculation prosses to estimate the number of cycles in post-repair testing with Δσ = 269 MPa 58
Figure 6-10: Improved SN curve from weld-toe grinding 59
Figure 6-11: Result from testing plotted on standard SN curve 60

List of Tables

Table 1: Thesis Overview....3
Table 2: DT-joint specimen dimension....29
Table 3: Fatigue testing results of the pre-cracking stage....40
Table 4: Repaired specimen fatigue life 1st attempt....46
Table 5: Repaired specimen fatigue life 2nd attempt....49
Table 6: Fatigue life of axially loaded tubular joint without repair....50
Table 7: Summary of the derived stress ranges....56

1 Introduction

1.1 Background

Offshore jacket structures fabricated from steel tubular are widely used as offshore substructures for oil and gas exploration and are also increasingly used as substructures for offshore wind turbines. These fixed structures are exposed to a harsh environment with considerable cyclic wind and wave loadings in a corrosive environment, which can lead to fatigue cracking. Consequently, fatigue is one of the critical design criteria for such structures (Almar-Næss, 1985; Atteya et al., 2021; Ersdal et al., 2019; Lotsberg, 2016)

Although every effort is made in the design stage to avoid fatigue cracking in the offshore structures' service life, this may not be achieved. In addition, numerous offshore installations are ageing and have already passed their design life. Therefore, adequate inspection and repair are vital to maintain safe operating conditions and safely extend the life of the existing offshore structures. In most cases, the repair is difficult and expensive and may result in significant downtime with consequential loss (Tubby, 1989).

An extensive number of repair methods exist, spanning from weld repair to mechanical fixing or removal and replacement of structural elements (Sharp & Ersdal, 2021). A similarity among these techniques is the necessity for heavy equipment, extensive planning, and substantial resource allocation, all of which contribute to high expenditure.

Hence, there is a lack of economically temporary repair methods for tubular joints subjected to fatigue cracks. A well-known temporary repair method for plated structures subjected to fatigue cracks is crack tip holes and crack deflecting holes (Atteya et al., 2020). This method has been used with success in aeronautical industries and bridge engineering. It comprises drilling a through-thickness hole in the crack tip or crack tip proximity to arrest the crack in the hole, thereby reducing the stress intensity at the crack tip. Another cost-effective repair method proven to increase fatigue life is weld toe grinding (Tubby, 1989), which implies profiling the weld toe to reduce the notch stress. The advantage of both these methods is that they do not require heavy equipment and are relatively easy to perform, which means lower costs.

1.2 Problem Statement

Although hole drilling repair has been used with success in aeronautical industries and bridge engineering and is extensively studied in plated structures, it has not yet been proven to be a successful repair method for tubular joints in offshore structures. To the author's knowledge, there is scarce research on the method for welded details and research is limited to two studies.

First, crack-tip holes were studied experimentally in two specimens by (Tubby, 1989), which concluded with restricted benefits of the method. Later, an experimental study by (Atteya, to be published) investigated the effect of crack-deflecting holes and weld-toe grinding. This later work provided valuable insight into the behaviour and stress fields in cracked tubular joints repaired with crack-deflecting holes. However, the study failed to prove a significant increase in fatigue endurance compared to the fatigue life improvement expected from the method.

A critical observation in Atteya's work was that the maximum stresses were identified in an area in front of the weld toe beyond the crack deflecting hole, rather than in the crack deflection hole as normally expected prior to Atteya's work. This was also the location for cracks to reappear after repair in this work. Another observation was that the stress ranges at this location were characterised by high stress and low cycle fatigue. In addition, it can be assumed that significant plastic deformation was present by interpreting the strain evolution diagram from this location. As a result, there still exists a knowledge gap on the effectiveness of the repair in high cycle fatigue conditions. Hence, this thesis aims to:

> *Investigate the effectiveness of crack-deflecting holes combined with weld-toe grinding in delaying crack propagation in cracked tubular joints subjected to high cycle fatigue.*

The study is carried out experimentally and supplemented with numerical analysis to provide a better understanding of the stresses and stress field in the experimental work. In addition, crack initiation and development post-repair is explored.

1.3 Limitations

The experimental work in this thesis is limited to the fatigue test of a single repaired Double T (DT) joint used in offshore jacket structures. The repair comprises a combination of crack-deflecting holes and weld-toe grinding. Lastly, the specimen tested in this study is scaled down compared to tubular joints found in real structures.

1.4 Thesis Overview

A graphical presentation of the thesis is found in Table 1.

Table 1: Thesis Overview

Introduction	**Chapter 1**	**Introduction:**
State of the Art	**Chapter 2**	**Fatigue Analysis of Offshore Structure Tubular Joints:** overview of basic fatigue analysis concepts of offshore structure tubular joints and methods for fatigue analysis.
	Chapter 3	**Fatigue Cracks and Repair Methods:** Review of fatigue cracking in today's offshore industry and well-known repair methods limited to, tubular joints.
Scientific Contribution	**Chapter 4**	**Specimen Construction and Fatigue Test Method:** Description of specimen design, test setup and method, as well as data acquisition system, instrumentation and test monitoring.
	Chapter 5	**Result of Fatigue Test:** Description of the experimental work to test the fatigue life of a tubular joint and a cracked tubular joint repaired with hole drilling and weld toe grinding.
Evaluation, Conclusion	**Chapter 6**	**Evaluation of the Repair's Effectiveness:** Interpretation of the results from the fatigue performance of the repaired cracked joints, supplement with numerical analysis.
	Chapter 7	**Conclusion and further work:**

2 Fatigue Analysis of Offshore Structure Tubular Joints

2.1 General

Three-dimensional frames fabricated from steel tubular are widely used as offshore substructures for oil and gas exploration and are also increasingly used as substructures for offshore wind turbines. These fixed jacket structures are exposed to cyclic wind and wave loads in a corrosive environment, and fatigue is one of the critical design criteria (Atteya et al., 2021).

This chapter presents the basic concepts of fatigue analysis of offshore structure tubular joints, including stress distribution in tubular joints, joint classification, parametric Equation, and well-known methods for fatigue analysis.

2.2 Stress Distribution in Tubular Joints

In fatigue analysis, it is essential to understand the stresses and stress distribution in the particular detail being analysed. The total stresses in a tubular will often be complex with contributions from external forces on the structure, stresses to maintain compatibility between members, stresses arising due to discontinuity at the joint and local stresses at the weld toe (Saini et al., 2016). The total stresses are normally defined as a result of these different stress contributions, as shown in Figure 2-1.

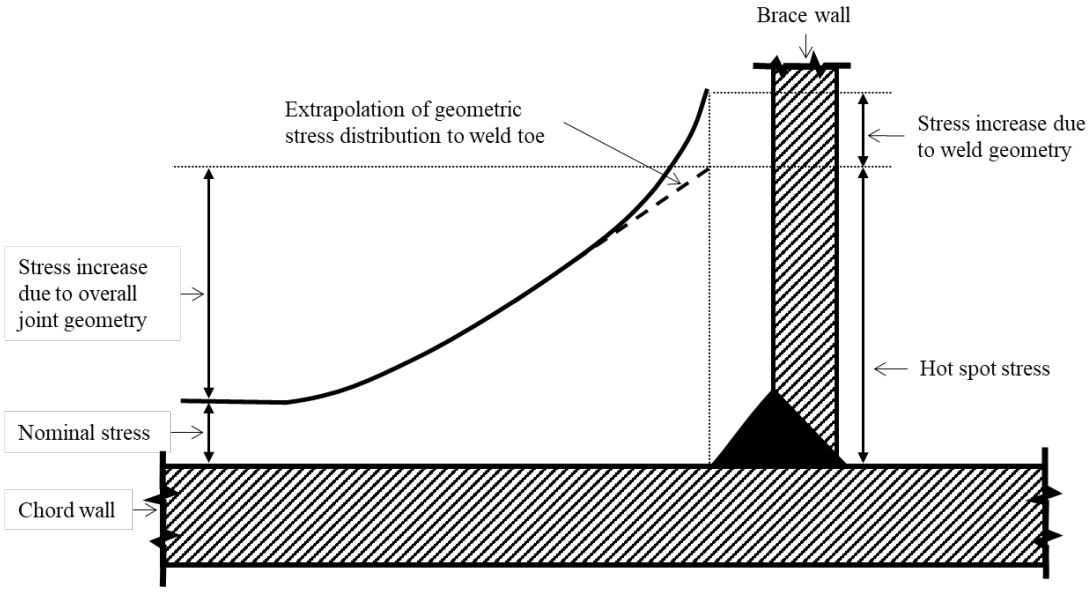

Figure 2-1: Definition of stresses in a welded tubular joint

The source of the stresses developed in a tubular joint is mainly from three different loading modes, axial force, in-plane bending and out-of-pane bending, as shown in Figure 2-2. The different stress concepts are further described in the following section.

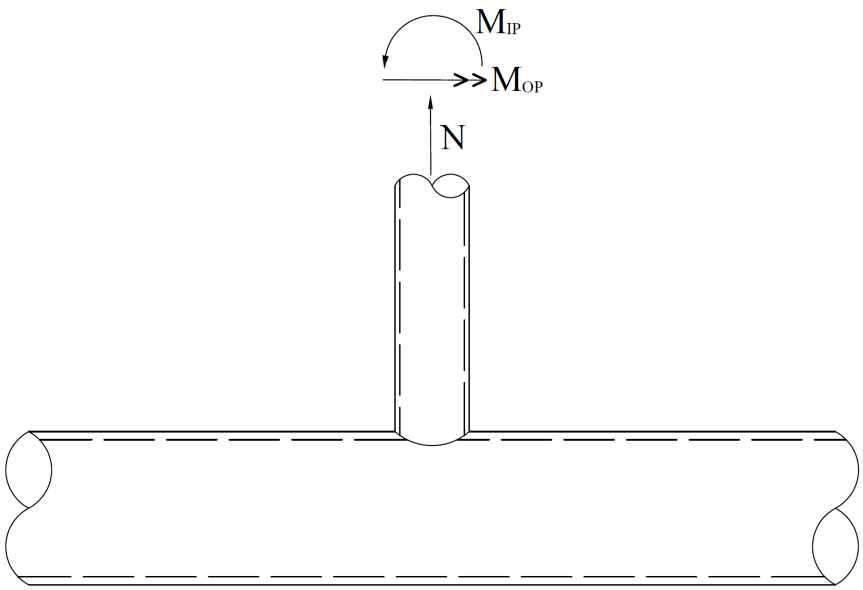

Figure 2-2: The three loading modes in tubular joints, in-plane bending, out-of-plane bending and axial force.

2.2.1 Nominal Stresses

The nominal stresses in a structural member need to be calculated and are useful to determine the local stresses in tubular joints. The nominal stresses can be explained as stresses only due to action loads on the structure without considering any localised stress from weld and geometric discontinuity. It can also be calculated with classical theory, such as simple beam theory combined with the principle of superposition. According to (BS EN ISO, 2007), the structure's nominal stresses and stress variations in fatigue assessment are obtained with an extensive series of global stress analyses with individual periodic waves. The nominal stresses can be expressed as follows in Equation (1):

$$\sigma_n = \frac{N}{A} \pm \frac{M}{I} y \tag{1}$$

Where N is the applied axial force, A is the cross-sectional area, M is the applied bending moment, I is the area moment of inertia, and y is the position of the extreme fibre (Saini et al., 2016).

2.2.2 Hot Spot Stress (HSS)

The hot spot stress HSS often referred to as geometric stress by international standards (BS EN ISO, 2007), is the stress created by the geometric changes in the considered tubular joint. It should be noted that the HSS does not include the local weld notch effect, as further discussed in Section 2.2.3. In more detail, the geometric stresses that arise are due to the difference in relative stiffness between the chord and brace hence different deformation. As the tube wall bends to maintain compatibility, primarily as ovalisation of the chord, extensive bending stresses occur, and the total resulting stresses at the weld toe increase.

In fatigue analysis, the S-N curves for most joints are developed based on the HSS and the excluded notch stress is accounted for by the corresponding HSS S-N (DNV, 2019).

The HSS at a particular weld toe location can also be defined as the nominal stress in the brace multiplied by a corresponding stress concentration factor (SCF), as shown in Equation (2). The procedure to obtain the HSS and SCF is presented in section 2.3.

$$\sigma_{HSS} = SCF \cdot \sigma_{nom} \tag{2}$$

2.2.3 Notch Stress

The local stress at the weld toe, also called notch stresses, is caused by the local notch at the weld toe. In Figure 2-3, the strains close to the weld are illustrated, as shown a rapid non-linear increase in stress occurs very close to the weld toe. This area is referred to as the Notch zone and the localised stress increase is commonly called the local weld notch effect (Saini et al., 2016).

This localised stress occurs at the location of the peak stress in a tubular joint and, therefore, where fatigue cracks are expected to develop. Hence, the fatigue life should ideally be based on the notch stress. However, the last two decades of research have shown that notch stress is heavily influenced by weld geometry and irregularities, which depends on the individual welder's performance at this specific weld. These localised weld shape effects are demanding to quantify and incorporate into the formulation of stress concentration. Therefore the hot spot stress is the industry standard for fatigue life calculation of tubular joints (Waegter, 2009).

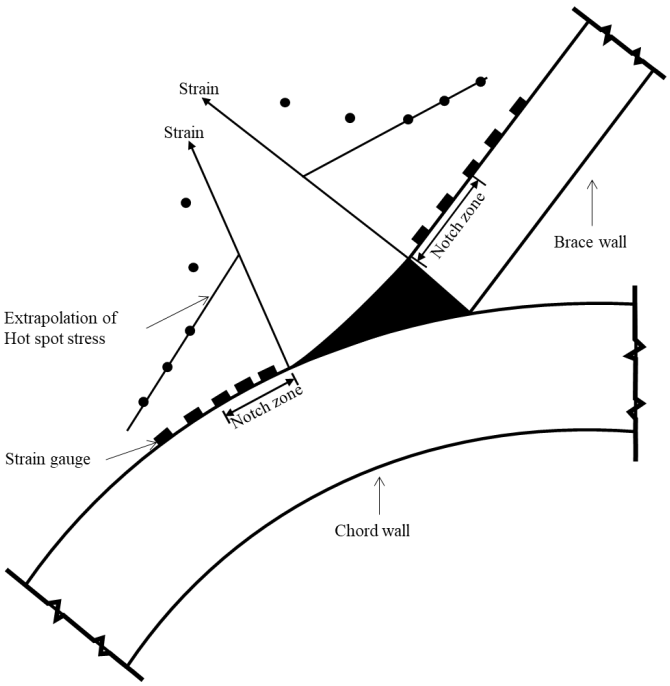

Figure 2-3: Strain development near weld toe and linear extrapolation techniques to determine HSS, as illustrated in (Almar-Næss, 1985)

2.3 HSS and SCF Calculation

2.3.1 General

The three commonly used approaches to calculate the hot spot stress (HSS) are presented in this section and comprise experimental testing, FEM analysis, and parametric equations for simple tubular joints (which include the concept of SCFs). The HSS depend highly on location along the weld, joint geometry, load type and force flow. The stress variation along the weld toe in an axially loaded T-joint is demonstrated in Figure 2-4, which shows an axially loaded T-joint. In the parametric equations, the joint geometry and force flow is accounted for through the concept of joint classification. In addition, different SCF equation is developed for diverse location along the weld and type of loading. The concepts mentioned above will also be further described in the following section.

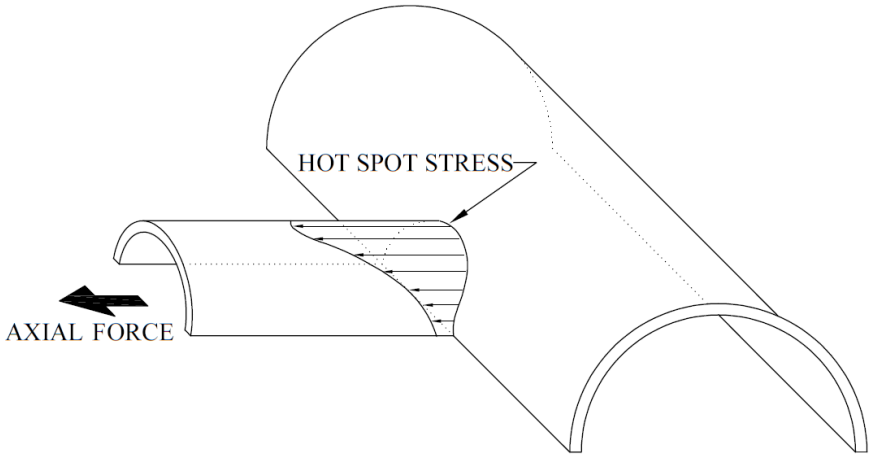

Figure 2-4: Illustration of hot spot stress along weld in an axially loaded T-joint, as illustrated in (Waegter, 2009)

2.3.2 HSS Derivation and Calculation

The hot spot stress HSS is found by extrapolating the maximum principal stresses at positions just outside the notch zone. The linear extrapolation technique is recommended for 90° T and X joints. At the same time, for some joint configurations, such as inclined Y and K joints, there may be a non-linear geometric stress distribution. However, the HSS S-N approach for simple tubular joints is based on linear extrapolation regardless of joint geometry (HSE, 1997).

Figure 2-5 shows the recommended extrapolation positions according to DNV-RP-C203, which can be found with the below Equations (3) to (8). These extrapolation points can be used to position strain gauges in an experimental approach and the points to read the stresses in an FEA approach.

Extrapolation of stress at the crown position along the chord surface normal to the weld toe:

$$a = 0.2\sqrt{rt} \tag{3}$$

$$b = 0.4\sqrt[4]{rtRT} \tag{4}$$

Extrapolation of stress at the saddle position along the chord surface normal to the weld toe:

$$a = 0.2\sqrt{rt} \tag{5}$$

$$b = 2\pi R\frac{5}{360} = \frac{\pi R}{36} \tag{6}$$

Extrapolation of stress along the brace surface normal to the weld toe:

$$a = 0.2\sqrt{rt} \tag{7}$$

$$b = 0.65\sqrt{rt} \tag{8}$$

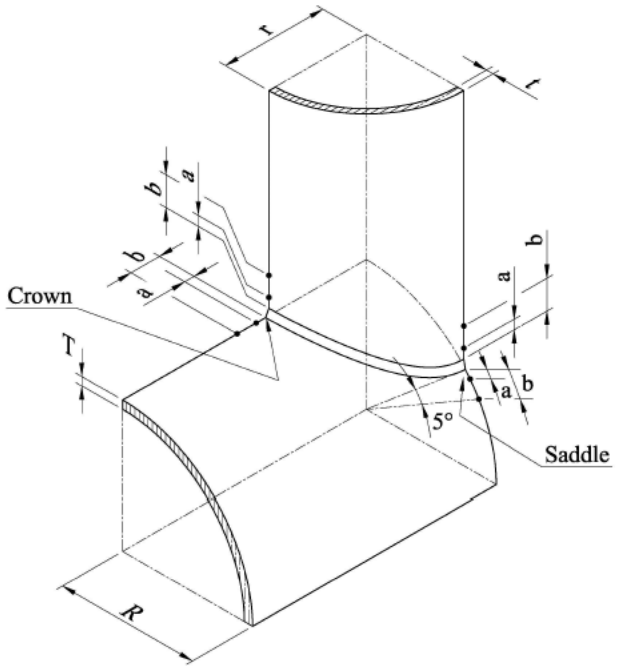

Figure 2-5: Points for read out of stresses for derivation of hot spot stress in tubular joints (DNV, 2019)

2.3.3 Joint Classification

Joint classification of tubular joints is a process where the axial force in each brace is subdivided into X, Y and K components. These three components correspond to the three joint types for which SCF exists. Each brace in each plane is classified as one of the joint types or a mixture of them. Figure 2-6 below shows several simple examples of joint classification (DNV, 2019).

- **X Joint:** The axial force in the brace is carried through the chord and into the brace on the opposite side.
- **Y Joint:** The axial force in the brace is balanced as beam shear in the chord.
- **K Joint:** The axial force in the brace is balanced to within 10% by forces in other braces in the same plane on the same side of the joint.

Essentially the SCF value is an expression of the ovalisation of the chord or local bending of the chord under the action of brace load. As the axial forces in an X-joint act on each side of the chord cross-section, both contributing to the chord's bending and ovalisation, X-joints generally always have the highest SCF. On the other side, the loads in a K joint are mainly carried through the braces, and the chord is only slightly affected. Hence, the following general relationship is stated for joints with equal geometrical properties (DNV, 2019).

$$SCF_X > SCF_Y > SCF_K$$

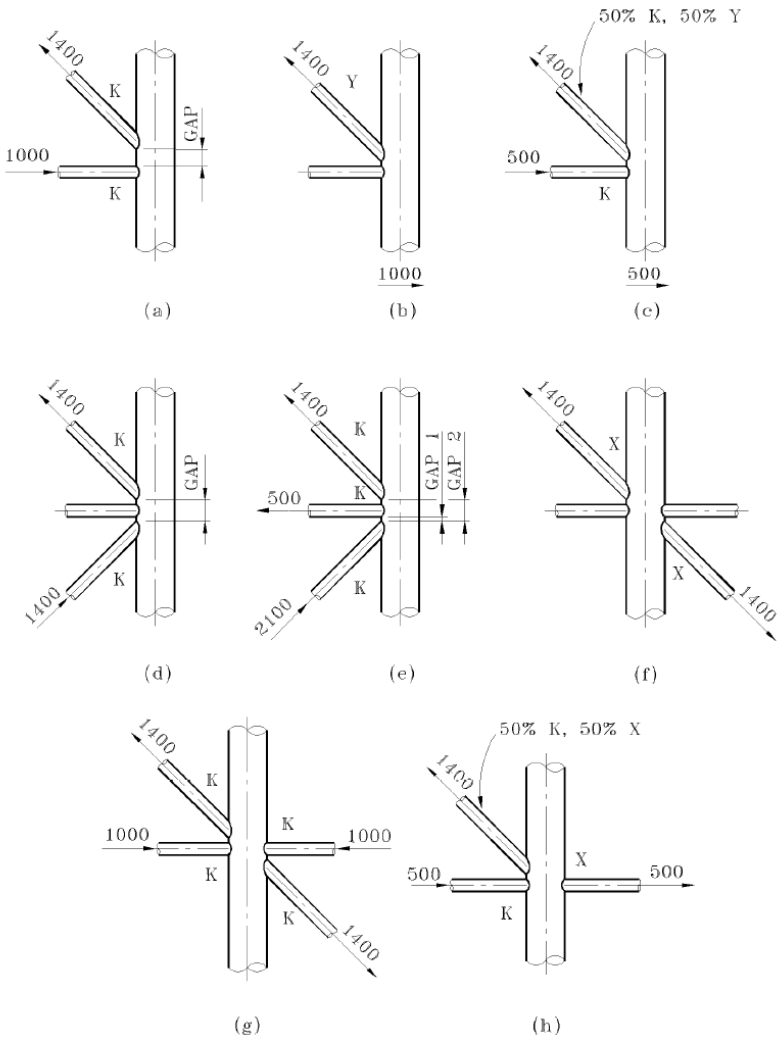

Figure 2-6: Classification of simple joints (DNV, 2019)

2.3.4 SCF Calculation

DNV RP-C204 provides parametric equations for SCF calculation for simple tubular joints based on Mike Efthimiou's work (Efthymiou, 1988). The suitable SCF equation is chosen by first classifying the joint and then determining the non-dimensional parameters shown below. Further, check that they are within the SCF equations' validity ranges shown in Equations (9)-(13). The geometrical properties are shown in Figure 2-7. DNV provide SCF equations for crown and saddle position at both the brace and chord for the three governing load modes axial force, IPB and OPB.

Non-dimensional parameters:

Diameter ratio	$\beta = \frac{d}{D}$
Chord stiffness	$\gamma = \frac{D}{2T}$
Wall thickness ratio	$\tau = \frac{t}{T}$
Chord length parameter	$\alpha = \frac{2L}{D}$

Validity range for the SCF equation provided in DNV-RP-C203:

$$0.2 \leq \beta \leq 1.0 \quad (9)$$

$$0.2 \leq \tau \leq 1.0 \quad (10)$$

$$8 \leq \gamma \leq 32 \quad (11)$$

$$4 \leq \alpha \leq 40 \quad (12)$$

$$20° \leq \theta \leq 90° \quad (13)$$

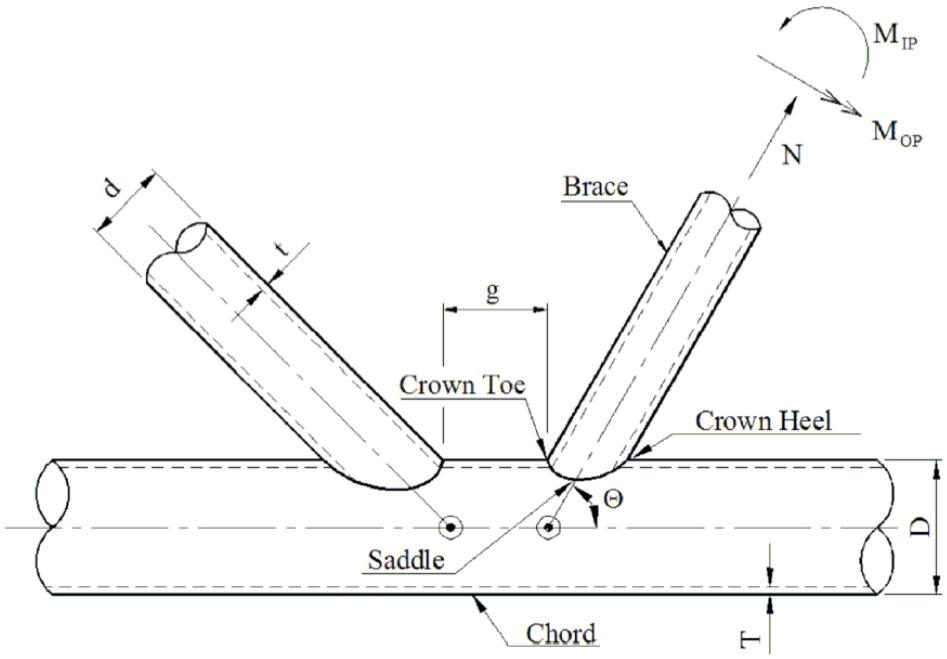

Figure 2-7: Geometrical definitions for tubular joints (DNV, 2019)

For most simple joint geometries and loading, the maximum HSS is located at either the crown or saddle position. However, studies of measured stress around the brace and chord indicate that under IPB combined with axial load, the maximum HSS may be located at an interim position between the crown and saddle position for certain geometries (HSE, 1997). Hence, with the aid of superposition, DNV has developed equations for HSS at eight locations around the circumference of the intersection, as shown in Figure 2-8.

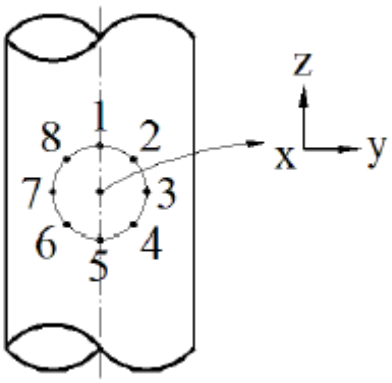

$$\sigma_1 = SCF_{AC}\,\sigma_x + SCF_{MIP}\,\sigma_{my}$$

$$\sigma_2 = \frac{1}{2}(SCF_{AC} + SCF_{AS})\,\sigma_x + \frac{1}{2}\sqrt{2}\,SCF_{MIP}\,\sigma_{my} - \frac{1}{2}\sqrt{2}\,SCF_{MOP}\,\sigma_{mz}$$

$$\sigma_3 = SCF_{AS}\,\sigma_x - SCF_{MOP}\,\sigma_{mz}$$

$$\sigma_4 = \frac{1}{2}(SCF_{AC} + SCF_{AS})\,\sigma_x - \frac{1}{2}\sqrt{2}\,SCF_{MIP}\,\sigma_{my} - \frac{1}{2}\sqrt{2}\,SCF_{MOP}\,\sigma_{mz}$$

$$\sigma_5 = SCF_{AC}\,\sigma_x - SCF_{MIP}\,\sigma_{my}$$

$$\sigma_6 = \frac{1}{2}(SCF_{AC} + SCF_{AS})\,\sigma_x - \frac{1}{2}\sqrt{2}\,SCF_{MIP}\,\sigma_{my} + \frac{1}{2}\sqrt{2}\,SCF_{MOP}\,\sigma_{mz}$$

$$\sigma_7 = SCF_{AS}\,\sigma_x + SCF_{MOP}\,\sigma_{mz}$$

$$\sigma_8 = \frac{1}{2}(SCF_{AC} + SCF_{AS})\,\sigma_x + \frac{1}{2}\sqrt{2}\,SCF_{MIP}\,\sigma_{my} + \frac{1}{2}\sqrt{2}\,SCF_{MOP}\,\sigma_{mz}$$

Figure 2-8: Superposition of stresses with corresponding equations (DNV, 2019)

2.4 Fatigue Analysis

2.4.1 General

Several fatigue analysis approaches exist, such as the Stress-life approach (i.e., S-N curve), the Fracture mechanics approach, the Strain life approach and Simplified fatigue analysis. The following section covers the basic concept of fatigue cracking, the stress life approach, the fracture mechanics approach, and the Palmgren-Miner rule for damage calculation.

2.4.2 The Basic Concept of Fatigue Cracking

In (ASM International Handbook Committee, 1996) fatigue is defined as "the progressive, localized and permanent structural change that occurs in a material subjected to repeated or fluctuating strains at nominal stresses that have values less than (often much less than) the static yield strength of the material." Fatigue may eventually culminate into cracks that may lead to fracture after a sufficient number of fluctuations. Fatigue damage is caused by the simultaneous action of cyclic stress, tensile stress and plastic strain, in which all three needs to be present for fatigue cracks to initiate and propagate (ASM International Handbook Committee, 1996).

The process of fatigue failure can be divided into five stages:

1. Cyclic plastic deformation before fatigue crack initiation
2. Initiation of one or more microcracks
3. Propagation or coalescence of microcracks to form one or more microcracks
4. Propagation of one or more microcracks
5. Final failure

Typically, under usual loading conditions, fatigue cracks initiate near or at singularities on the material surface or just below the surface, such as scratches, pits, inclusions, embrittled grain boundaries or sharp changes in cross-section. Microcracks may also be initially present from welding, heat treatment or mechanical forming, and for welded structural elements, defects will be present from the welding process and the initiation phase (the above stages 1-3) can be ignored or are at least significantly accelerated.

However, a fatigue crack may form even in a flaw-free metal with a polished surface and no stress concentration. If the stress amplitude is high enough, plastic deformation occurs, leading to slip steps and resulting slip lines and planes on the surface. The accumulation of slip steps in a localised region leads to surface roughening and subsequent microcrack initiation. This feature is commonly called intrusions and extrusions, a mechanism described by (Cottrell & Hull, 1957).

After the formation of microcracks, they then grow or coalesce to form one or more microcracks, which eventually grow until the fracture toughness is exceeded and the material fails.

It is important to emphasize that the rate of crack growth and the number of cycles to failure can vary widely depending on the material characteristics, fabrication, loading conditions and the environment to which the material is exposed. In addition, the residual stresses particularly found in welded details, can affect the fatigue endurance. (ASM International Handbook Committee, 1996; BS EN ISO, 2007; HSE, 1999)

2.4.3 S-N Curve

The most common method for fatigue design of welded joints is based on the use of S-N curves. The S-N curve is established on fatigue testing and provides the number of cycles to failure for different stress levels. Numerous S-N curves have been developed for various details and different environments. The characteristic S-N curve used in the design is the mean minus two standard deviation curve, which gives a 97.7% probability of survival, assuming the test data to be normally distributed on a log N scale (Lotsberg, 2016). The basic design S-N curve is given as (DNV, 2019):

$$\log N = \log \overline{a} - m \log \Delta\sigma \tag{14}$$

Where:

- $\Delta\sigma$ = stress range
- N = number of cycles to failure for stress range $\Delta\sigma$
- m = negative inverse slope of S-N curve
- $\log \overline{a}$ = intercept of the design S-N curve with the log N-axis by S-N curve

In Figure 2-9, two distinct S-N behaviours are illustrated. In some ferrous and titanium alloys, as shown in Figure 2-9 (a), the S-N curve reaches a horizontal plateau at higher N values. This indicates the existence of a fatigue limit, also known as the endurance limit, which is the maximum stress level below which fatigue failure does not occur. In contrast to ferrous and titanium alloys, such as those made of iron and titanium, most nonferrous alloys (e.g., aluminium, copper) do not exhibit a fatigue limit. As illustrated in Figure 2-9 (b), the S-N curve continues to decline as the number of cycles increases without reaching a horizontal plateau (Callister & Rethwisch, 2020).

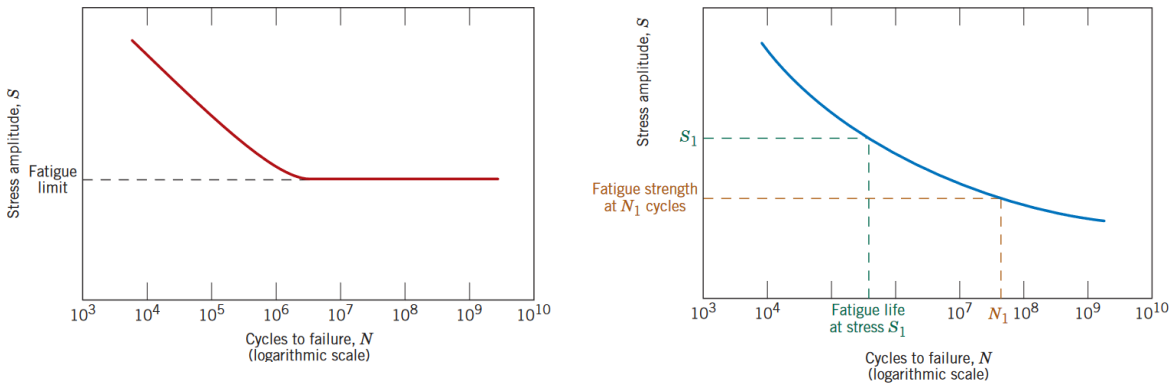

(a) (b)

Figure 2-9: S-N curve of material with fatigue limit (a) and without fatigue limit (b) *source (Callister & Rethwisch, 2020)*

It is developed different concepts of S-N curves. In DNV-RP-C203, three concepts are defined:

- Nominal stress S-N curve
- Hot spot stress S-N curve
- Notch stress S-N curve

In fatigue design of offshore tubular joints, the industry standard recommends the use of the hot spot stress S-N curve called T-curve shown in Figure 2-10. This S-N curve is based on a series of experimental testing of different joint configurations, load modes and stress ranges (HSE, 1999). The T-curve applies to the outside hot spot stress for tubular joints that are welded from both outside and inside as well as only welded from outside. The solid line represents the fatigue life of tubular joints in air, and the dashed lines represent the fatigue life of tubular joints in seawater with and without CP.

Fatigue life based on the S-N curve is, as already mentioned, the preferred approach in the design of offshore structures. However, the method has some limitations. The most significant shortcoming is that it has limitations when being used to assess the integrity of existing structures and it cannot be used in determining the remaining life of structural details where cracks have initiated and are developing. In such cases, the fracture mechanics method is the go-to approach presented in section 2.4.6.

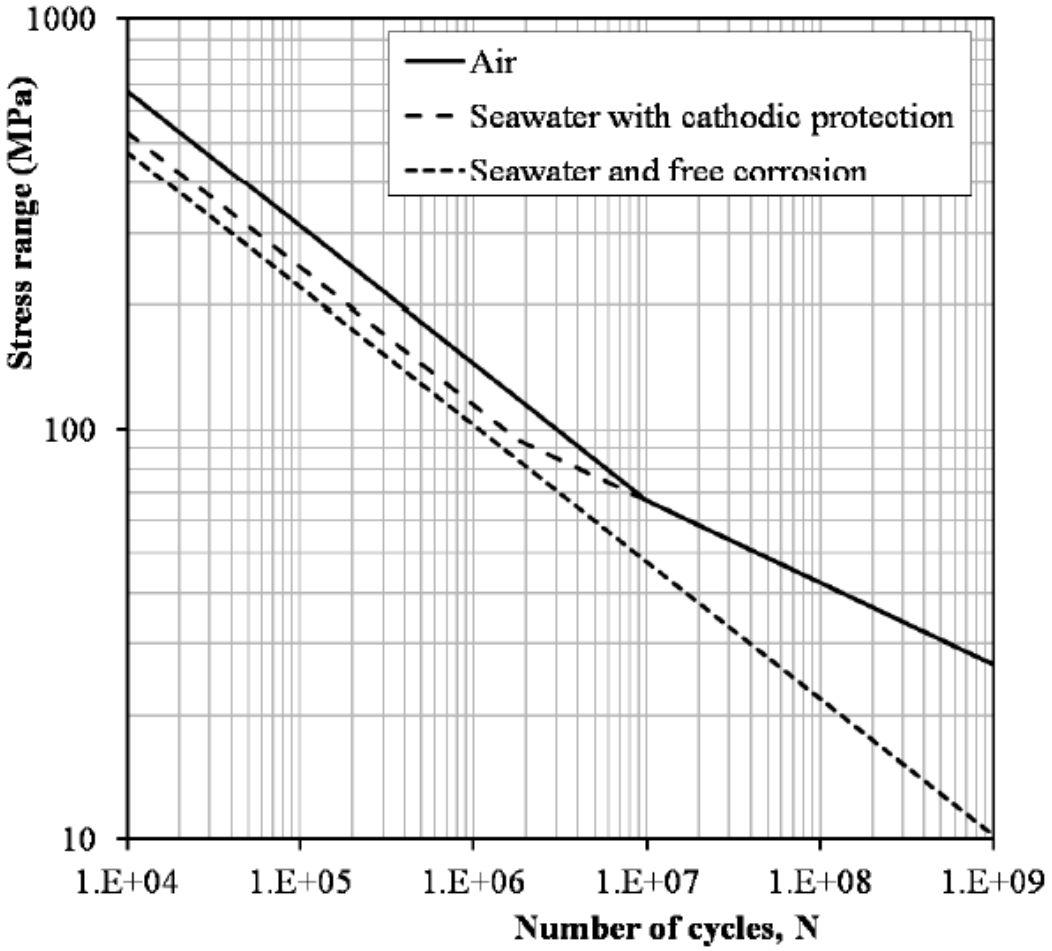

Figure 2-10: S-N curves for tubular joints in air and in seawater with cathodic protection (DNV, 2019)

2.4.4 Damage Calculation with Palmgren – Miners Rule

The S-N curves are primarily developed from experimental testing of specimens subjected to cyclic loading under constant stress amplitude. However, structures in practice are exposed to variable stress amplitudes, particularly offshore structures. The most common approach used for calculating cumulative damage is Miner's summation. The rule assumes that the total accumulated damage is obtained by the linear summation of the damage of each individual stress range, given by Equation(15) (Ersdal et al., 2019):

$$D = \sum_i D_i = \sum_i \frac{n_i}{N_i} \tag{15}$$

Where:

- D = Total cumulative damage
- n_i = number of cycles of constant amplitude stress range $\Delta\sigma_i$
- N_i = Total number of cycles to failure under constant stress amplitude $\Delta\sigma_i$

2.4.5 Low Cycle Fatigue

The S-N curve's low cycle/ height stress range is generally understood as stress ranges corresponding to N<10 000 cycles and is characterised by strain rather than stress (Ersdal et al., 2019). In fatigue assessment of offshore structures, the S-N curve may be linearly extrapolated to fewer cycles. This method is not necessarily conservative, and in cases with high utilisation, the approach described in NORSOK N-006 (Standard Norge, 2015) may be used (DNV, 2019).

In high-cycle fatigue analysis, elastic stresses are calculated in the assessment. In contrast, low cycle fatigue is associated with changes in load direction that cause substantial yielding at the hot spots, also during the load reversal. Hence, to account for the non-linear behaviour of the material in low-cycle fatigue analysis, the calculated strain is often used as a parameter (DNV, 2019).

2.4.6 Fracture Mechanics

Fracture mechanics analysis and its application in fatigue analysis provide a complementary approach to the S-N fatigue life assessment of offshore structures. It is especially useful for assessing ageing structures. In contrast to the S-N approach, it enables the assessment of defects detected during fabrication or in-service inspection. Furthermore, the method offers a clear benefit in that it allows for assessing life extension by analysing the parameters relevant to the phase of extending life. This is achievable due to the method's adaptability in considering the exact geometry and alterations in loading. Consequently, it becomes possible to assess both the severity of the identified defect and the remaining life (Ersdal et al., 2019).

Fracture mechanics aims to define the local conditions of stress and strain around the crack in terms of global parameters of geometry load etc., under which the crack propagates. Various approaches have been utilised in the analysis of fracture mechanics problems, which have led to the introduction of a variety of fracture mechanics parameters, such as J, G, COD and K, all being interrelated. The most popular among these parameters is the stress intensity factor denoted K (Almar-Næss, 1985). Essentially, the stress condition at a crack tip region can be characterised in terms of this single parameter K. The general expression for the stress intensity factor describing the stress field at a through-thickness crack in a plane body with far-field stress normal to the crack 2a is Equation (16) (Lotsberg, 2016):

$$K_g = \sigma\, Y \sqrt{\pi\, a} \tag{16}$$

Where:

- σ = Remote stress as illustrated in Figure 2-11
- a = Half crack length for internal cracks and crack depth for edge cracks
- Y = Geometry function

The geometric function is 1.0 for a through-thickness crack in an infinite body. Otherwise, this function usually is larger than one under tensile load. Normally Y is a function of crack size and is written Y(a). In addition, Y is also a function of crack shape, boundary condition and type of loading.

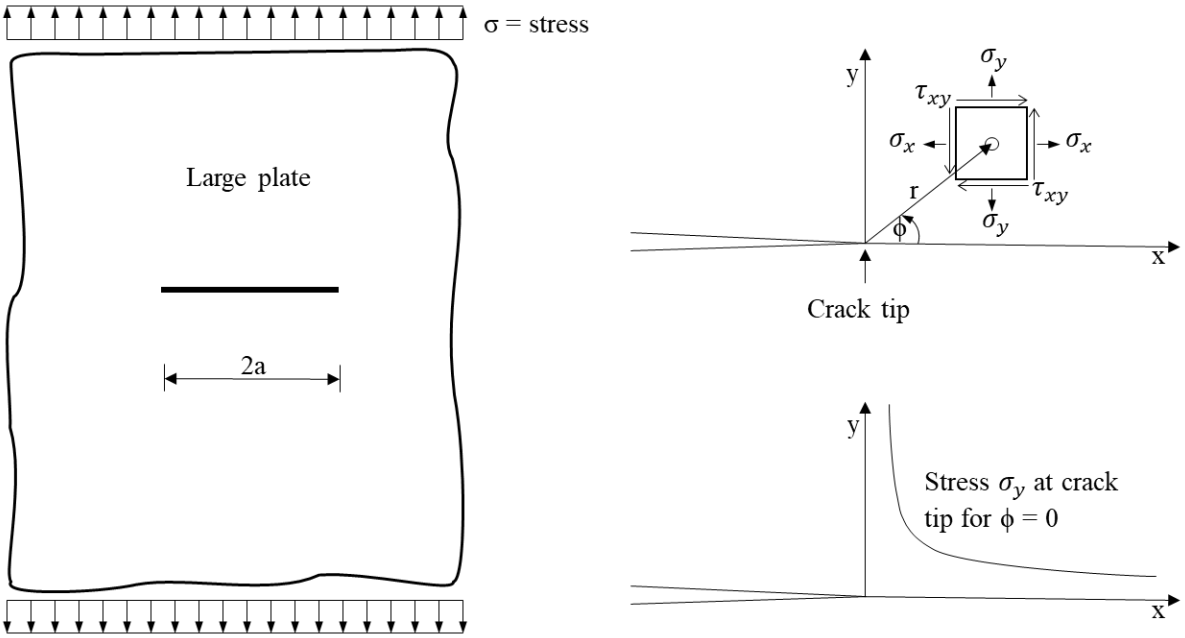

Figure 2-11: Illustration of a stress field in front of a crack tip in a large plate, as illustrated in (Lotsberg, 2016)

Fracture mechanics can be divided into two general categories: liner-elastic (LEFM) and elastic-plastic (EPFM). The basis of LEFM is an analysis of the elastic stress field at the crack tip. A crack in a solid can be stressed in three different modes, as illustrated in Figure 2-12. In fatigue, mode I is the most common and the most important mode in crack growth analysis (Almar-Næss, 1985). The stress intensity at a crack tip subjected to mode I stress is denoted K_I.

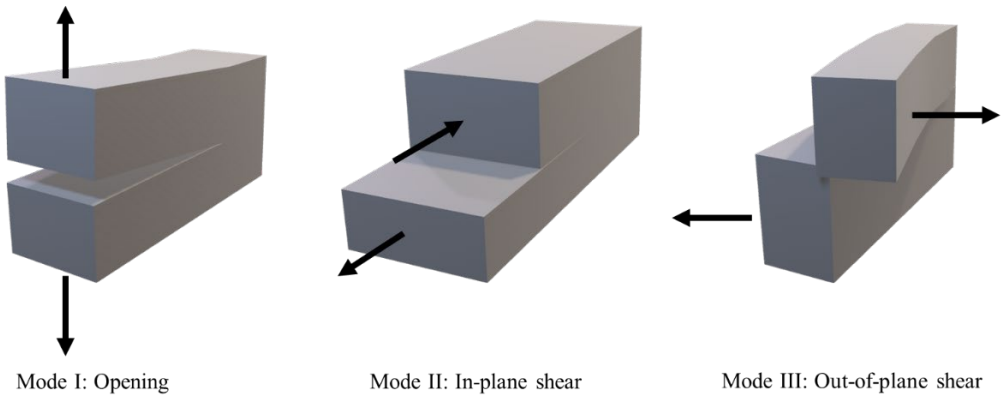

Figure 2-12: Illustration of the three loading modes in fracture mechanics

When a detail experiences cyclic loading and thus is subjected to a stress range $\Delta\sigma = \sigma_{max} - \sigma_{min}$. It can be seen from Equation (16) that this stress range corresponds to a range in stress intensity factor $\Delta K = K_{max} - K_{min}$, which represents the driving force in crack growth. Paris first described the fatigue crack growth rate governed by the range in stress intensity factor, and it is often called the Paris law Equation (17):

$$\frac{da}{dN} = C(\Delta K)^m \quad for \quad \Delta K_{th} \leq \Delta K \leq \Delta K_{mat} \tag{17}$$

Where:

- da = Increments in crack growth for dN stress cycles
- C and m are material parameters
- ΔK_{th} = Threshold value for stress intensity range
- ΔK_{mat} = material fracture toughness

Figure 2-11 illustrates a typical crack growth curve. In region I below the threshold range, crack growth does not appear. On the other hand, as the maximum stress intensity factor approaches the maximum fracture toughness indicated in region III, an unstable fracture may occur. The required number of cycles for an increase in crack length from initial crack size a_o to final crack size a_f can be calculated by integration of the Paris law, as shown in Equation (18):

$$N = \frac{1}{C\Delta\sigma^m}\int_{a_i}^{a_f}\frac{da}{(\pi a)^{m/2}Y(a)^m} \tag{18}$$

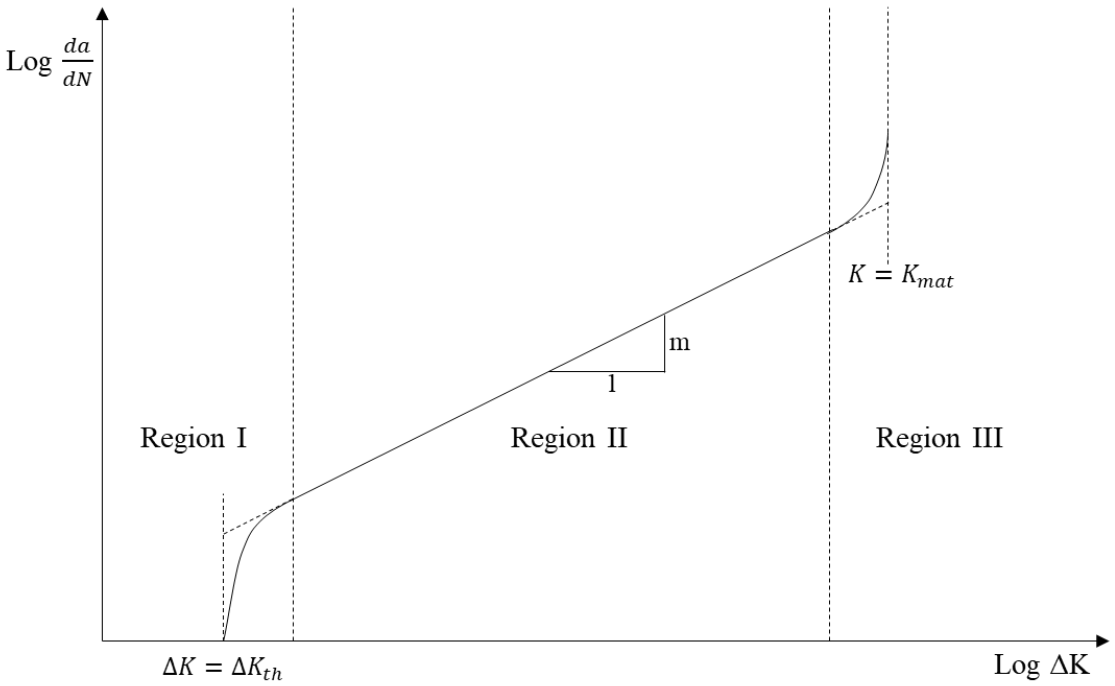

Figure 2-13: Typical fatigue crack growth curve

3 Fatigue Cracks and Repair Methods

3.1 General

Offshore structures are exposed to a harsh environment with considerable cyclic wind and wave loadings, which can lead to fatigue cracking. Although every effort is made in the design stage to avoid fatigue cracking in the offshore structures' service life, this may not be achieved. In addition, numerous offshore installations are ageing and have already passed their design life. Therefore, adequate inspection and repair are vital to ensure safe operation and safely extend the life of the existing offshore structures. This chapter explores the extent of fatigue cracking in today's offshore industry and well-known repair methods limited to the thesis scope, tubular joints.

3.2 Fatigue Cracks in Offshore Structure Tubular Joints

Several inspection reports exist on damage and causes of damage to offshore steel structures. Marine Technology Directorate (MDT) conducted a project in 1989 reviewing records of inspection up to 1984 of platforms installed in the North Sea between 1971 and 1978. In 12 of the platforms, cracks were reported. The most common causes were reported to be direct and indirect design deficiencies, construction deficiencies and accidental events (MTD, 1989; Sharp & Ersdal, 2021).

In 1994 MDT performed one of the first major reviews on damage to fixed offshore structures requiring repair. The report analysed steel and some concrete platforms on the North-West European continental shelf over a period up to 1991. Thirty-nine of the damages requiring repair were related to fatigue, the most frequent number of incidents reported (MTD, 1994; Sharp & Ersdal, 2021).

PMB engineering group conducted a study in the Gulf of Mexico, which included an assessment of damage types resulting from inspections. The study was part of a larger project undertaken by the US Mineral Management Service to develop a methodology to manage the integrity of existing fixed steel platforms reaching the latter stage of their design life. The findings were based on 40 reported incidents representing significant damage (PMB, 1988). Cracks were found to be the dominant damage type. In addition, it was found that fatigue was one of the leading causes to crack formation (Sharp & Ersdal, 2021).

An overview of major structural damages to fixed structures in the UK sector of the North Sea was reported by (Sharp et al., 1995). The information was taken from a database developed by a UK-certified society, containing information on 170 incidents from a review of 174 platforms from 1972 to 1991. The severance, known and suspected through-thickness cracks were included along with several other data. A summary of frequencies and causes of different types of damages recorded in the database is shown in Figure 3-1. As the Figure shows, trough thickness cracks caused by fatigue is the most frequent damage type (Sharp & Ersdal, 2021).

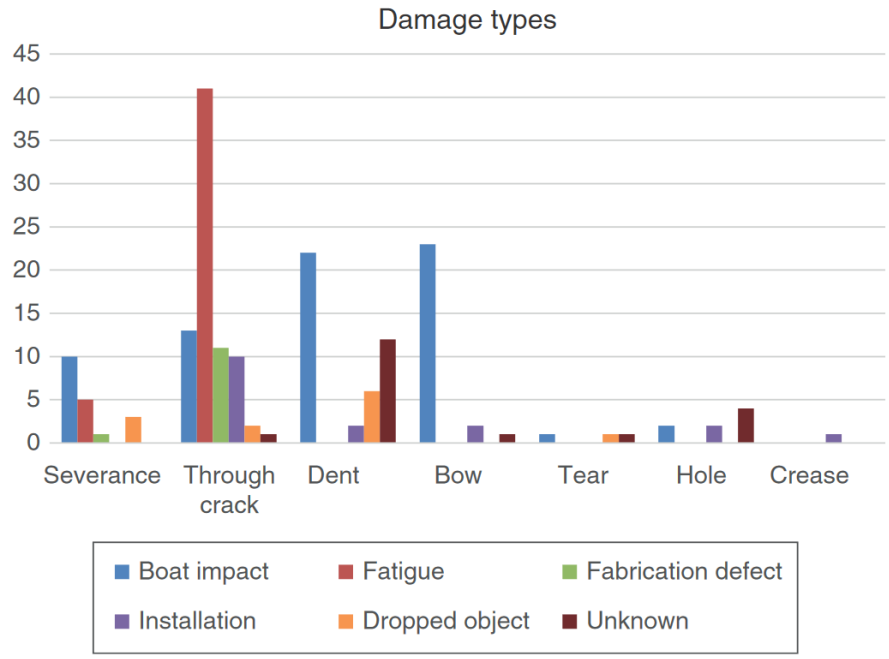

Figure 3-1: Cause and frequency of damage to fixed offshore structures, *source* (Sharp & Ersdal, 2021)

3.3 Overview of Repair Methods for Cracked Tubular Joints

To maintain safe operating conditions, repair of offshore structures is necessary both in the structure's design life and life extension. In most cases, the repair is difficult and expensive and may result in significant downtime with consequential loss. However, this cost is still considerably lower than replacing the structure (Tubby, 1989).

An extensive number of repair methods and many factors need to be considered when choosing an appropriate repair method, which ranges from a basic weld repair to the use of mechanical fixing or removal and replacement of structural elements. The selection of repair method is mainly linked to the damage or anomaly in need of repair and its cause. However, before choosing a suitable repair method, it is necessary to evaluate if repair is needed and the urgency. Based on this evaluation and assessment, a repair method is chosen influenced by damage type, cause, and several other factors. The following section will present common repair methods for cracked tubular joints.

3.3.1 Grinding and Weld Improvement

Machining methods such as burr grinding, disc grinding and water jet gouging are commonly used repair methods for removing fatigue cracks and improving the fatigue strength of welds. With proper grinding, the original life of detail can be more than restored. A rotating burr or disc, as shown in Figure 3-2, is typically used to perform the grinding process. In offshore repair, burr grinders are the preferred method as they are claimed to be easier to use and generally produce better results. The downside is a slower cutting rate compared to disc grinding. The three main methods of weld grinding are weld toe grinding, weld profiling and flush grinding of weld cap, where the two first methods are used in tubular joint repair and fatigue improvement.

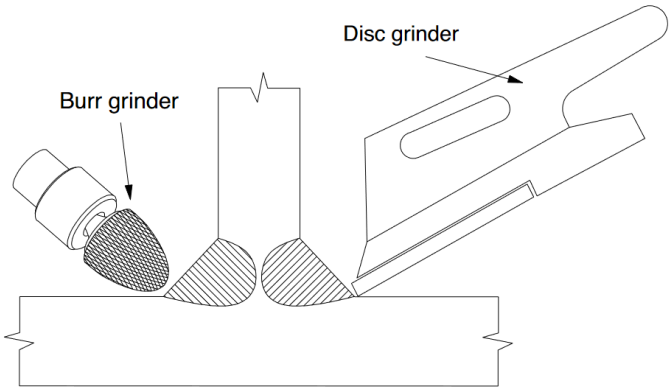

Figure 3-2: Illustration of burr and disc grinding repair of weld, (Braun & Wang, 2021)

Weld toe grinding is performed by local grinding of the weld toes below any visible undercut. Figure 3-3 illustrates two weld toe improvements, A and B. Grinding the weld toe tangentially to the plate surface, as shown in A, will only slightly improve fatigue endurance. As shown in B, a more efficient improvement is achieved by grinding below the plate surface. The ground concave profile should be 0.5 mm below the bottom of any visible undercut, but not exceed 2 mm or 7% of the plate thickness (DNV, 2019).

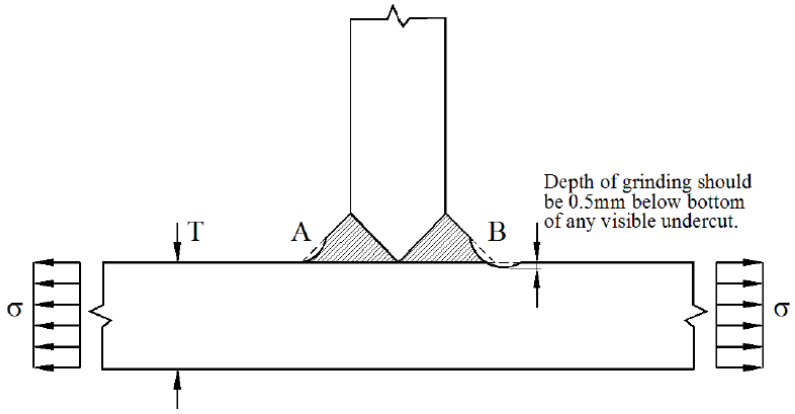

Figure 3-3: Illustration of weld toe improvement (DNV, 2019)

Weld profiling is a method for increasing fatigue strength and is accomplished by machining the weld with a given radius, as shown in Figure 3-4. The method is unsuitable for fatigue crack repair but can be combined with weld toe grinding and weld repair.

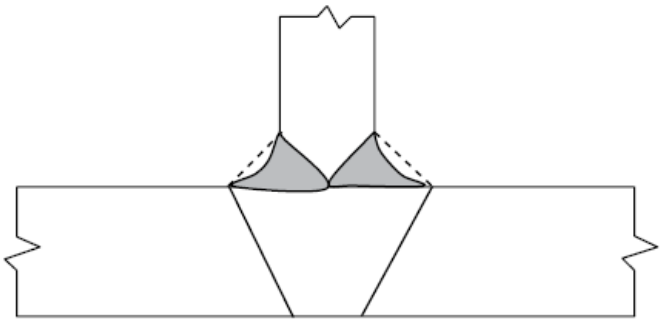

Figure 3-4: Illustration of weld profiling, (DNV, 2019)

Another well-known approach to improve the fatigue strength of a weld detail is by reducing tensile residual stresses with peening. There exist different peening methods. However, the basic principle is the same: deforming the weld toe plastically to introduce compressive residual stresses in the material surface. The weakness to consider with the following method is that the compressive stresses may be reduced or disappear if the detail is subjected to a compressive overload (Sharp & Ersdal, 2021).

3.3.2 Stop Holes and Crack Deflecting Holes

Stop-hole drilling is a widely used method to prevent existing cracks from further developing and is believed to be an efficient method for arresting non-fatigue cracks. However, for fatigue crack arrest, research has shown somewhat mixed benefits of the method (Tubby, 1989). The stop hole is typically drilled at the crack tip, and the principal is to reduce the stress intensity at the crack tip by transforming the tip into a blunt notch. The stop holes and crack deflecting holes method is further elaborated in section 3.4.

3.3.3 Weld Repair

Welding provides the possibility of fixing cracks or adding components or attachments. In addition to grinding, repair welding is a frequently utilised method for removing fatigue cracks and can be classified into four categories:

- **Welding under dry atmospheric pressure** is a widely used repair method commonly used in ship-shaped and semi-submersible structures. Additionally, it can also be used above the splash zone in fixed structures and in and below the splash zone with the use of a cofferdam.
- **Welding under dry hyperbaric pressure** is usually carried out using a waterproof chamber with open bottom, as shown in Figure 3-5. The chambers are custom-made for the specific project, and a gas at the same pressure as the surrounding seawater is admitted pushing water out of the chamber. Hence, welding is performed in a dry environment but with higher pressure. This higher pressure may substantially influence the performance of the weld proses. Therefore, specialised welding procedures should be developed for this method.
- **Wet welding,** as shown in Figure 3-6, is conducted in direct contact with water, making it a cheaper alternative to dry welding under hyperbaric pressure, as there is no need to build a habitat. However, the weld quality is significantly worse compared to a corresponding weld under dry atmospheric pressure. This is mainly due to the rapid cooling rate that occurs in the weld metal, which leads to a brittle structure in the weld and heat-affected zone (HAZ). In addition, the weld interaction with water leads to a hydrogen-rich environment. The hydrogen that has not dissipated may be abundant enough to cause cracking in the weld metal or HAZ.

- **Friction welding** can be used to apply studs and attachments. The method is carried out by rotating a stud at high speed while pressure is applied to force the stud onto the metal surface. The friction between the stud and the metal surface causes the surfaces to heat and plastically displace and fuse the materials. Friction welding underwater may produce a poorer result due to the rapid cooling of the weld. However, it has been found possible to achieve an acceptable weld with the aid of a polymer sleeve to protect the weld from the surrounding.

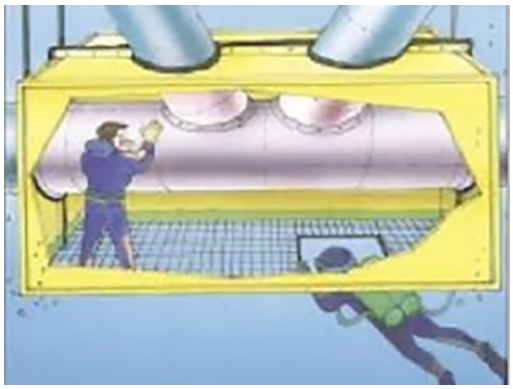

Figure 3-5: Illustration of a waterproof chamber with an open bottom (Profdivers, n.d.)

Figure 3-6: Wet welding (AWS, 2017)

3.3.4 Member and Nodal Strengthening

Member and nodal strengthening in fixed offshore steel structures are generally achieved with clamps and sleeves or grout filling of tubular joints. Grout filling is performed by filling the chord with grout, as shown in Figure 3-7. This strengthens the wall and reduces local bending and deformation of the cross-section, leading to increased capacity against both fatigue and static stress. Grout significantly reduces stress caused by axial and out-of-plane bending, lowering the stress concentration factors around the brace-to-chord weld intersection. Failure modes of grout-stiffened nodes remain unchanged compared to conventional nodes. (Sharp & Ersdal, 2021)

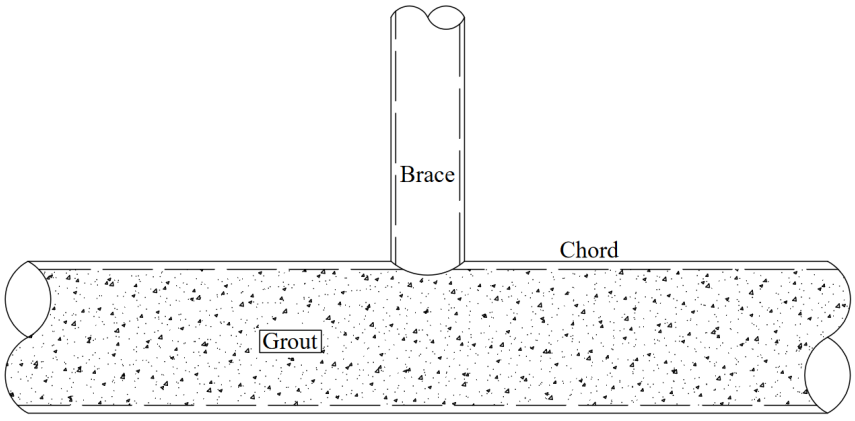

Figure 3-7: Grout-filled joint as illustrated in (Sharp & Ersdal, 2021)

Clamps and sleeves are primarily used to repair or reinforce tubular members or joints in a fixed offshore steel structure. The clamp provides an alternative load path by transferring loads and stresses from a damaged or weakened area of the structure to itself. The sleeve works similarly, surrounding and connecting to the tubular member to provide a parallel load path. A tight connection between the clamp or sleeve and the original steelwork is crucial for effective stress transfer. This can be achieved through various means, such as friction, grout, or an elastic membrane (e.g. neoprene) filling the interface. Additionally, the stress transfer can be optimised by stressing the clamp or sleeve directly onto the tubular section with long stud bolts.

Various clamp and sleeve technologies exist, differentiated by their load transfer techniques and the level of geometric tolerance required for compatibility with the existing structural element. Some of the most prevalent types include:

- **Mechanical friction clamps (prestressed clamps)** consist of two or more segments held together by bolts to provide the load path. The outer segments must have precise tolerances to fit the existing structure, and the friction between the two steel surfaces affects the repair's strength. These clamps are used to reinforce brace members (static strength and fatigue strength) and connect members at an angle to an existing structure. However, they are often not suitable for joint repairs due to the complex geometry and strict tolerances required.
- **Grout-filled clamps (split sleeve clamps)** are clamps in which the split sleeves are closed by pre-tightened bolts, leaving a circular space between the existing structure and the clamp for grout injection. The use of grout reduces the need for strict tolerances. Grout-filled clamps transfer loads from the existing structure to the clamp through grout by shear and compression. Weld beads can increase the shear capacity but require underwater welding. Filling the clamp with grout is a standard underwater operation but may require large-scale testing to verify the execution. Insufficient filling has been noted in decommissioned clamps, stressing the importance of a verified grout-filling method to ensure sufficient quality of the repair. Grouted clamps are weaker than mechanical friction clamps and often need to be longer to achieve sufficient capacity.
- **Stressed grout-filled clamps (prestressed grouted clamps),** as shown in Figure 3-8, are similar to unstressed grout-filled clamps but with added external stress applied by tightening the bolts. Thus, the advantages of both friction clamps and unstressed grouted clamps are provided in load-bearing capacity. In addition, the tolerance requirements are less strict compared to friction clamps. This type of clamp has been used successfully on the Norwegian continental shelf.
- **Stressed neoprene-lined clamps (prestressed lined clamps)** are similar to mechanical friction clamps but with an added layer of elastomer material, such as neoprene, between the clamp and the structure. The bolt loads and the friction between the elastomer and steel determine the strength. This type of clamp requires less strict tolerance compared to mechanical friction clamps. (Sharp & Ersdal, 2021)

Figure 3-8: Stressed grout-filled clamp (Trident, 2023)

3.3.5 Removal and Installation of New Structural Elements

Sometimes, the preferred repair method may be removing or adding structural elements. Advanced analysis techniques have enabled the identification of members that can be removed instead of repaired. The purpose behind this approach can be classified into three main categories:

- Avoid local stress concentration by removing secondary elements
- Change local or global load effects by removing structural elements or part of structural elements
- Replacing a structural element by removing it and installing a new one.

Removing and replacing a structural element can be an effective modification. An example is seen at the Norwegian shelf, where a jacket structure had a cracked tubular joint fixed by removing the original brace and installing a new one using clamps. Cutting techniques used to remove the member include mechanical (cutter, wire saw, etc.), thermal (oxy-acetylene, etc.), explosive, and electrochemical cutting.

Introducing new structural elements can also be an effective repair method. An example of such repair may be adding braces to increase the strength of a jacket facing increased wave forces. The braces can be attached by welding above water and clamps below water (Sharp & Ersdal, 2021).

3.3.6 Doubler Plates

Doubler plates can be used to efficiently reinforce a structure by increasing its thickness, but a design analysis is required to ensure effective load-carrying. This repair method is also used in fixed steel offshore structures, as shown in Figure 3-9 (Sharp & Ersdal, 2021).

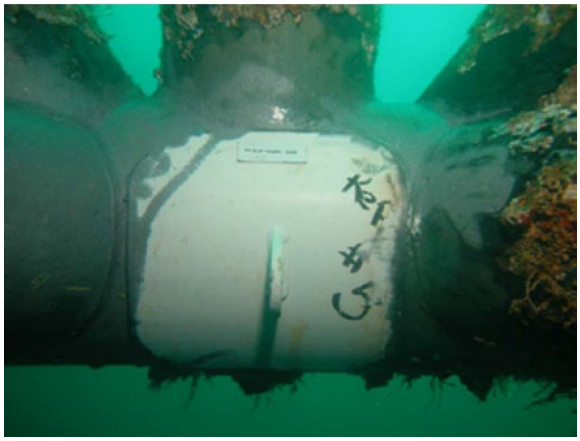

Figure 3-9: Example of doubler plate repair to a jacket structure, *source (Sharp & Ersdal, 2021)*

3.4 Hole Drilling Repair

Hole drilling repair is a relatively simple and cost-effective repair method for crack arresting. The method is primarily intended as a temporary measure and is used in various structures and industries, such as aircraft, bridges, ships, and fixed and floating offshore structures. The method can be divided into three main categories (Atteya et al., 2020):

- **Stop holes** drilled at the crack tip to remove stress intensity at the crack tip.
- **Deflecting holes** drilled in an area close to the crack tip to redirect the crack path, as shown in Figure 3-10.
- **Crack flack holes** by drilling two holes symmetrically relative to the crack plane, intended to reduce the stress intensity factor, as shown in Figure 3-10.

Hole size and position play an essential role in the effectiveness of the repair. In addition, the method can be improved by introducing compressive stresses in the hole.

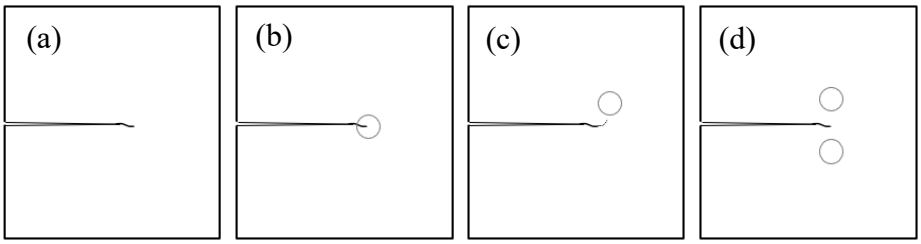

Figure 3-10: (a) crack, (b) stop hole, (c) crack deflecting hole, (d) crack flack holes

3.4.1 Stop Holes

A stop hole may be drilled at the crack tip to stop or impede further crack growth as a result of cyclic loading. Stop holes should be placed such that the crack tip is removed, as shown in Figure 3-10, or if there is uncertainty regarding the crack tip position, the hole can be placed in front of the visible crack tip. A properly placed hole removes the stress intensity at the crack tip. However, the hole itself introduces a significant stress concentration. The SCF resulting from a hole located at the end of an internal crack can be calculated with the following Equation (19) (Lotsberg, 2016):

$$SCF = 1 + 2\sqrt{\frac{a}{r}} \tag{19}$$

Where a is half crack length and r is the hole's radius. From Equation (19), it can be seen that large cracks require large holes to ensure a reasonably low SCF. In general, larger holes are better if the overall strength and stiffness of the structural component are not compromised.

3.4.2 Crack Deflecting Holes

Several studies have proven crack-deflecting holes to be an effective repair method to retard crack propagation due to cyclic loading (Atteya et al., 2020) (Makabe et al., 2009). An experimental study by Makabe in 2008 explored how compressive residual stress can prevent the growth of fatigue cracks using a double-edge-pre-cracked specimen that featured holes. The specimen geometry is shown in Figure 3-11, and a schematic representation of the hole arrangement is shown in Figure 3-12. The three main results obtained from the study were as follows:

- Inserting pins into holes could arrest the growth of fatigue cracks, as the residual stress was distributed along the crack's path and in the area surrounding the holes.
- In the experimental conditions, the arrest of crack growth was influenced by the horizontal distance to the hole, denoted as x. Greater distance x resulted in a higher degree of crack growth arrest.
- Preventing the coalescence of multiple cracks was achievable by drilling holes and inserting pins into them, which reoriented the direction of the crack growth.

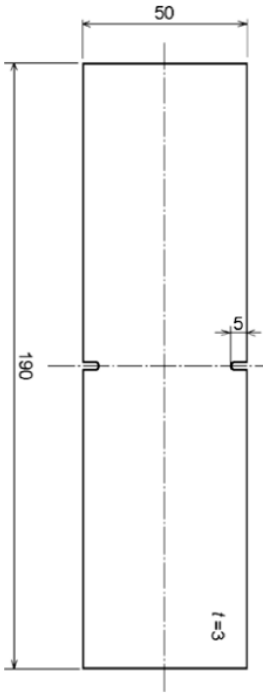

Figure 3-11: Specimen geometry (Makabe et al., 2009)

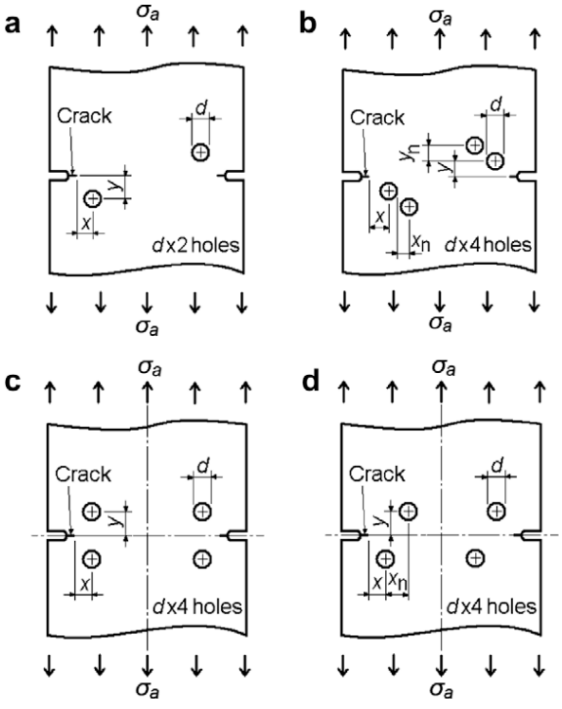

Figure 3-12: Schematic representation of the hole arrangement (Makabe et al., 2009)

Atteya performed another experimental and numerical study on crack-deflecting holes in 2020, which studied the effect of crack-arresting holes on internal cracks. The specimen and hole configuration is shown in Figure 3-13 and Figure 3-14. Three specimens with different holes placement were tested in addition to a control specimen. The crack was successfully arrested in one specimen, significantly increasing fatigue life.

The crack was slightly deflected towards the drilled hole in the remaining two specimens due to mode II loading. However, according to Atteya, the ratio between mode II and mode I load was not height enough to force the crack into the hole. The study showed that crack-deflecting holes influenced crack propagation in two ways:

- Accelerated crack growth due to stress concentration around the hole.
- A shielding effect is provided by the hole at the crack tip, which slows down the crack growth.

In the specimens where the crack was not successfully arrested, the crack retardation due to the shielding effect where lower than the crack acceleration due to stress concentration around the hole. Thus, the overall fatigue life was lower than the reference specimen.

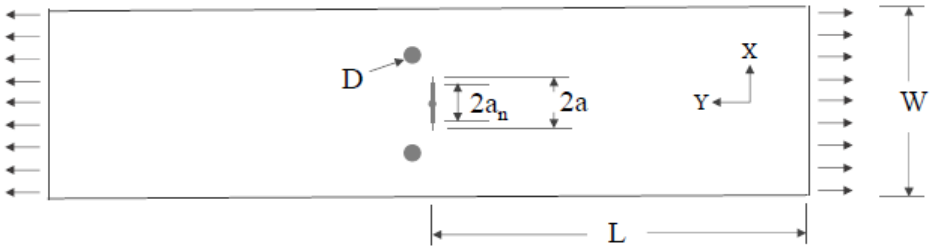

Figure 3-13: Specimen geometry, (Atteya et al., 2020)

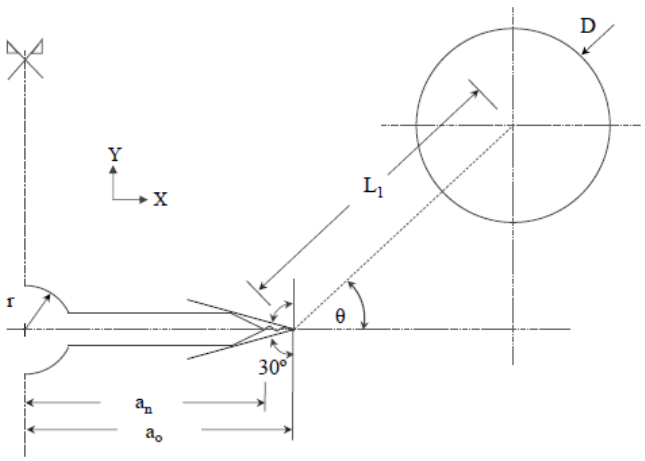

Figure 3-14: Schematic representation of the hole arrangement (Atteya et al., 2020)

As evident from the studies, crack-deflecting holes may serve as an efficient repair method for stopping or retarding further crack development due to cyclic loading. However, it is seen that correct hole placement is critical to gain a positive effect of the method, which requires a good understanding of the stress field and how the presence of holes modifies it.

3.4.3 Hole Drilling Repair in Offshore Tubular Joints

Stop holes are an attractive method for underwater repair and have been used in tubular joints in offshore jacket structures, although with some variation in their effectiveness (Sharp & Ersdal, 2021). In 1998 an experimental study on fatigue performance on repaired tubular joints was carried out by the welding institute (Tubby, 1989). Among several repair methods, stop holes with cold expansion were tested on two tubular T-joints subjected to cyclic out-of-plane bending, as shown in Figure 3-15.

The main observation from the test was that the first crack to appear after retesting the repaired joint was a branch from the main toe crack, as shown in Figure 3-15. In practice, it would be difficult to find and sufficiently treat such areas. Consequently, a single untreated branch may be catastrophic. Tubby concluded that hole drilling and cold expansion was not effective repair method in the two specimens investigated.

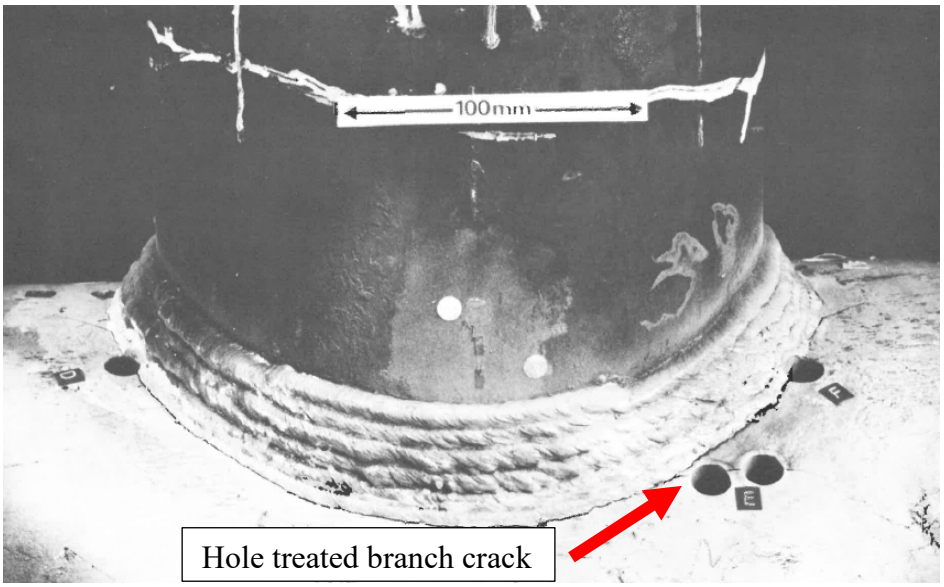

Figure 3-15: Cracked tubular joint with stop hole repair (Tubby, 1989)

4 Specimen Construction and Fatigue Test Method

4.1 General

This section describes the specimen's design, material, fabrication process, and fatigue testing setup and procedure. Understanding the material properties, joint geometry, and manufacturing processes is essential to analysing the joint's performance under cyclic loading. Additionally, a description of the test setup, data acquisition system and procedure ensure the reliability and repeatability of the test results. This section aims to provide an understanding of the specimen design and methods employed in the fatigue test, serving as a basis for the results, discussion, and conclusions in subsequent sections.

The testing program consists of a fatigue test of one welded DT-joint and tensile coupon tests of the material used. The fatigue test comprises cracking, repairing and testing the fatigue endurance of the repaired specimen. The joint design and fabrication are equal to the specimen tested by (Atteya, to be published), thus enabling a comparison of the results.

4.2 DT-Joint Specimen as built

4.2.1 Specimen Geometry and Dimensions

One DT-joint specimen was fabricated with the geometry shown in Figure 4-1, the dimension given in Table 2, and the following non-dimensional geometrical parameters:

- $\beta = \frac{d}{D} \approx 0.5$
- $\tau = \frac{t}{T} \approx 1$
- $\gamma = \frac{D}{2 \cdot T} \approx 12.9$
- brace to chord angle $\theta = 90°$

Table 2: DT-joint specimen dimension

Description	Symbol	Value	Unit
Chord thickness	T	8.20	mm
Chord diameter	D	219.1	mm
Brace thickness	t	8.56	mm
Brace diameter	d	114.3	mm

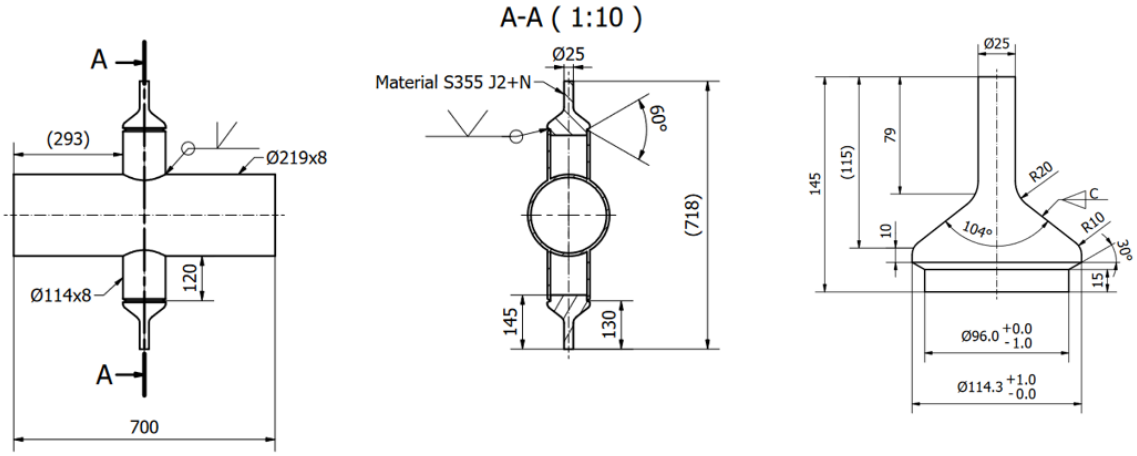

Figure 4-1: DT-joint Geometry *source* (Atteya, to be published)

4.2.2 Specimen Material

The brace and chord were both made of hot-rolled, seamless pipes formed from normalised structural steel satisfying the grade requirements S355 G15+N. According to the mill certificate, the brace member had a yield strength of 390MPa and an ultimate strength of 530MPa, while the chord member had a yield strength of 435MPa and ultimate strength of 530MPa. The cones were machined from a 120mm shaft of steel S355 J2+N. The complete mill certificate for the brace and chord members can be found in Attachment 2.

4.2.3 Specimen Fabrication

RPT-Production, a leading welding, pipe bending and prefabrication provider located at Bryne, fabricated the DT-joint specimen utilising an identical WPS employed for the fabricating of Atteya's specimens. The complete weld comprises an initial root pass executed with tungsten inert gas welding (process 141), succeeded by a second pass, fill and cap weld utilising flux-cored arc welding (process 136) in conjunction with active shielding gas. NDT testing was conducted in compliance with the requirements stipulated in DNV-OS-C401, including 100% visual inspection, 100% magnetic particle testing and 100% ultrasonic testing. No weld improvement technics were applied before the pre-cracking of the specimen. A picture of the DT-joint as fabrication can be found in Figure 31, while the weld and NDT specifications, documentation, and specimen drawings are presented in Attachment 4 and Attachment 3, respectively.

Figure 4-2: DT-joint as built

4.3 Fatigue Test and Measurement Setup

4.3.1 Fatigue Testing Rig

The machine employed for the fatigue testing was the MTS 809 Axial/Torsional Test System model 319.25, located in the workshop at the University of Stavanger. The machine can apply axial and torsional load as well as displacement. Moreover, the test system can conduct a wide range of evaluations, spanning from static to multiaxial fatigue testing. Under dynamic loading, the load frame is rated to a maximum axial force of 250kN and 2500Nm torsional force. Furthermore, the system permits a maximum axial displacement of 150 mm and a torsional range of ±45 degrees. The actuator, connected to the lower gripper, is driven by an external Hydraulic Power Unit (HPU), while the load cell is positioned above the upper gripper. The specimen was vertically positioned in the test machine with the grippers attached to the braces, as shown in Figure 4-3. All testing was performed at room temperature.

Figure 4-3: Test machine, HPU (MTS, n.d.) and specimen installed in the test system, respectively

4.3.2 Strain Gauges and Thermocouples

Linear electric strain gauges were installed at critical locations on the DT joint to measure the stress distribution in the chord, detect and map crack propagation, and acquire the stress concentration factors. As the strain gauges are sensitive to temperature, thermocouples PT100 were glued to the specimen to constantly measure the temperature of the specimen and correct the strain readings.

In each quadrant of the specimen, six strain gauges were attached. The strain gauge layout within a single quadrant is depicted in Figure 4-4, featuring two SGs at the saddle point to capture the maximum hot spot stress with the aid of the linear extrapolation method described in DNV-RP-C203. Additionally, one SG was positioned at both ±22.5˚ and ±45˚ angles from the saddle point to facilitate the identification and monitoring of the crack propagation throughout the testing.

The first row of strain gauges nearest to the weld toe were placed in extrapolation point A, as specified in DNV-RP-C203. Meanwhile, the strain gauges farthest from the weld toe, located at the saddle position, were positioned at extrapolation point B.

- Point A at chord surface normal to the weld toe $= 0.2\sqrt{rt} = 4.4mm$
- Point B at chord surface normal to the weld toe $= 2\pi R\frac{5}{360} = 9.6mm$

The strain gauges used in the testing were designated 1-LY71-3/120. These gauges exhibit a temperature-responsive characteristic, which allows them to self-compensate within the temperature range of -10°C to 120°C when used on ferrite steel. Moreover, the gauges have a grid length of 3mm, a nominal resistance of 120 ohms and are connected with solder tabs.

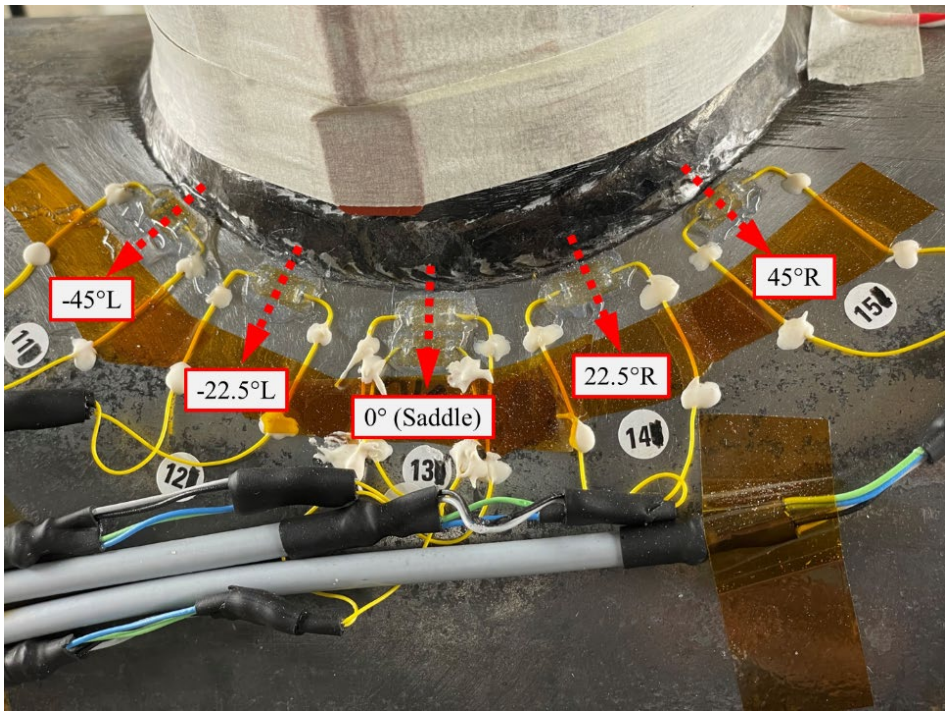

Figure 4-4: Strain gauge layout at quadrant 1

4.3.3 Data Acquisition System and Microscope

HBM's computer-controlled data acquisition system acquired the strain gauge measuring data throughout the testing. The strain gauges and thermocouples were connected to QuantumX bridge amplifiers coupled with a computer. Strain gauge readings, visualisation and post-processing were performed with the data acquisition software CatmanEasy-AP.

A total of 24 strain gauges were connected to two QuantumX MX1615B modules with a capacity of up to 16 sensors each, and the three thermocouples were connected to QuantumX MX440B. An ethernet switch interconnected the three QuantumX modules, which were then connected to a computer with a firewire.

Based on a convergence study of the peaks and troughs of the strain readings, a strain gauge sampling rate of 300Hz was selected, 50 times greater than the highest test frequency applied. During the testing process, the raw data was processed using CatmanEasy-AP software. This facilitated temperature compensation of strain gauge measurements, estimation of hot-spot stress through weld toe stress extrapolation, and documentation of stress alterations over time to associate them with crack initiation, propagation, and residual stress relief.

In addition to the strain gauges, a digital handheld microscope was used throughout the testing to examine and track the surface crack propagation. This enabled a rough validation of significant changes in the strain gauge readings and enhanced the overall crack analysis. The handheld microscope was equipped with a 5-megapixel sensor and a magnification capability of up to 200 times.

4.4 Fatigue testing of the DT-joint

4.4.1 Loading of the specimen

The specimen was tested under constant amplitude sinusoidal loading, in which sole axial force was applied through the brace. The entire fatigue testing process was carried out under load control, maintaining a positive R-ratio and a constant frequency at 3 and 6 Hz.

Before initiating the fatigue test, several preparatory steps were performed:

1. Stresses before and after clamping were collected to determine eccentricity and misalignment in the specimen and test machine.
2. Incremental static load was applied to verify sufficient gripping pressure, stabilise the gauges and determine the maximum hot spot stress.
3. Cyclic loading at 6 Hz was applied to facilitate a convergence study of the strain gauge sampling frequency and ensure stable strain readings.
4. Cyclic loading was utilised to determine the peak SCF across various load ranges. A total of 100 cycles were conducted within each load range, spanning from 10 kN to 40 kN, with increments of 10 kN. The maximum HSS captured during this stage was 85% of the characteristic yield strength. An R-ratio of 0.1 was maintained throughout testing. (Young's modulus was taken as 207 GPa)

The test commenced with a load range of 40kN and an R-ratio of 0.11, giving a maximum HSS of 316 MPa. Initially, the load frequency was set to 6 Hz. However, it was reduced to 3 Hz when approaching crack stage N1.

4.4.2 Monitoring during testing

The strain gauges positioned on the specimen enabled the monitoring of the stress distribution across the chord saddles and captured variations in the stresses during testing. Alternation in strain gauge readings is indicative of stiffness reduction due to crack initiation and subsequent propagation. A handheld microscope was used to examine the surface crack progression to supplement the strain gauges. A mixture of water and oil was applied to the affected area, enhancing the crack visibility and aiding in their detection under the microscope.

After reaching N1, a distinct rib mark was created at the crack surface at every 20 000 to 40 000 cycle intervals by applying 200 cycles with a different frequency and R-ratio. The maximum marker load applied was equal to the peak load in the testing, ensuring a similar maximum crack opening for both loads. The R-ratio and frequency were 0.9 and 1 Hz, respectively. This method facilitates crack surface analysis with fractographic after completing the fatigue test.

4.4.3 Justification of Fatigue Test Parameters

The primary objective of the fatigue test was to evaluate the behaviour and effectiveness of crack-deflecting hole repairs in tubular joints subjected to fatigue cracks forming under high-cycle fatigue conditions. Extensive research has been performed on the subject by Atteya. Therefore, it was essential to perform the fatigue test in a manner that facilitated a reliable basis for comparison of the results. Thus, the specimen design, test parameters and procedure were closely aligned with those in Atteya's research. However, the load range was significantly reduced in the subsequent fatigue test to avoid stress ranges in the low-cycle fatigue regime.

As the fatigue testing is carried out under load control, a significant increase in stress range in the crack tip proximity will occur as the crack develops and the specimen loses stiffness. Hence the load range was further decreased in the post-repair testing to maintain stress ranges within high-cycle fatigue conditions.

Real offshore jacket structures are usually highly redundant, meaning that the load will be redistributed in other load paths if one member or joint starts losing its load-bearing capacity. This suggests that fatigue testing controlled by deformation or displacement would more precisely represent the behaviour of redundant structures. That being said, fatigue testing of tubular joints under load control is expected to give shorter fatigue life than similar features in redundant in-service structures. The failure criteria in SN-curves used in this testing and offshore structures are the onset of through-thickness cracking, and as these are based on load-controlled testing, the failure criteria are considered to provide a safety margin for offshore structures. (Atteya, to be published)

5 Result of Fatigue Test

5.1 Overview

The complete fatigue testing scheme of the DT joint aimed to evaluate the fatigue life of the DT joint and the effectiveness of repair methods. The program involved three main stages:

1. **Pre-cracking:** the specimen was subjected to cyclic tension load until a through-thickness crack was achieved.
2. **Repair:** two repair methods were performed on the specimen: weld toe dressing at the cracked quadrant and crack deflection holes at the crack tip proximity.
3. **Post-repair testing:** the repaired specimen was subjected to further cyclic loading to evaluate the performance of the repair methods. This phase comprised two attempts.
    a. 1st attempt: testing until a clear indication of improved fatigue life under constant load range in high cycle fatigue conditions
    b. 2nd attempt: the specimen was tested further under a significantly higher load range until N4 (low cycle fatigue conditions)

In the following chapter, the result of the complete testing scheme will be presented in the order mentioned above.

5.2 Pre-Cracking Phase

5.2.1 SCF Calculation and test setup check

Before initiating the fatigue testing, a verification check was conducted by inspecting the SCFs in all the saddle positions for different static load levels ranging from 10 to 44.5 kN. The maximum HSS was in Q2, with an SCF of 19.2 at a static load of 10 kN, increasing to 19.5 for a static load level of 44.5 kN. In addition to the calculation of the SCF with static load levels, the SCF was calculated for the load range employed in the pre-cracking. Figure 5-1 shows the SCF for the four quadrants subjected to the load range used in the pre-cracking.

The quantification of the HSSs' was accomplished via the linear extrapolation technique described in section 2.3.2, where the strains recorded from the strain gauge at point a and b was linearly extrapolated towards the weld toe. The SCF was then obtained by dividing these HSSs by the brace's corresponding nominal stress level or stress range. The maximum SCF based on the 40 kN load range was 20.45 and located in Q2 and the average SCF of the four saddle positions was 19.89.

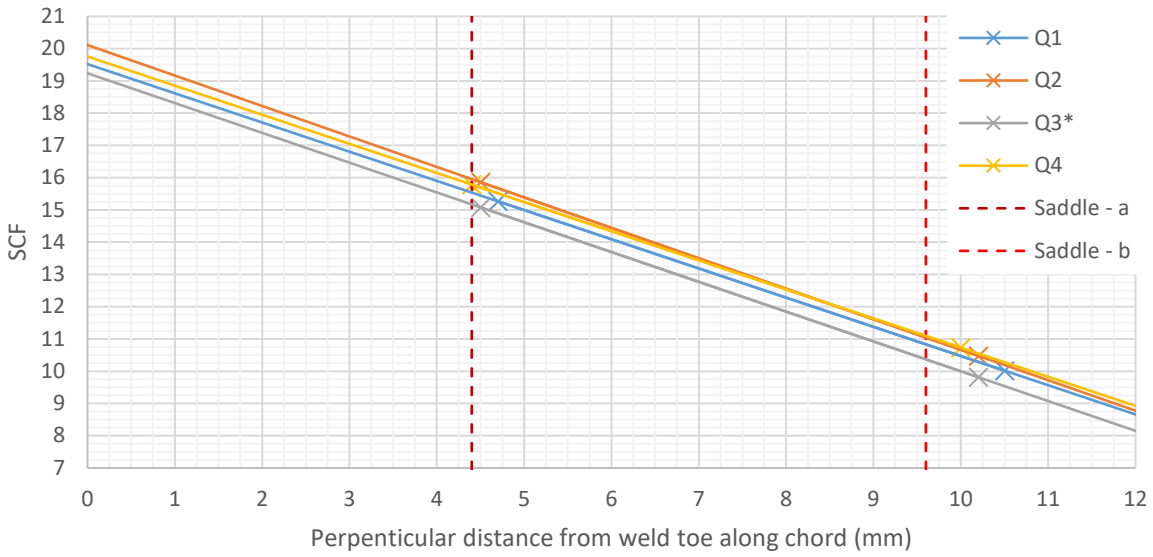

Figure 5-1: SCF at the four quadrants from the experimental work, with ΔP=40 kN. *The SG positioned in saddle-b at Q3 was not measured after installation. Hence, the average SG placement in saddle-b from the other three quadrants is plotted.

In addition to the experimental study of the SCFs, a finite element model was created in the software Dassault Systems Abaqus Version 2017 to study the SCF further and compare it with the experimental work. The geometrical dimension and material properties chosen in the model were aligned with the dimension and properties measured from the experimental test specimen and set as follows:

- Brace
  - Thickness, t = 8.5 mm
  - Diameter, d = 114 mm
- Chord
  - Thickness, T = 8.5 mm
  - Diameter, D = 219 mm
- Material properties
  - Yield strength, fy = 410 MPa
  - Youngs modulus, E = 207 GPa
  - Passions ratio, ν = 0.3

In the DT-joint model, the fully integrated first-order linear hexahedron brick element C3D8 incorporating eight integration points was selected. The characteristic mesh size surrounding the brace-chord intersection was set to 1 mm, and five elements were used through thickness for both the brace and chord. Figure 5-2 shows the FE model and mesh around the saddle point in the brace-chord intersection. The weld profile was excluded in the FE model as it is considered not significantly influence the HSS derived from linear extrapolation.

The boundary conditions were established to align with the fixation and load application in the experimental testing. A local polar coordinate system was created with the z-axis running through the cone's centre axis along the direction of the brace, with the radial plane subsequently falling parallel with the brace cross-section.

In the cone attached to the lower gripper where the load was applied, the rod was set to have zero displacements in the rotational direction around the z-axis. In the opposite gripper, the rod was set to have zero displacements in both the translational z-direction and rotation about the z-axis.

For load implementation, a concentrated point load was assigned on a reference node. This reference node was linked with all nodes in the lower rod incorporating beam MCP constraints. The chosen load level was 2.95 kN, giving a nominal stress level of 1 MPa in the brace, which facilitates easy calculation of SCFs. The analysis was performed as a static linear perturbation, which does not include any geometrical non-linearities, as these are considered insignificant.

The SCF in the FE model was determined in the same manner as in the experimental testing by linearly extrapolating the directional stresses from points a and b perpendicular to the weld toe. This method yielded an SCF of 20.63, which is greater than the SCF derived from the experimental testing. This slight deviation is anticipated, given that the strain gauge is capturing the average strain over an area of 3mm x 3mm while the FE result is extracted along a path of nodal stresses that goes through the centre line of the strain gauge.

An SCF of 20.62, demonstrating a reasonably good match with the maximum SCF of 20.45, as determined from the experimental work, which also matches well with the SCF of 20.55 derived from equations given in DNV C203. It is worth mentioning that the stresses that compares with the SN-curve is the principal stresses, which is generally expected to be 15% higher than the Hot spot directional stresses derived here (CIRIA, 1985).

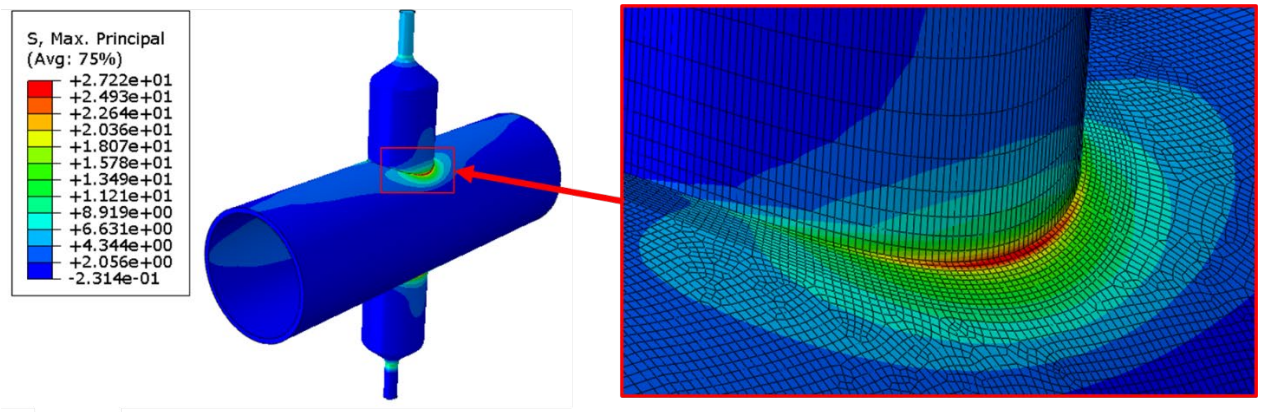

Figure 5-2: FE model of the intact DT-joint

5.2.2 Test Loading

The load range and R-ratio maintained throughout the pre-cracking stage were 40 kN and 0.1, respectively. Initially, the frequency was set to 6 Hz but reduced to 3 Hz after an 11% loss in the hot spot stress range at saddle point in Q3 at 300k cycles to ensure documentation of critical events. The maximum load reach in the testing (Pmax) was 45 kN, while the minimum (Pmin) was 5 kN. Stress distribution along the brace chord intersection and hot spot stresses at saddle positions were recorded. HSS recordings and load cell readings facilitated the calculation of SCFs.

5.2.3 Stress Distribution

Strain gauges were installed on the chord brace intersection across all four quadrants of the specimen. Figure 4-4 illustrates the SG layout within a single quadrant, which is mirrored in the other three quadrants. The data represented in this chapter originate from the five strain gauges closest to the weld toe within each quadrant. During the mounting of the specimen, the stresses due to clamping were documented to map the stresses caused by eccentricity in the specimen and test setup. These are shown in Figure 5-3.

As the testing commenced, the stress ranges were recorded and as anticipated for DT joints subjected to axial load, the largest stress ranges were located at the four saddle points. The stresses gradually decreased towards the crown, as shown in Figure 5-4. It is also apparent in Figure 5-4 that stress ranges in all four quadrants are quite similar and symmetric around the saddle. This provides a rough indication of symmetrically placed strain gauges and a lower probability of significant eccentricities in the specimen or test setup. The highest stress range recorded was found in Q2 and Q4.

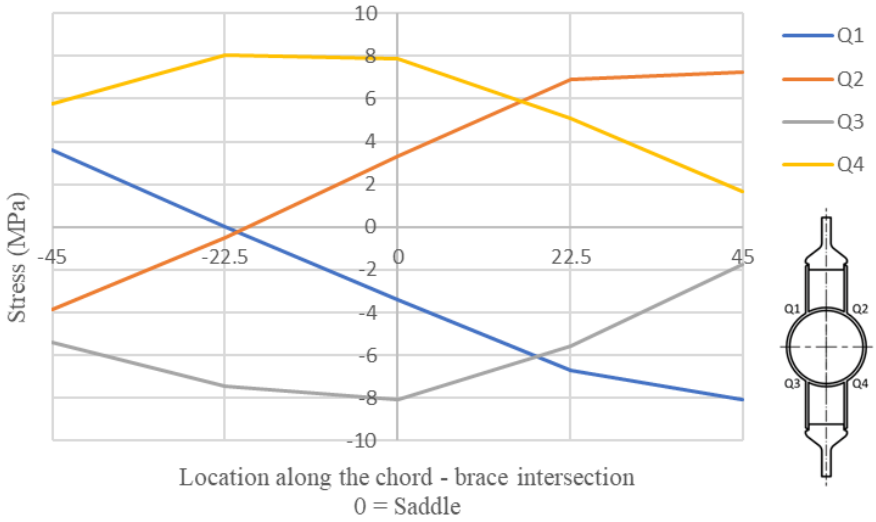

Figure 5-3: Stresses resulting from clamping the specimen in the test rig

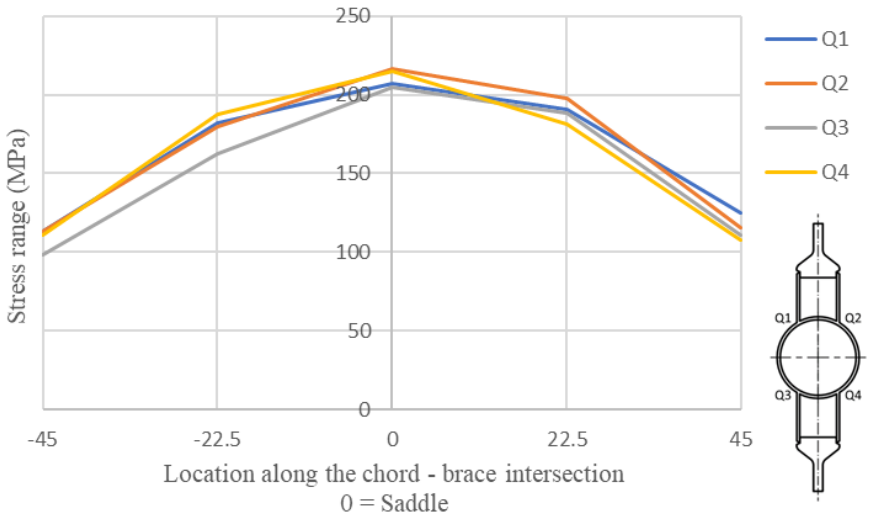

Figure 5-4: Stress range distribution at strain gauge closest to weld along chord-brace intersection (ΔP=40kN)

5.2.4 Result of Pre-Cracking

The first noticeable change in stress range was located at the saddle point in Q3 when passing 110 000 cycles. After 342 000 cycles, the hot spot stress range had dropped 15% in Q3, marking N1. In addition, to the strain gauge readings, the crack development was monitored with a microscope and the surface crack versus the number of cycles is shown in Figure 5-6. At 200 000 cycles, the crack became visible at the saddle point in Q3. The crack continued developing from 0 degrees towards strain gauges positioned at both ±22.5˚, and a 7.5 mm surface crack was detected after 410 000 cycles denoting N2. After N2, the crack kept propagating symmetrically around the saddle point until reaching about 1 million cycles and a crack length of 32 mm. It was then apparent that the crack propagation towards the negative direction started to increase while the propagation in the positive direction declined. This behaviour can also be interpreted from Figure 5-5, showing the stress range versus the number of cycles.

It was decided to stop the test at 1.515 million cycles as the strain gauges at the saddle and -22.5˚ degrees had passed 90% and 96% drop in strain range, respectively. Hence, it was assumed that a through-thickness crack was achieved between the two strain gauges marking N3. The surface crack length was measured to 73mm, spanning between strain gauges at -45˚ to the strain gauge at +22.5˚. A summary of the fatigue life is shown in Table 3.

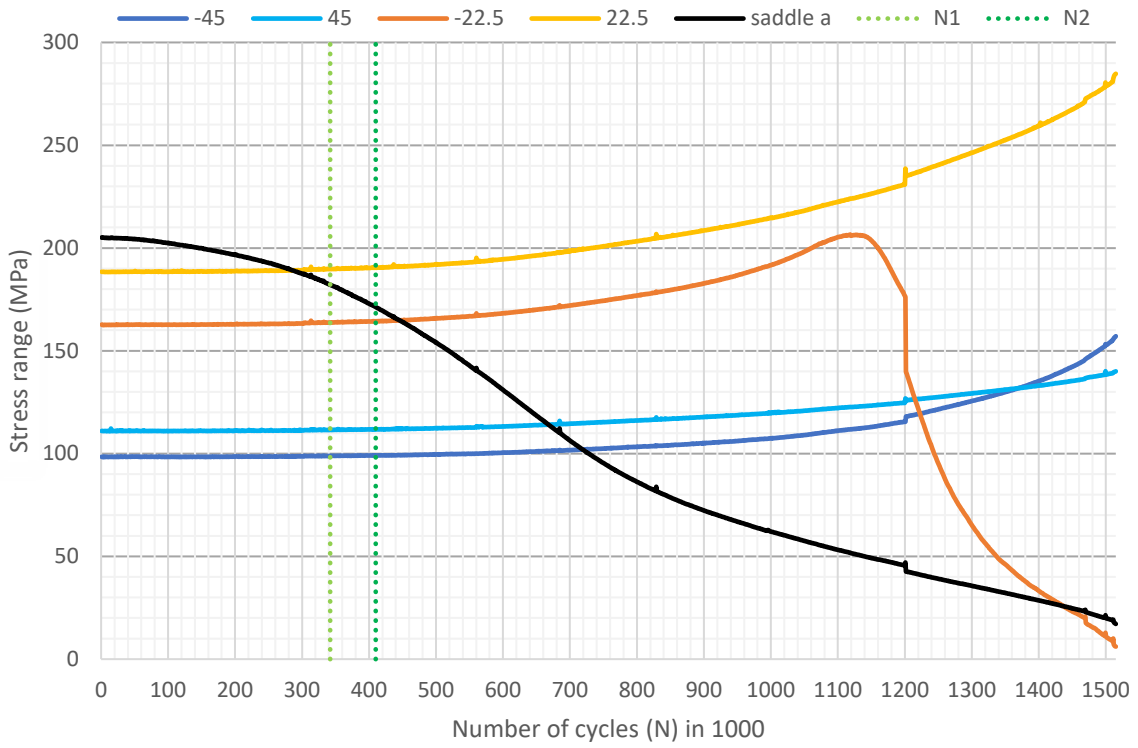

Figure 5-5: Stress range vs number of cycles.

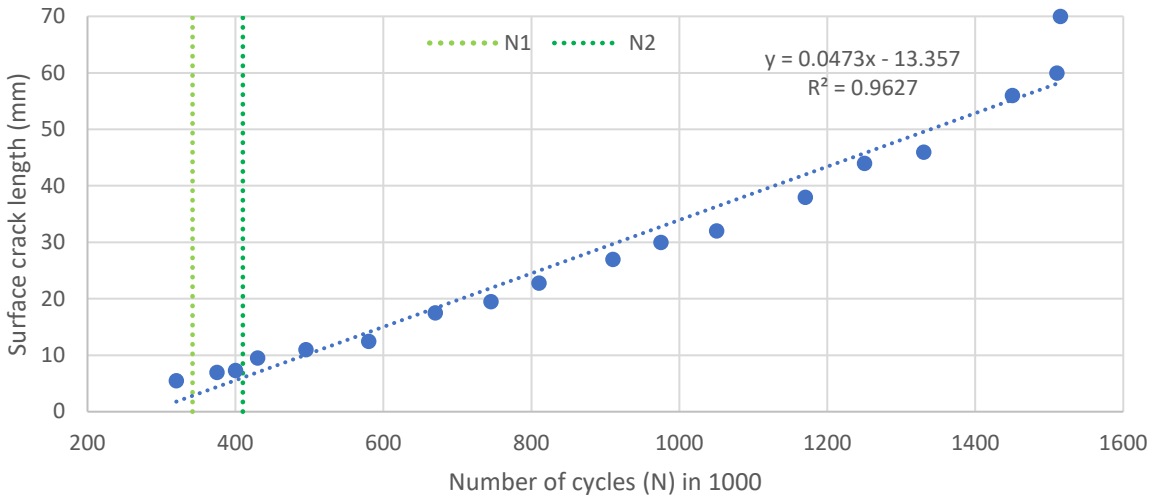

Figure 5-6: Surface crack length vs number of cycles

Table 3: Fatigue testing results of the pre-cracking stage

Fatigue life	Number of Cycles	Remark
N1	342 000	15% drop in the measured hot-spot strain*
N2	410 000	7.5 mm surface crack length
N3	1 515 000	observation of 100% loss in the hot-spot strain readings**

**The hot-spot strain is measured by linear extrapolation from two strain gauges placed perpendicular to the weld toe.*
***Two strain gauges lost over 90% of the strain range. Therefore, 100% strain range loss between these strain gauges is assumed.*

It was observed that the crack initiated in the quadrant with the lowest HSS range, which is somewhat unexpected. However, as explained in section 2.2, the HSS is arbitrary and determined from linear extrapolation. The true notch stresses at the weld toe are greatly influenced by the weld profile. As shown in Figure 5-7, a weld spatter is located at the saddle point in the chord in Q3. It is believed that the crack initiated at this spatter.

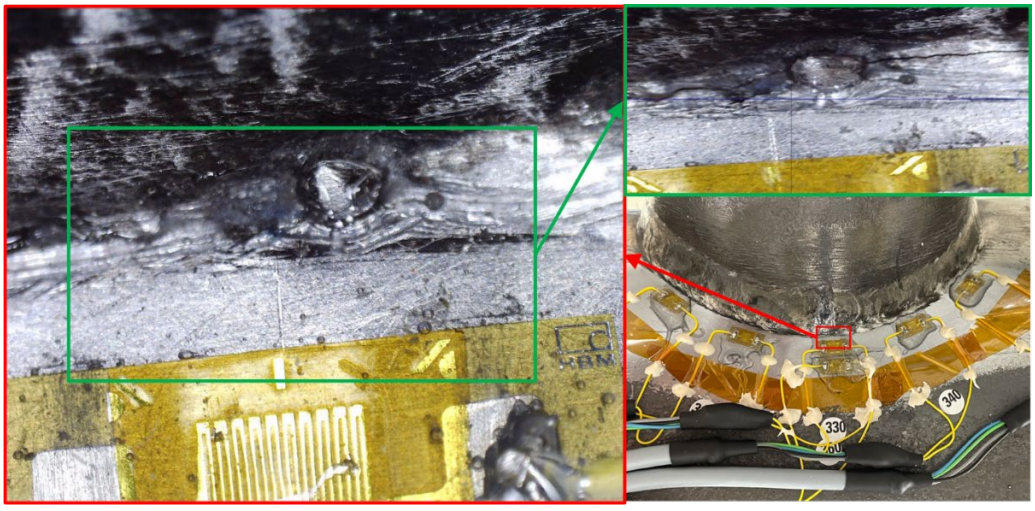

Figure 5-7: Weld scatter at the saddle in Q3

5.3 Repair of the Cracked DT-Joint

After pre-cracking the specimen, a combination of two temporary repair methods was tested on the DT Joint specimen comprising crack deflection holes in the crack tip vicinity and weld toe grinding. The location of the crack tip was determined with MPI and visual inspection with a microscope. As described in section 5.2.4, only Q3 had a through-thickness crack. The remaining three quadrants were still intact.

5.3.1 Crack Tip Localisation

For crack-deflecting holes to increase fatigue endurance, it is vital to determine the exact location of the crack tips to place the holes in a favourable spot. Several steps were carefully carried out to validate the crack tip's location. First, the crack tips were located with the strain gauge readings and a microscope. Then MPI with fluorescent was conducted to validate the position. Finally, MPI with fluorescent was performed repeatedly with the specimen subjected to a static tensile load of 30 kN to open the crack. As there was a good agreement on the crack tip position in all three inspections, the crack tip position was concluded to span from -38˚ to +21˚ in Q3. In Figure 5-8, the crack inspected with MPI is depicted.

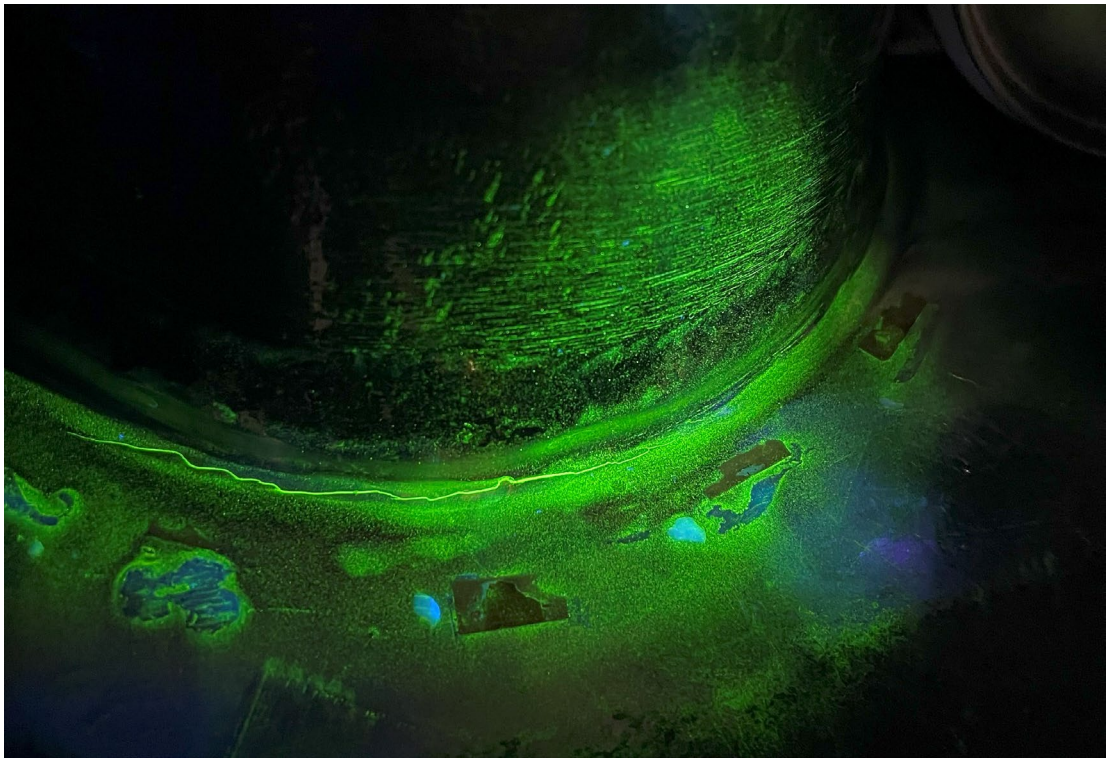

Figure 5-8: MPI of the crack in Q3

5.3.2 Specimen repair

The specimen was repaired by drilling holes in the crack tip proximity. This was accomplished using a magnetic-based drill fitted with 18 mm carbide twist bits and supplemented by cutting fluid to avoid excessive heating of the hole surface in the drilling process. After the hole drilling, the burrs from the drill bit were removed by ground smoothing the hole edges.

Positioning of the holes was made in alignment with Atteya's testing by centring the holes 12˚ ahead of the crack tip and shifting them 15 mm perpendicular from the weld toe. As the crack spanned from -38˚ to +21˚, the holes were placed centred at -50˚ and +33˚. The objective of the crack-deflecting holes was to deflect the crack away from the weld toe, which holds significant stresses and arrests the crack in the holes.

Figure 5-9: Magnetic-based drill

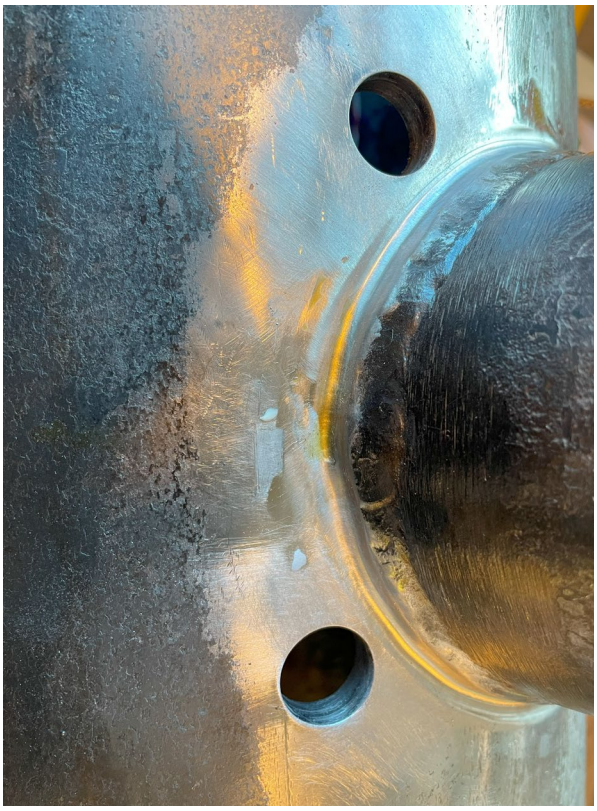

Figure 5-10: Carck deflecting holes

In addition to the crack deflecting hole repair, weld toe grinding was performed in Q3. The repair was conducted at RPT production, where a rotating "balled-nosed tree" carbide burr with a maximum diameter of 8 mm was used to grind the weld toe in compliance with BS 7608 (British Standard, 2015). The weld toe was further enhanced by sanding the weld toe in a direction perpendicular to the weld toe with a 240-grit paper Figure 5-11, which produced a surface roughness of 58.5 µm (Upmold, 2017) Figure 5-11.

The weld toe grinding needs to satisfy several requirements to benefit the fatigue endurance, both regarding the grinding process and the resulting weld toe profile, Attachment 6. Post repair, the emerged weld toe profile exhibited an average depth and radius of 0.5 mm and 3.4 mm, respectively Figure 5-12, which aligns with the DNV C203 and BS 7608 specifications further described in section 3.3.1. A correctly ground weld toe serves as an efficient way of reducing the SCF at the weld toe and delaying crack initiation.

Figure 5-11: Sanding weld toe

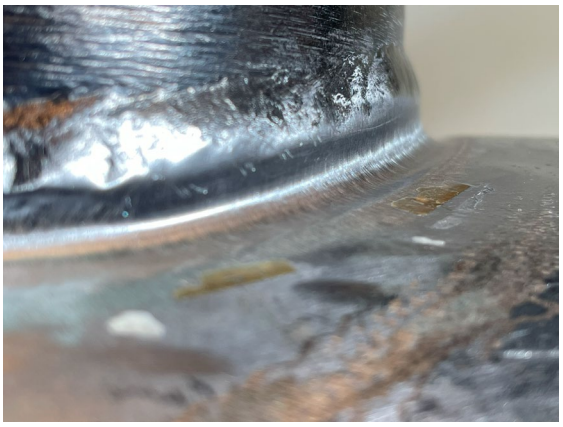

Figure 5-12: Weld profile after weld toe repair

After the repair, a set of three new strain gauges were installed around each crack deflecting hole in the repaired quadrant, as shown in Figure 5-13.

1. The strain gauges between the holes closest to the chord saddle (SG 313 and 323) monitored the crack propagation towards the crack-deflecting holes and aided in determining the point of through-thickness cracking between the holes.
2. The strain gauges closest to the weld-toe and chord crown (SG 311 and 321) detected new crack initiation behind the holes and monitored the strains where the maximum stresses in the specimen were expected to be located.
3. The third strain gauge closest to the holes (SG 312 and 322) measured the strains where the maximum stresses around the hole were expected. Furthermore, it was used for validation of the numerical model of the DT-Joint.

In the numerical model of the repaired specimen, the position of the strain gauges concerning the stress field was studied further, as described in Section 6.3.3.

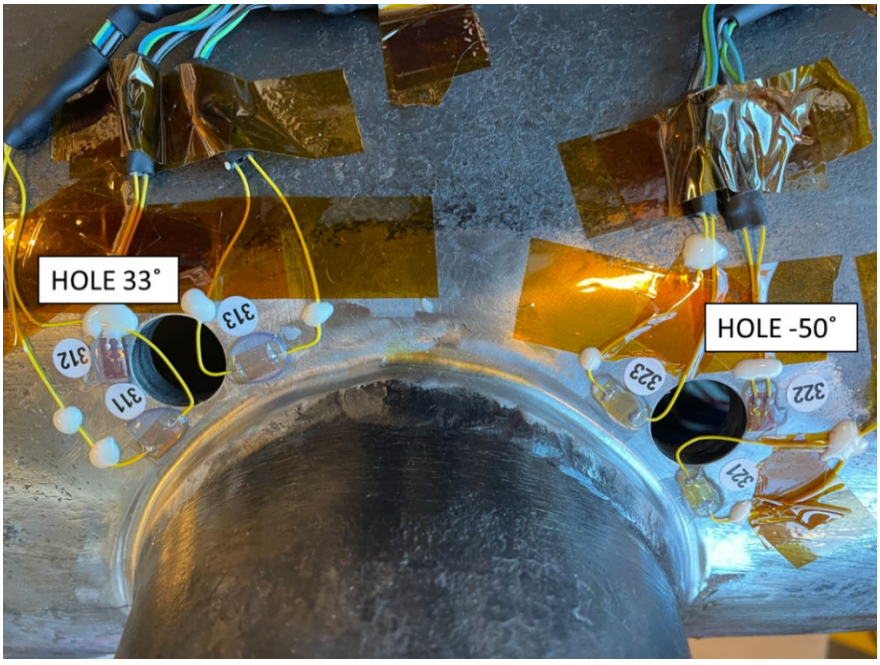

Figure 5-13: Strain gauge layout in repaired quadrant

5.4 Performance of the Repaired DT – Joint, First Attempt

5.4.1 Test Loading

In the final phase of the testing program, the performance of the repaired DT-Joints was tested by subjecting the specimen to additional cyclic stress. As the crack induces greater SCF while propagating, the load range was reduced to ensure that the stress range remained within the bounds of high cycle fatigue throughout the entire post-repair testing. A load range of 27kN was selected, maintaining an R-ratio of 0.1, resulting in a minimum load (Pmin) of 3kN and a maximum load (Pmax) of 30kN. The frequency was initially set at 5Hz but was later increased to 10Hz once the strain measurements stabilised and showed no indication of further crack propagation or initiation.

5.4.2 Repair Performance

As the testing commenced, the hole influenced the crack path by deflecting it away from the weld toe towards the holes. After 540 000 cycles, the surface crack entered the hole at -50˚ marking Ni1. The crack propagated through the strain gauge on the saddle side by hole -50˚ (SG 323), and the strain gauge was destroyed. This can be seen in the strain evolution diagram in Figure 5-14 and the picture in Figure 5-15. Through-thickness crack was observed at 910 000 cycles marking Ni2 at -50˚ hole.

The strain evolution diagram in Figure 5-14 and Figure 5-16 shows a distinct shift in the readings at about 30000s and 100000s. The first shift was due to the test machine's maintenance, which required the specimen to be re-installed. The second shift is due to a shutdown of the data acquisition system and subsequent loss of strain readings on 100 000 cycles.

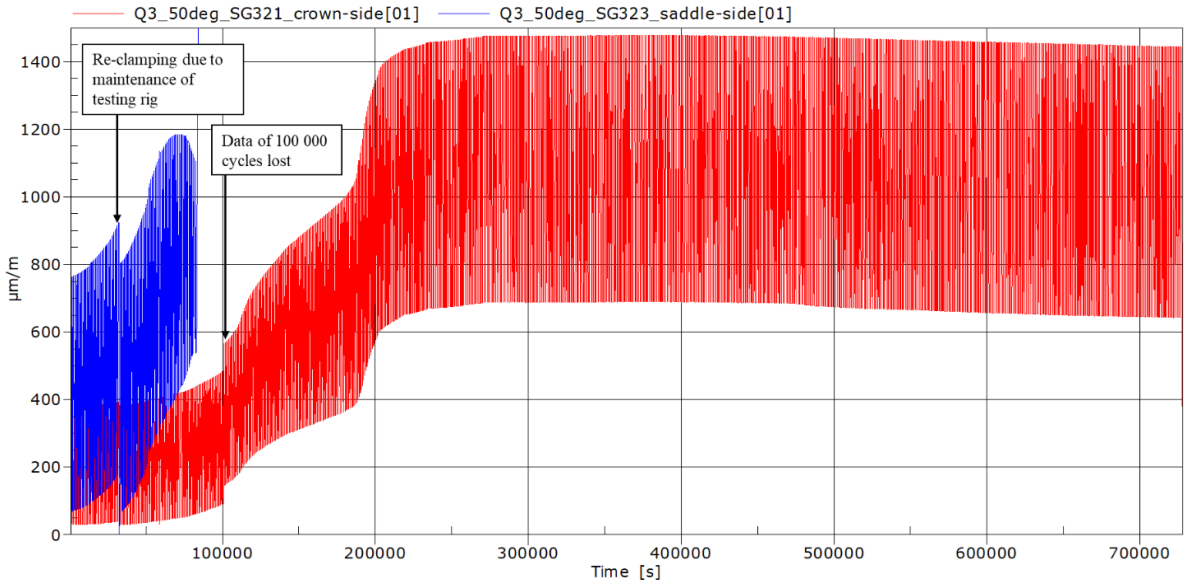

Figure 5-14: Strain evolution diagram -50˚ hole post-repair testing phase

Figure 5-15: Crack propagation into -50˚ hole

At the +33˚ hole, Ni1 was observed at 900 000 cycles. The crack then rapidly propagated to a full through-thickness crack between the holes at 930 000. Confirmation of the full through-thickness crack was achieved through visual inspection and interpretation of the strain gauge measurement. Figure 5-16 shows that the strain gauge at the saddle side of hole +33˚ have lost nearly the entire strain range while the strain gauges on the crown side exhibited a gain. The crack path into hole +33˚ is shown in Figure 5-17.

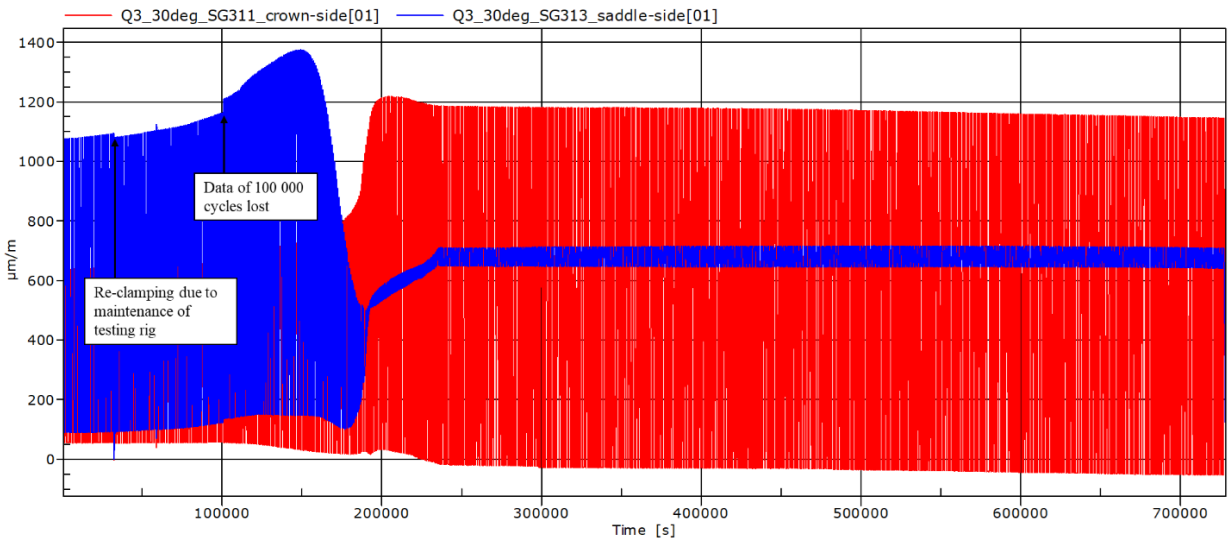

Figure 5-16: Strain evolution diagram +33˚ hole post-repair testing phase

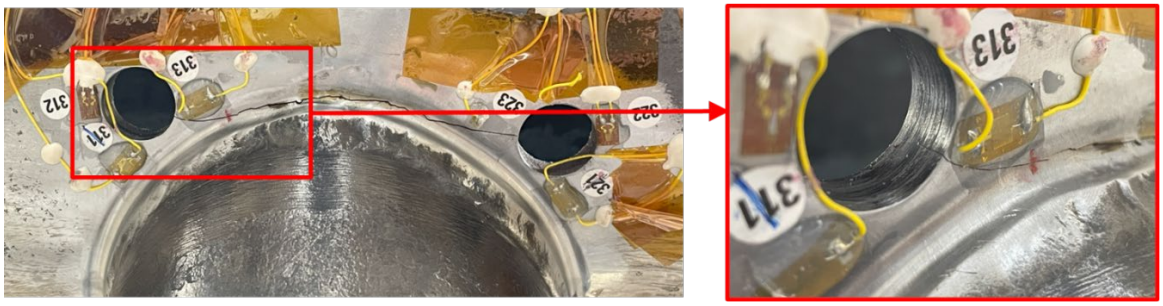

Figure 5-17: Crack propagation into +33˚ hole

The strain gauge readings stabilised after achieving a through-thickness crack between the crack-deflecting holes, and the testing continued for another 2 585 000 cycles. As there was no sign of crack initiation or further crack development, the conclusion that the repair had successfully increased the fatigue endurance in the specimen was drawn. Thus, it was decided to stop the testing after a total of 3 515 000 cycles in the post-repair testing phase. The conclusion drawn is further discussed in Section 6. Finally, in Table 4, the fatigue life of the repaired specimen is summarised.

Table 4: Repaired specimen fatigue life 1st attempt

Fatigue Life	**÷50˚ Hole**	**+33˚ Hole**
Ni1	540 000	900 000
Ni2	910 000	930 000
Run out	3 515 000	

Ni1 surface crack into the hole
Ni2 though-thickness crack into the hole

5.5 Performance of the Repaired DT – Joint, Second attempt

5.5.1 Test Loading

Due to run-out at the initial load level, an increased load level was tested in order to force cracking in the repaired DT joint. The new load range selected was adjusted to 54 kN, maintaining an R-ratio of 0.1. This load range gave a maximum load (Pmax) of 60 kN and a minimum load (Pmin) of 6 kN. Since the new stress range fell into the low cycle fatigue regime, events were anticipated to occur at a considerably accelerated rate. Hence the frequency was reduced back to 3 Hz to ensure enough time for documentation of events throughout the testing.

5.5.2 Reverse Coalescence

Previous testing of equal specimens has shown reverse coalescence, where the crack initiates in the weld toe beyond the crack-deflecting hole (crown side) and propagates back into the hole (Atteya, to be published). This behaviour does not align with the expected behaviour before Atteyas testing, where the crack initiates at the hole. Therefore, the specimen was subjected to further cyclic loading under a significantly higher load range to facilitate an investigation of crack initiation and propagation after repair. The reverse coalescence phenomenon is illustrated in Figure 5-18.

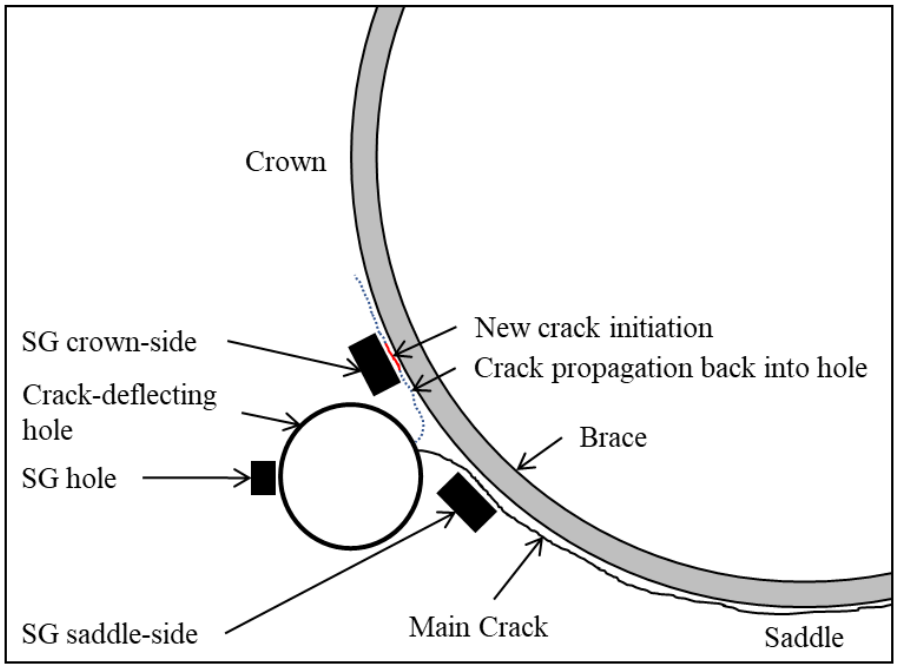

Figure 5-18: Reverse coalescence phenomena and strain gauge naming

5.5.3 Repair Performance

Upon starting the test, there was a slight increase in stress range, which was assumed to result from plastic deformation Figure 5-21. However, the stress range stabilised after about 20 000 cycles and remained stable until reaching 70 000, which marked the first stress reduction indicating material degradation. The first visual crack was observed between the SG crown-side at +33˚ hole and the weld toe, as shown in Figure 5-19 after 86 000 cycles. The crack then kept propagating towards the crown and back into the hole. Finally, at 145 000 cycles, the surface crack reached the +33˚ hole, and the reverse coalescence phenomenon was evident.

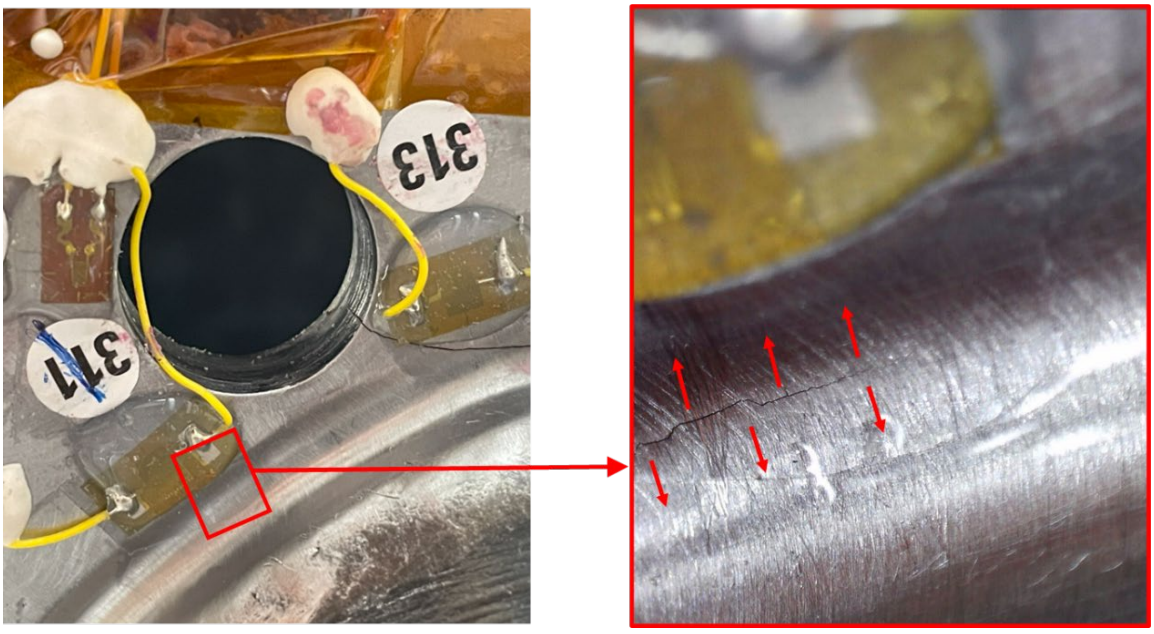

Figure 5-19: Crack initiation in front of SG crown-side at +33˚ hole

As the crack beyond the +33˚ hole propagated, the stress range at the -50˚ hole kept increasing until reaching 195 000 cycles. The stress range then pivoted and started decreasing, and the first visible crack was subsequently observed at 198 000 cycles. At 250 000 cycles, the crack reached back into the -50˚ hole and the reverse coalescence phenomenon was also present at this hole, as shown in Figure 5-20.

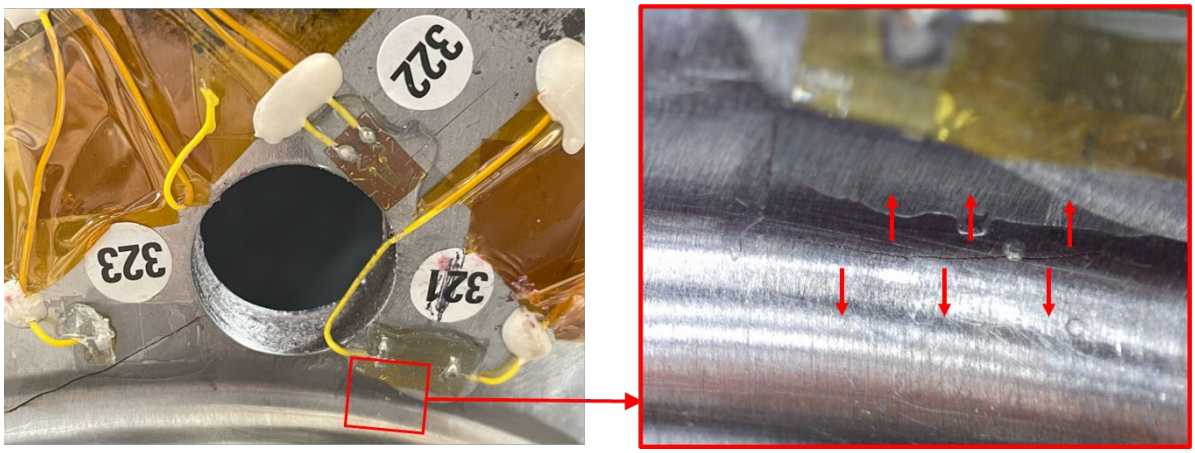

Figure 5-20: Crack initiation in front of SG crown-side at -50˚ hole

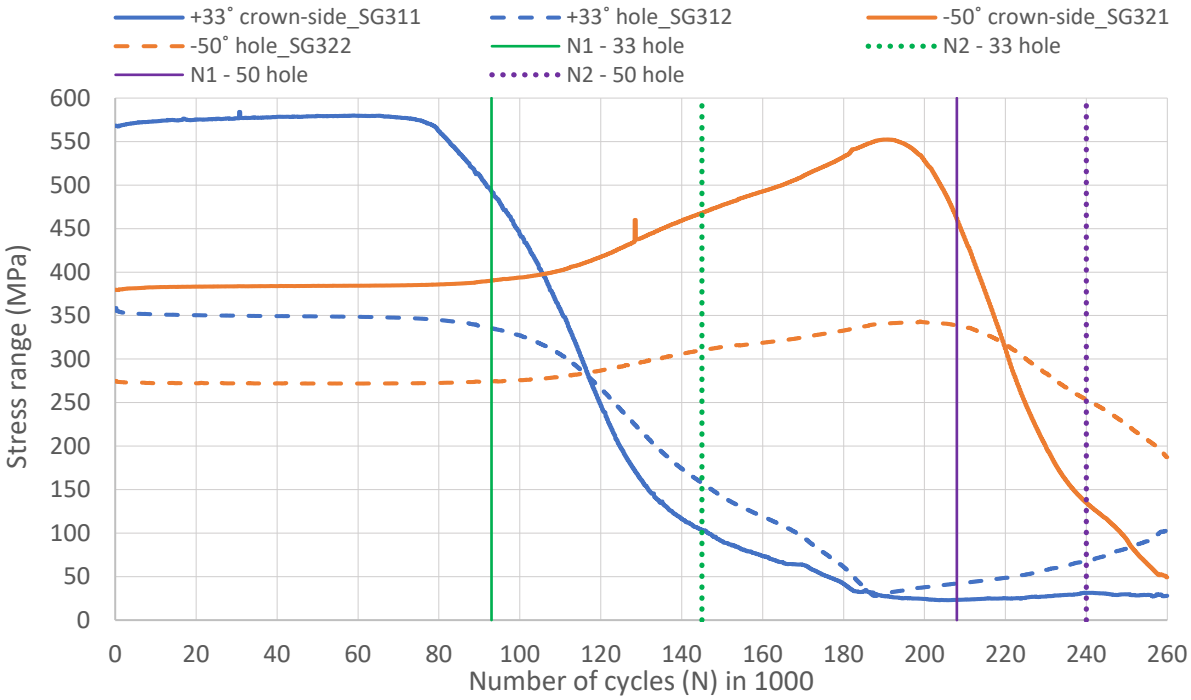

Figure 5-21: Stress range vs number of cycles post-repair

The testing was terminated after 260 000 cycles. At this point, the crack had propagated back into both holes and extended over a total length exceeding 1.5 multiplied by brace diameter marking N4. Considering the substantial bending forces introduced by the crack, the decision to stop the test at this point was to minimise potential risk to personnel and testing facilities. The resulting crack is shown in Figure 5-22 and the fatigue life stages are summarised in Table 5.

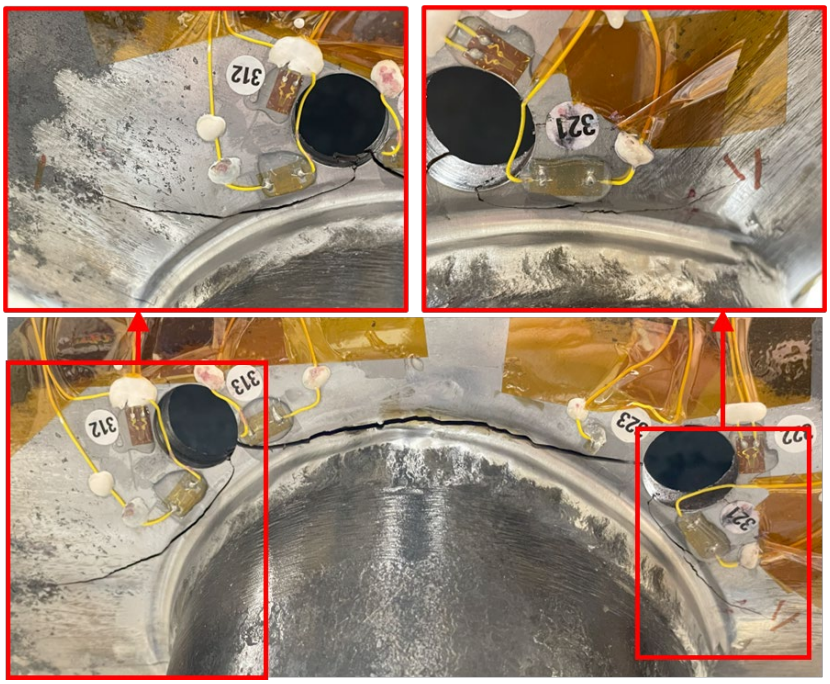

Figure 5-22: Total crack after terminated test

Table 5: Repaired specimen fatigue life 2nd attempt

Fatigue Life	**÷50° Hole**	**+33° Hole**
*N1**	208 000	93 000
*N2**	250 000	145 000
N4	260 000	

N1 Crack initiation beyond the hole 15% drop in strain range, refer to Figure 5-18*
N2 Crack entering hole reversely*

6 Evaluation of the Repair's Effectiveness

6.1 General

This chapter will discuss the effectiveness of the repair method investigated in the thesis. Herein two approaches will be utilised in determining the repairs' effectiveness. First, the fatigue endurance post-repair will be compared to the fatigue endurance in the pre-cracking phase. By comparing this relation to existing data on fatigue life from the N3 stage to N4, it is possible to determine if the repair had positively affected the fatigue life.

The other approach applied comprises extracting the stress range experienced by the specimen in the post-repair testing and comparing it to the SN curve. At first, this approach seems reasonable. However, it raises the question of which stress range to be utilised in combination with the SN curve. Thus, the following chapter also investigates and discusses the stress field and possible appropriate stress range to be used.

6.2 Repair's Effectiveness First Attempt Based on a Comparison with Existing Tests

6.2.1 Comparison Basis

An empirical approach to evaluating the efficacy of the repair is by comparing the number of cycles until N3 with those leading to N4. In Atteya's work, an equally designed DT-joint was tested under similar test conditions until N4 without any repair. Hence this test can be regarded as a suitable benchmark for comparison. Furthermore, in OTH 92 390, several axially loaded tubular joints underwent testing until reaching N4. Table 6 below summarises the test result from OTH 92 390 (HSE, 1999). It is essential to note that only the axially loaded tubular joints with a thickness of 16 mm and an r-ratio of 0 have been included in the summation. This selection criterion has been chosen due to the close similarity of test conditions and geometrical parameters to the specimen tested in this thesis. In this thesis the ratio between N4 and N3 is defined as dR, Equation (20). The dR chosen as the benchmark for the comparison is 32%, as this is the most conservative.

$$dR = \frac{N4}{N3} * 100 - 100 \tag{20}$$

Table 6: Fatigue life of axially loaded tubular joint without repair

	N3 (E3)	**N4 (E3)**	**dR**
OTH	1 100	1 200	9%
OTH	630	730	16%
OTH	680	820	21%
OTH	1 000	1 300	30%
OTH	840	1 100	31%
OTH	7 500	8 500	13%
Max OTH	**760**	**1 000**	**32%**
Atteya	632	820	30%

6.2.2 Comparison of the Tested Specimen

The specimen was subjected to a lower cyclic stress range in the post-repair phase than in the pre-cracking phase. Therefore, a direct comparison to the pre-crack fatigue endurance would not be possible. Nevertheless, the cycle count to reach N3 under the post-repair stress range was estimated by shifting the SN curve to the N3 result from the pre-cracking phase, as shown in Figure 6-1. Subsequently, from this shifted S-N curve, the projected cycle count to achieve N3 under the stress range employed in the post-repair phase could be derived. Eventually, this enabled comparing the number of cycles in the post-repair phase and the estimated number of cycles to N3. The procedure employed to calculate dR is summarised as follows:

1. Pre-crack result ($\Delta P = 40kN$):
    a. $\sigma_{nom}(14.16\ MPa) \cdot SCF(19.4) = HSSr(274.7\ MPa)$
    b. Number of cycles to N3 = 1 515 000
2. Shifting the SN curve to N3 from the pre-crack phase:
    a. New log(a) = 13.50
    b. m = 3
3. Estimate of the Number of cycles to N3 under post-repair load ($\Delta P = 27kN$):
    a. $\sigma_{nom}(9.19\ MPa) \cdot SCF(19.4) = HSSr(178.24\ MPa)$
    b. Estimated number of cycles to N3 = $10^{\log(a)-m\cdot\log(\Delta\sigma)} = 5\ 546\ 000$
4. Number of cycles in the post-repair phase ($\Delta P = 27kN$):
    a. Number of cycles to run out = 3 515 000
5. **Calculating dR** = 3 515 000/ 5 546 000 = **<u>63%</u>**

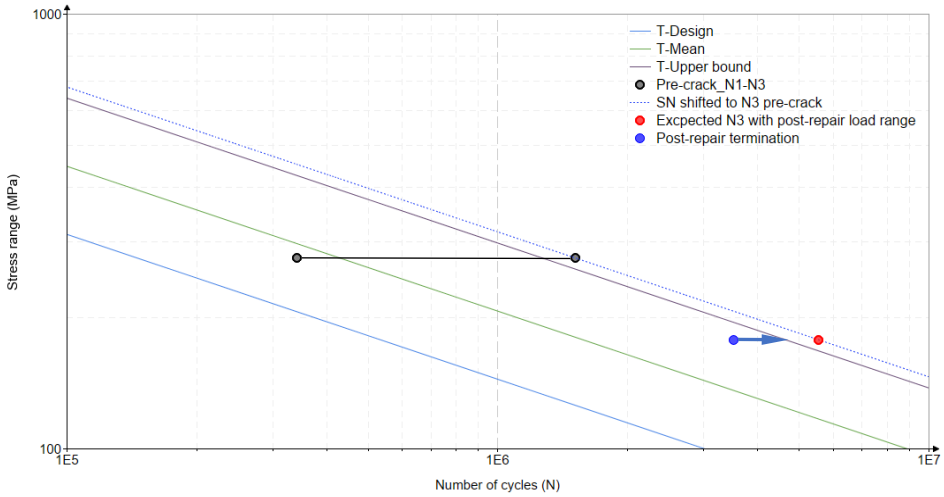

Figure 6-1: Standard SN curve and SN curve shifted to pre-crack result

The dR ratio of 63% derived from the approach employed in this section is about 100% higher than the greatest dR number for similar specimens tested without repair. Consequently, the conclusion can be drawn that drilling crack-deflecting holes combined with weld-toe grinding has successfully increased fatigue endurance. It should also be emphasised that N4 has not been reached under these loading conditions, but it was decided to stop the testing due to time limitations and that sufficient data was achieved. Furthermore, there was no sign of crack initiation or development at the point of test termination.

6.3 Stress Field and Stress Range Analysis

6.3.1 General

A study of the stresses has been carried out to facilitate an estimate of the effectiveness of the repair by comparing the stress range experienced by the specimen with the SN curve. A finite element model of the DT joint has been created to aid and validate the strain gauge placement and provide a better comprehension of the overall stress field in the specimen.

The stress range that goes along with the T-curve is the HSS range. This is obtained by linear extrapolation of the principal stresses at a distance perpendicular to the weld toe, as discussed in Section 2.3.2. Given the fact that the T-curve is developed based on testing of intact specimens and the corresponding maximum HSS range from the intact stage, it raises the question of whether the linear extrapolation technique is appropriate for repaired tubular joints. Moreover, there is a difference between the maximum principal stresses and the radial directional stresses recorded from the strain gauges as mentioned in Section 5.2.1. These questions are investigated and discussed in this section.

6.3.2 Finite Element Model of the Repaired Tubular Joint

The repaired specimen was modelled in Dassault Systems Abaqus Version 2017 with similar boundary conditions and load application as in the model of the intact specimen Section 5.2.1. The crack and holes were modelled to align with the experimental work's actual geometry and crack path. However, the model was simplified by excluding the weld profile and weld toe repair. Several analyses have been conducted with different element types and mesh refinement to reach reasonable convergence. The model used is shown in Figure 6-2 and the element type chosen was C3D8, which in this case, is belived to provided sufficient results for a reasonable computational cost. Furthermore, the plastic properties were also included in the material model in these simulations.

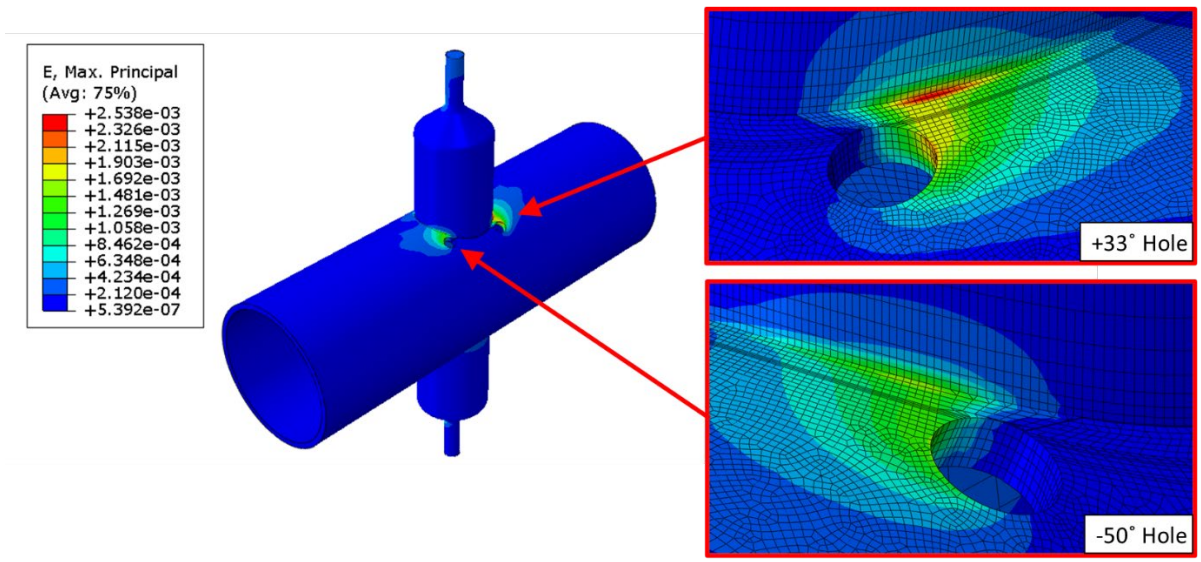

Figure 6-2: FE model of the repaired DT-joint, including the crack

6.3.3 FE-model Validation

To validate the FE model, a static general analysis was performed with five steps from 0 to 30 kN giving load increments of 6 kN between each loading step. The same exercise was performed in the experimental work to facilitate a comparison of the strain readings by increasing the load stepwise from 0 to 30 kN with increments of 6 kN. The directional strains from the FE model were extracted by assigning a local coordinate system in the position of the strain gauge, which allowed for the extraction of the surface strain in the direction corresponding to the strain gauge grid in the experimental work. Both the strain readings from the FE model and the experimental work are plotted in Figure 6-3.

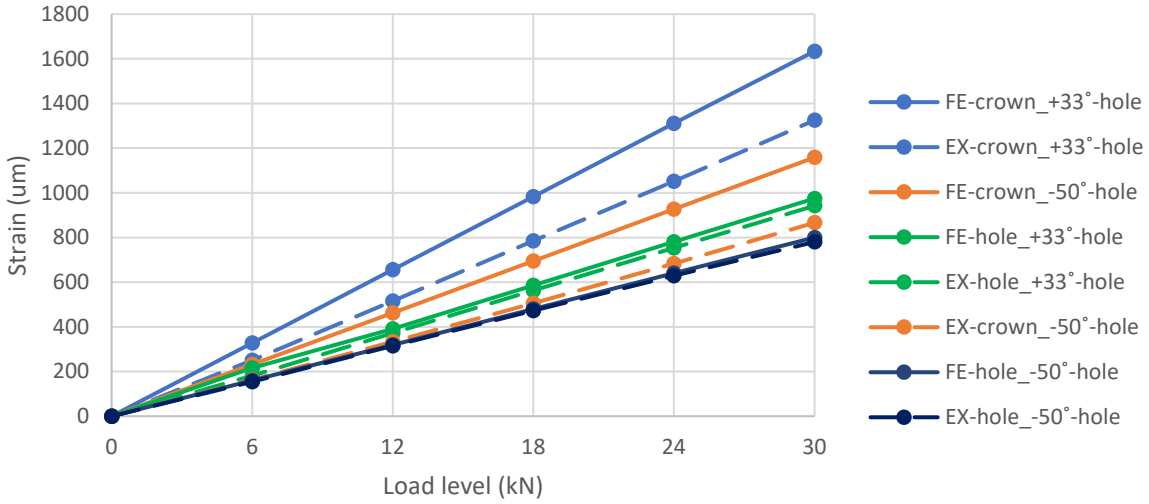

Figure 6-3: Strain readings from the FE model and SG in the experimental work for different load levels

Figure 6-3 illustrates good agreement between the strains in the FE model and experimental work for the strain gauge located next to the holes. However, for the strain gauges close to the weld toe on the crown side, there is a deviation of about 25% at the +33˚ hole and 35% at the -50˚ hole, where the FE model shows the highest strains. The source of this deviation may be due to the fact that the strain gauges were placed sufficiently close to the groove caused by the grinding to experience some shielding effects. In addition, the weld profile highly influences the strain readings, as discussed in Section 2.2.3.

As the weld profile and the subsequent weld toe repair are excluded in the FE model, there is a high probability that the weld toe repair provides a shielding effect that influences the stress flow by reducing the stresses on the surface next to the weld toe, which is not captured in the FE model. This behaviour is illustrated in a simple FE model where a groove corresponding to the weld toe profile in the experimental work is modelled on one half and excluded on the other half of the model, as shown in Figure 6-4. An axial tensile force is applied to the plates.

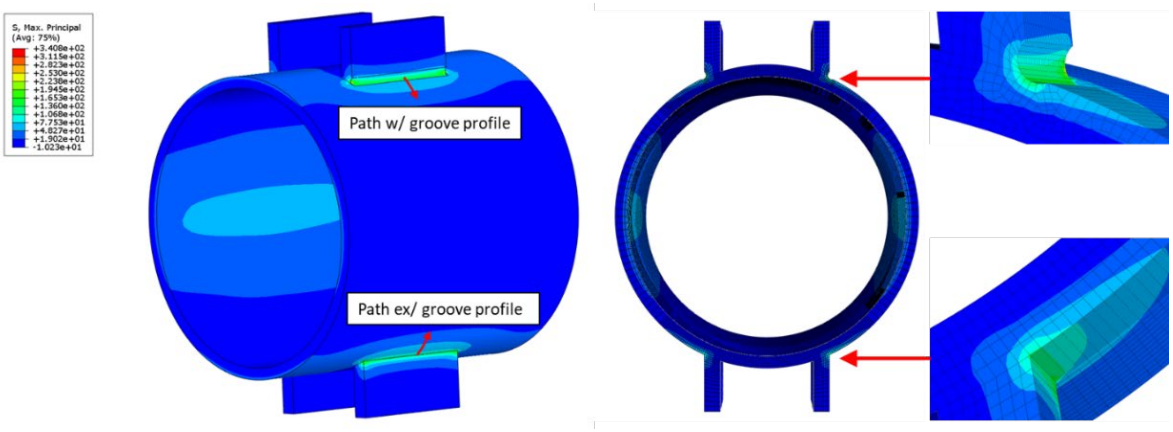

Figure 6-4: FE model of ground weld-toe profile

The directional strains along the path shown in Figure 6-4 are plotted in Figure 6-5. As seen in the plot, the groove profile reduces the surface strains close to the weld-toe to 80% of the surface strain at the same location without the groove. Atteya also observed this behaviour in his research, where a strain gauge located directly in front of a groove was inefficient in capturing the strain variation.

However, it is essential to emphasise that the 20% deviation discovered in this model cannot be directly transferred to the FE model of the repaired DT joint due to the different configurations. Nonetheless, it reasonably explains the discrepancy between the model and the experimental work. Moreover, Section 5.2.3 shows an eccentricity in the experimental specimen, a feature excluded in the FE model, contributing to the present deviation. Lastly, it is worth mentioning that the Strain gauge in the experimental work measures the average strain over an area of 3 x 3 mm, while the strains extracted from the FE model are extracted from a node (single point).

To sum up, the weld and ground weld-toe profile should be included in the numerical model to capture the actual stresses present next to the weld-toe after a weld-toe repair, as the stresses close to the weld-toe are highly sensitive to the weld profile geometrical changes. However, as this type of modelling is a demanding and meticulous process for such geometries and does not fall under the main scope of this thesis, it was decided not to be included.

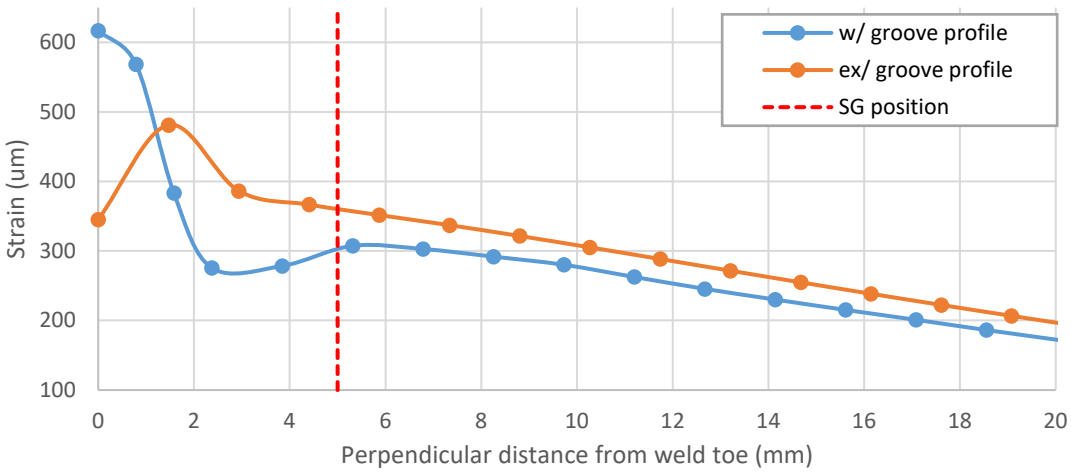

Figure 6-5: Directional strains along paths illustrated in Figure 6-4

6.3.4 Selection of the Strain Range to be used with the SN Curve

As mentioned in Section 6.3.1, several methods may be employed to determine the maximum stress range experienced by the specimen during post-repair testing. The stresses can either be directly extracted from strain gauge readings from the experimental work or directly from the corresponding location in the FE model. Furthermore, the maximum hot spot stress range may be obtained from the FE model with the linear extrapolation technic. A summary of the result from the applied methods is presented in Table 7.

In this work, the HSS was determined by designating a pathway of nodes oriented perpendicularly to the weld toe, originating from the point on the weld toe with the maximum stress, as shown in Figure 6-6. Subsequently, the technique of linear extrapolation was applied for the maximum principal and directional stresses. The directional stresses were transformed according to a local coordinate system aligning with the strain gauge position in the experimental work. Simultaneously the location of the strain gauge was examined and found to lie perfectly aligned within the path established in the FE model, thereby confirming reliable strain gauge placement in the experimental work.

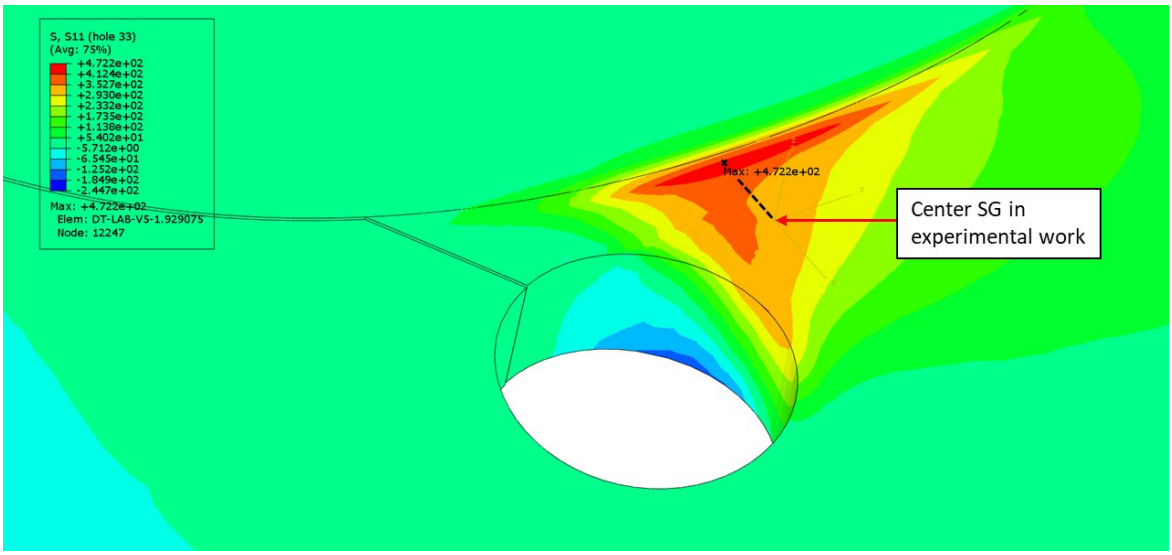

Figure 6-6: Directional stresses around +33° hole

An important observation from the derived stress ranges from the FE model is that the HSS range based on the directional stresses (366 MPa) is higher than the HSS range derived from the maximum principal stresses (329 MPa). This is unphysical due to the fact that the directional stress cannot exceed the max principal stress. However, as the directional stresses decay faster at distances from the weld toe compared to the maximum principal stresses. Hence, the linear extrapolation technique used to derive the HSS results in higher directional HSS than principal HSS. However, using the HSS derived from the principal stresses is the established method and will be used also here.

Since the test model has only one strain gauge behind the hole at the crown-side, while two strain gauges are requerd to derive the HSS by linear extrapolation. Hence, the FE model has been used to establish a relationship between the HSS derived from the principal stresses and the stress at the strain gauge location, and this relationship has been used to scale the strain gauge readings. The scaling factor was found to be 1.08 based on the stresses shown in Table 7. As a result, the stress range readings at the strain gauge of 250 MPa is scaled to 269 MPa as the assumed HSS.

Table 7: Summary of the derived stress ranges

FE MODEL		EXPERIMENTAL TEST	
Method	**Δσ**	**Method**	**Δσ**
Direct extraction from SG location	305 MPa	Direct extraction from SG**	250 MPa
HSS range (Max Principal stress)	329 MPa	SG x 1.08*	269 MPa

**Factor of 1.08, derived by dividing HSS range from max principal stress by the directional stress at the SG location in the FE model to estimate the HSS range adjusted to SG readings from experimental work.*
***The stress range is extracted after a full trough-thickness crack was achieved between the holes*

6.4 Repair's Effectiveness First Attempt Based Comparison with SN curve

6.4.1 Cycle Count in First Attempt Post-Repair Testing

In the first attempt of the post-repair testing, the specimen underwent 3 515 000 cycles until defined as a run-out. However, it took 930 000 cycles to achieve a through-thickness crack between the crack deflecting holes, in which the crown side strain gauge location where the new crack was expected to occur was subjected to a variable stress range as the crack propagated.

To evaluate the accumulated damage during these first 930 000 cycles and its relevance for the fatigue life of this location, an equivalent stress range for these cycles was calculated, and the resulting damage was established based on the SN curve. This damage is then used further to determine the equivalent number of cycles this part of the test represents, correcting for the stress level at this location after through thickness between the crack deflecting holes.

The time series Figure 6-7 from the strain gauge at the +33˚ hole crown side was exported to the programming software MATLAB by MathWorks. Here the number of cycles at each stress range was counted through the well-known Rain-flow counting algorithm. Then the equivalent stress range for these cycles was calculated with the following Equation (21):

$$\Delta\sigma_E = \left[\frac{\sum_{i=1}^{n} n_i \cdot \Delta\sigma_i^m}{\sum_{i=1}^{n} n_i}\right]^{\frac{1}{m}} \quad (21)$$

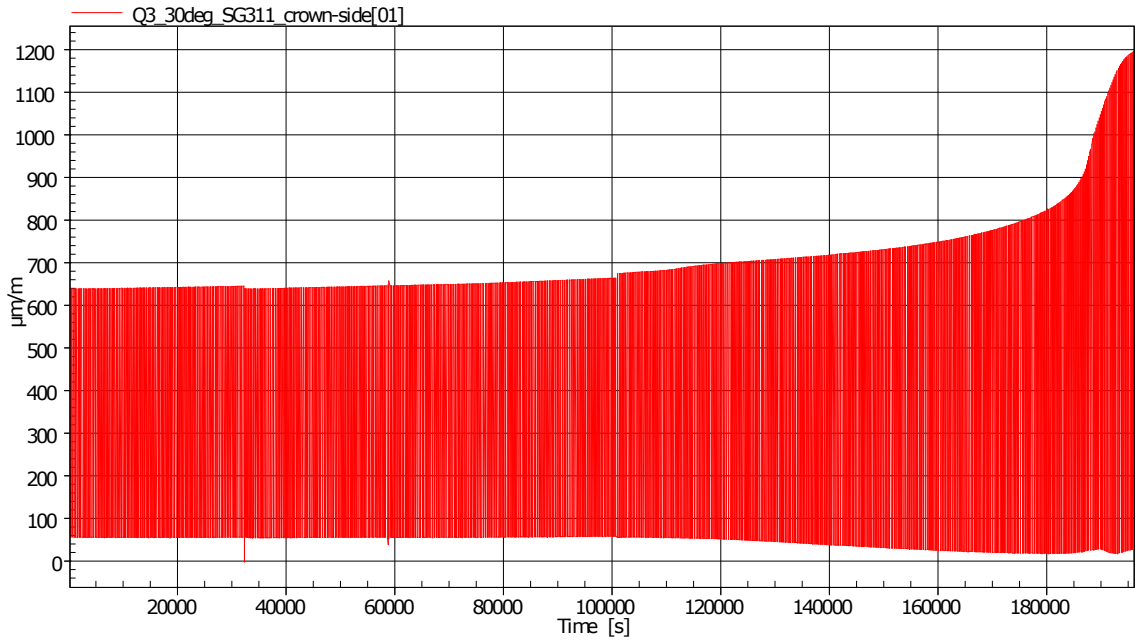

Figure 6-7: Time series of the first 930 000 cycles 1st attempt post-repair SG crown-side +33 hole

The resulting equivalent stress range and cycle count were determined to be 135 MPa and 969 000 cycles, respectively. It is worth highlighting that the cycle count from the Rain-flow counting exceeds the number of cycles applied by the test machine. The cause of this discrepancy is found in the timing of the strain recordings. Specifically, the recording of strain measurements commences prior to the initiation of the load cycles by the testing machine and concludes after the completion of a round of applied load cycles. Hence, the stress fluctuation during the intervals when no load cycles are being actively applied is unfortunately counted, as shown in Figure 6-8. However, by removing all cycle counts with a stress range of less than 0.3 MPa, the total number of cycles counted is 830 000 with an equivalent stress range of 143.5 MPa, which aligns with the applied number of cycles by the test machine.

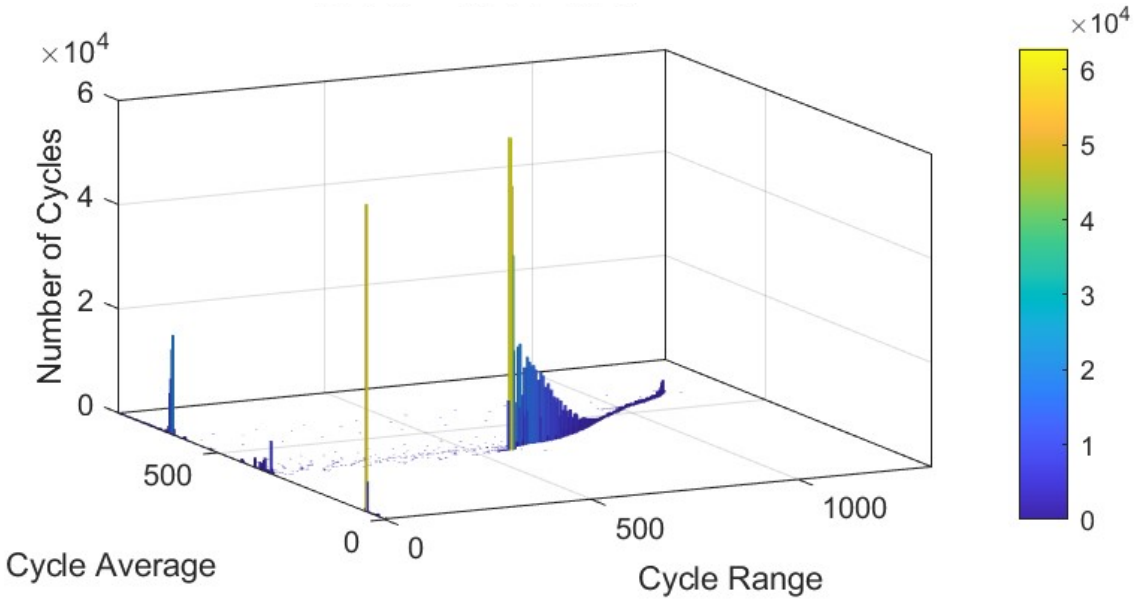

Figure 6-8: Rainflow matrix histogram (w/strain range in µm) of time-series Figure 6-7

As presented in Section 5.4.2, the strain recording of 100 000 cycles was lost during the first 930 000 cycles, particularly the cycles from 365 000 to 465 000. Thus, these cycles were not included in the time series and subsequent Rain-flow counting above. The recorded stress range at 365 000 and 465 000 cycles were 125 MPa and 128 MPa, respectively. The lowest of the two stress ranges was chosen to calculate the damage during the lost 100 000 cycles.

An overview of the procedure employed to calculate the number of cycles corresponding to a stress range of 269 MPa in the first attempt post-repair testing is presented in Figure 6-9.

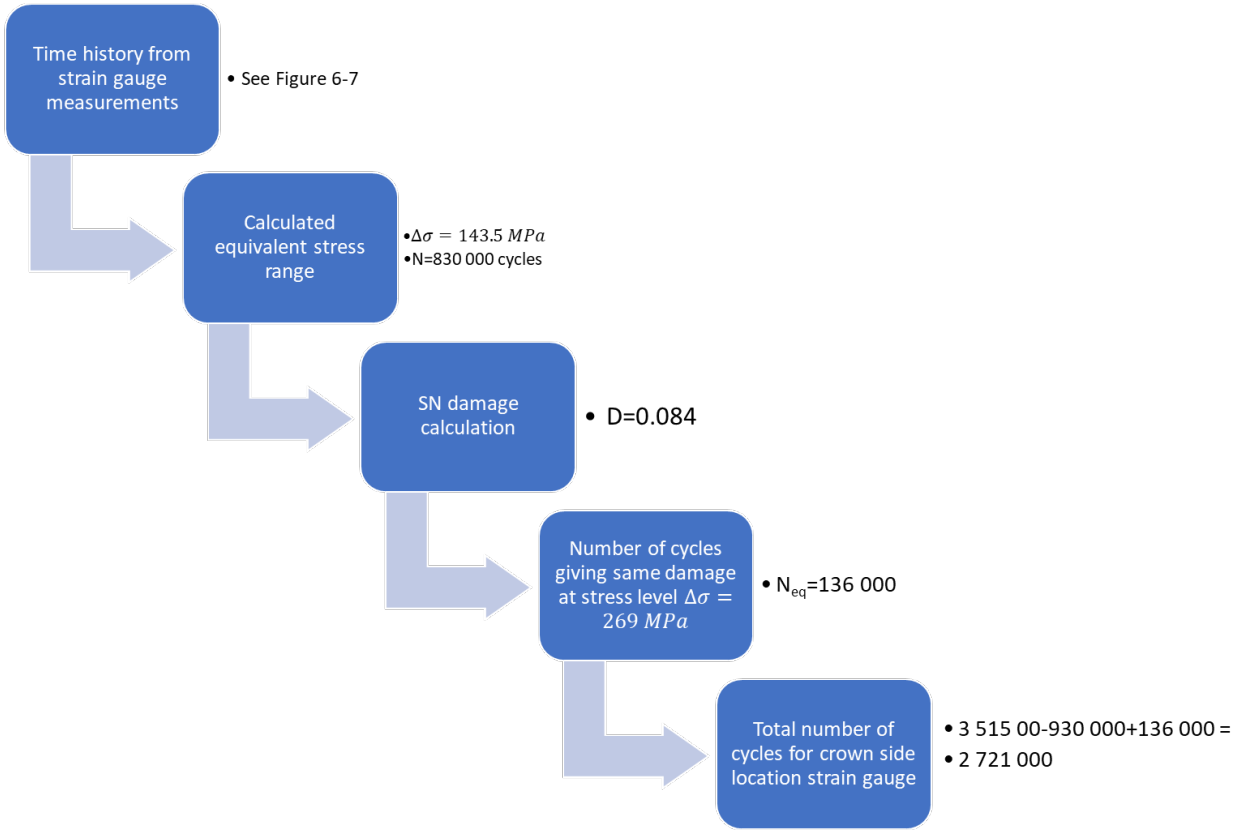

Figure 6-9: Calculation prosses to estimate the number of cycles in post-repair testing with Δσ = 269 MPa

6.4.2 Comparison With SN curve

The basis for the comparison is 2.7 million cycles with a stress range of 269 MPa. Considering this result, it is immediately evident that the fatigue endurance in the post-repair testing is significantly higher than the upper bound of the T curve, which sets the basis for discussing the weld-toe grinding effect.

Both DNV-RP-C203 and BS 7608 provide an improved SN curve for welded connection subjected to weld toe grinding, as presented in Figure 6-10. By comparing the number of cycles from the design T curve with the improved SN curves, it is possible to derive an improvement factor of the weld toe grinding from DNV and BS for the given stress range of 269 MPa.

- Improved fatigue life according to DNV = 1.6
- Improved fatigue life according to BS = 2.0

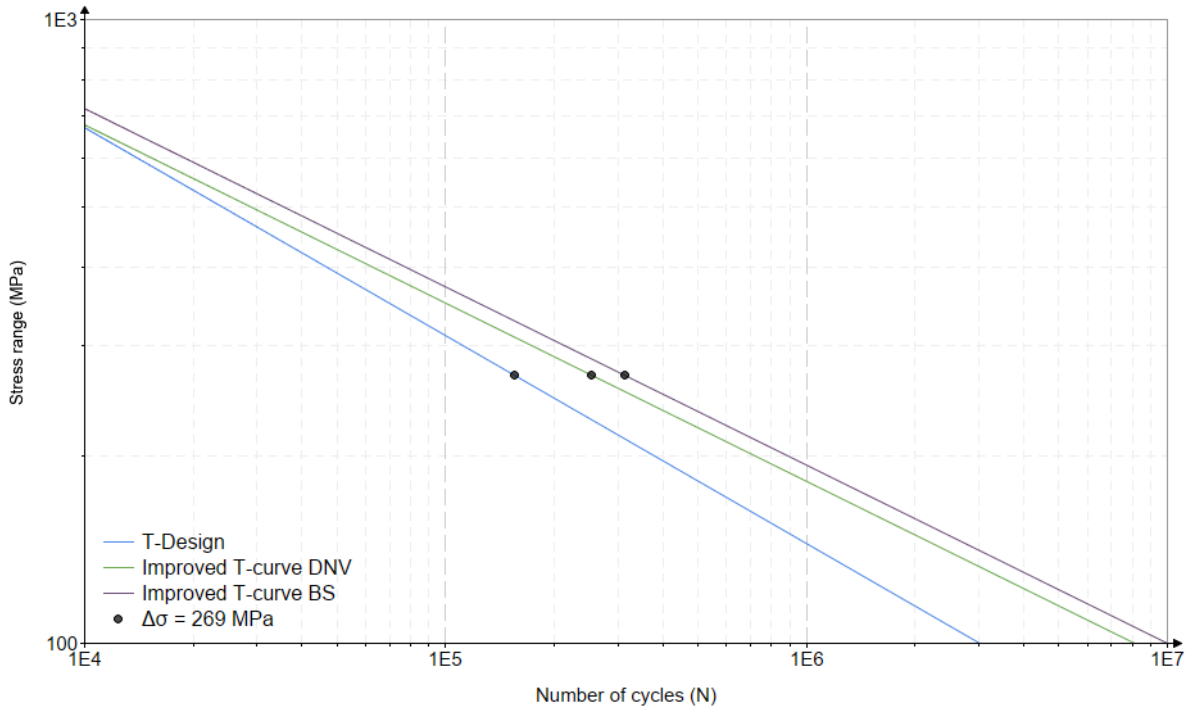

Figure 6-10: Improved SN curve from weld-toe grinding

The reason for deriving these improvement factors, as opposed to simply extracting the number of cycles from the SN curves, is to enable the consideration of the fatigue endurance during the pre-cracking phase in the comparison. By utilising the SN curve shifted to the pre-crack result, the following number of cycles is expected:

- No improvement from weld-toe grinding: 1 616 000 cycles
- Improvement from grinding according to DNV: 2 636 000 cycles
- Improvement from grinding according to BS: 3 227 000 cycles
- **Number of cycles to run out in post-repair testing: 2 721 000 cycles**

It is evident from these considerations that the weld-toe grinding successfully increased the specimen's fatigue endurance. The number of cycles in the first attempt of the post-repair testing excided the number of cycles expected according to DNV when improved with weld toe grinding.

6.5 Repair's Effectiveness Second Attempt and Reverse Coalescence

The second attempt post-repair testing results are plotted on the SN curve in Figure 6-11. It was observed that the stress range at the +33 hole was classified as high-stress low cycle fatigue. Hence the SN curve for low cycle fatigue was plotted according to NORSOK N-006. This standard, however, only provides the design curve. Thus, an assumed mean and upper bound was obtained by parallel shifting the design curve to the point where it coincided with the mean and upper bound SN curve for high cycle fatigue at 100 000 cycles.

The -50 hole was subjected to a variable stress amplitude, as the stress range started to increase at the point of crack initiation at the +33 hole and kept increasing while the crack propagated at the +33 hole. To calculate the equivalent stress range upon reaching N1 at the -50 hole, the method utilised in Section 6.4.1 was applied, which gave an equivalent stress range and cycle count of 436 MPa and 212 000 cycles, respectively.

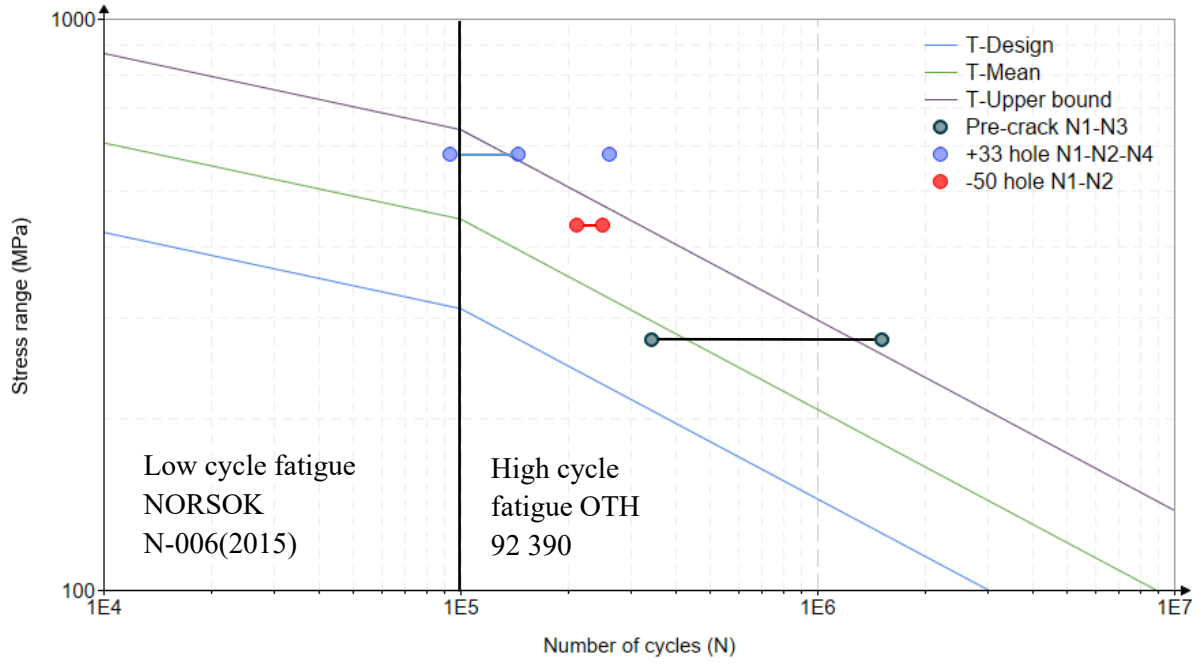

Figure 6-11: Result from testing plotted on standard SN curve

In the second post-repair testing attempt, it was observed that the new crack development at both crack-deflecting holes initiated in front of the strain gauge at the crown side, which affirmed the precision of the gauge placements. Furthermore, this observation also provided empirical evidence supporting Atteya's earlier finding of the reverse coalescence phenomenon presented in Section 5.5.2.

Another important observation in the 2nd attempt of post-repair testing was that the specimen behaved as if it had not undergone any damage during the 1st attempt post-repair testing. Considering Atteya's findings and testing results for similar stress levels, and the fact that the specimen's fatigue endurance is on the upper bound of the SN curve (as seen in Figure 6-11), it implies that the specimen did not undergo any considerable fatigue damage during 1st attempt post-repair testing (high cycle fatigue condition).

Furthermore, the results also confirm that the repair method investigated is less effective when plastic strain is present, which was expected. It is well known in fatigue analysis that microcracks may initiate due to slip steps, inclusions and extrusions at sufficiently high alternating plastic strain amplitude even if no notches, inclusions or stress riser are present (ASM International Handbook Committee, 1996).

7 Conclusion and further work

7.1 Conclusion

Due to the lack of effective temporary repair methods for cracked tubular joints in offshore jacket structures subjected to high cycle fatigue, this thesis aimed to investigate the effectiveness of a simple repair technique. Specifically, crack-deflecting holes in combination with weld-toe grinding. To achieve this objective, an experimental study of the repair method has been carried out, supplemented by a numerical analysis of the stresses and stress fields in the experimental work.

A single, double T (DT) – Joint was experimentally investigated through a three-phased fatigue testing program comprising pre-cracking, repair and post-repair testing. After a through-thickness crack was achieved in the pre-cracking phase, the cracked specimen was repaired with crack-deflecting holes and weld-toe grinding according to DNV specifications. Moreover, the testing was conducted within low-stress high-cycle fatigue conditions.

In the post-repair testing, the crack was successfully arrested in the crack-deflecting holes. Furthermore, as no sign of new crack formation was detected after an improved fatigue endurance was evident, the testing was terminated and defined as run-out. The results were compared to existing test results and SN curves, which clearly showed a significant fatigue life enhancement.

Due to run-out and no sign of new crack formation during the post-repair testing, a 2nd attempt post-repair testing was conducted. The subsequent testing applied a significantly higher load range yielding stress ranges characterised by high-stress low cycle fatigue. Under this increased stress range, new cracks initiated beyond the holes and propagated back into the hole reversely, which confirmed the reverse coalescence phenomenon discovered by Atteya. Another important observation from this testing phase was that the specimen behaved as if no damage had been induced during the 1st attempt post-repair testing.

In the author's view, the crack deflection holes combined with the weld-toe grinding successfully managed to delay the crack initiation in the 1st attempt of post-repair testing. This is a result of the reduced stress concentration due to the holes and weld-toe profile improvement, and the improved surface roughness from the grinding and sanding at the weld-toe. However, as the load range was increased in the 2nd post-repair testing attempt, the repair no longer succeeded in maintaining a sufficiently low-stress range, leading to plastic strain and stress amplitudes and subsequent crack initiation. Hence, the weld toe-grinding had a limited enhancement on the specimen's fatigue life under such plastic strain amplitudes.

Based on the results and findings in this thesis, the following conclusion is drawn:

> *Crack-deflecting holes combined with weld-toe grinding effectively extended the fatigue life of the tested cracked DT joint subjected to cyclic axial loading under stress ranges characterised by high cycle fatigue in air conditions.*

Given the considerable variation and substantial uncertainties associated with fatigue analysis, a single test cannot definitively establish fatigue-related behaviours. However, in light of existing testing and the findings within this thesis, the effect of the studied repair method appears very promising.

7.2 Further work

As the experimental results indicated a significant fatigue life enhancement of tubular joints repaired with crack-deflection holes combined with weld-toe grinding, future research should focus on providing more empirical evidence on the method by investigating the effects of the repair on:

- Different joint configurations, e.g. T-joints, K-joints, and Y- joints
- Joints with different diameter and wall thickness ratios
- Joints subjected to different cyclic loading modes, e.g. In-plane and out-of-plane bending
- Joints in seawater with chaotic protection and free corrosion

Considering the crack initiation beyond the holes and the reverse coalescence phenomenon in the post-repair testing, future work should also focus on optimizing the cut-out repair, as already stated by Attaya (Atteya, to be published). An optimal hole shape, size and placement would decrease the stress concentration even further, making the repair method efficient for tubular joints subjected to higher nominal stress ranges and more extensive degradation.

8 References

Almar-Næss, A. (1985). *Fatigue handbook : offshore steel structures*. Tapir.

ASM International Handbook Committee. (1996). *ASM handbook : Vol. 19 : Fatigue and fracture*. ASM International.

ASTM. (2019). A370 − 19 Edition September 2019. In: ASTM INTERNATIONAL.

Atteya, M. (to be published). *PhD thesis -Crack Arresting using Cutout Repair in Tubular Offshore Joints* University of Stavanger.

Atteya, M., Mikkelsen, O., G. Pavlou, D., & Ersdal, G. (2020). Crack Arresting With Crack Deflecting Holes in Steel Plates. ASME 2020 39th International Conference on Ocean, Offshore and Arctic Engineering,

Atteya, M., Mikkelsen, O., Wintle, J., & Ersdal, G. (2021). Experimental and numerical study of the elastic SCF of tubular joints. *Materials*, *14*(15), 4220.

AWS. (2017). *AWS Releases New Edition of D3.6M*. American Welding Society. https://awo.aws.org/2017/06/aws-releases-a-new-edition-of-d3-6m-underwater-welding-code/

Braun, M., & Wang, X. (2021). A review of fatigue test data on weld toe grinding and weld profiling. *International Journal of Fatigue 145*. https://doi.org/10.1016/j.ijfatigue.2020.106073

British Standard. (2015). BS 7608:2014+A1:2015 - Guide to fatigue design and assessment of steel products. In: BSI Standards Publication.

BS EN ISO. (2007). BS EN ISO 19902:2007+A1:2013-Petroleum and natural gas industries — Fixed steel offshore structures. In: British Standard

Callister, W. D., & Rethwisch, D. G. (2020). *Materials science and engineering : an introduction* (10th , global ed.). Wiley.

CIRIA, U. E. G. (1985). *Design of Tubular Joints for Offshore Structures: Part E, Material selection, fabrication and non-destructive examination ; Part F, Complex welded, cast and composite joints*. UEG. https://books.google.no/books?id=lEa3zAEACAAJ

Cottrell, A. H., & Hull, D. (1957). Extrusion and intrusion by cyclic slip in copper. *Proceedings of the Royal Society of London. Series A. Mathematical and Physical Sciences*, *242*(1229), 211-213.

DNV. (2019). DNV-RP-C203 - Fatigue design of offshore steel structures. In: DNV AS.

Efthymiou, M. (1988). Development of SCF formulae and generalised influence functions for use in fatigue analysis. in Recent development in tubular joints technology,. In: Surrey UK,.

Ersdal, G., Sharp, J. V., & Stacey, A. (2019). *Ageing and Life Extension of Offshore Structures: The Challenge of Managing Structural Integrity*. Newark: John Wiley & Sons, Incorporated.

HSE. (1997). *OTH 354 Stress Consentration Factors for Simple Tubular Joints - Assessment of Existing and Development of New Parametric Formulae*. Lloyd's Register of Shipping 71 Fenchurch Street London UK.

HSE. (1999). *OTH 92390 Background to new fatigue design guidance for steel joints and connections in offshore structures*. Health & Safety Executive London UK.

Lotsberg, I. (2016). *Fatigue Design of Marine Structures*. Cambridge: Cambridge University Press. https://doi.org/10.1017/CBO9781316343982

Makabe, C., Murdani, A., Kuniyoshi, K., Irei, Y., & Saimoto, A. (2009). Crack-growth arrest by redirecting crack growth by drilling stop holes and inserting pins into them. *Engineering Failure Analysis*, *16*(1), 475-483.

MTD. (1989). *Underwater Inspection of Steel Offshore Installations: Implementation of a New Approach*. Report number 89/104. MTD London UK.
MTD. (1994). *Review of Repairs to Offshore Structures and Pipelines*. Publication 94/102 MTD London UK.
MTS. (n.d.). *Series 809 Axial/Torsional Test Systems*. MTS. https://www.mts.com/en/products/materials/dynamic-materials-test-systems/series-809-at-test-systems
PMB. (1988). *AIM III Assessment Inspection Maintenance*. Published as MMS TAP report 106ap.
Profdivers. (n.d.). *Underwater Hyperbaric welding*. Professional Diving Services. https://www.profdivers.com/underwater-welding/underwater-hyperbaric-welding/
Saini, D. S., Karmakar, D., & Ray-Chaudhuri, S. (2016). A review of stress concentration factors in tubular and non-tubular joints for design of offshore installations. *Journal of Ocean Engineering and Science*, *1*(3), 186-202.
Sharp, J. V., & Ersdal, G. (2021). *Underwater inspection and repair for offshore structures*. John Wiley & Sons, Inc.
Sharp, J. V., Stacey, A., & Birkinshaw, M. (1995). *Review of Data for Structural Damage to Offshore Structures* 4th Intern. ERA Conference, London, Dec.1995.
Standard Norge. (2015). NORSOK standard N-006 Assessment of structural integrity for existing offshore load-bearing structures. In: Standard Norge.
Trident. (2023). *Grouting Services*. Trident Group. https://trident-gp.com/en/services/view/21
Tubby, P. (1989). *OTH 89 370 Fatigue performance of repaired tubular joints*. Department of Energy: Her Majesty's Stationery Office London.
Tweed, J. H., & Freeman, J. H. (1987). *OTH 87 259 Remaining Life of Defective Tubular Joints - An Assessment Based on Data for Surface Crack Growth in Tubular Joints Fatigue Tests*.
Upmold. (2017). *Surface finish sandpaper grit chart*. https://upmold.com/surface-finish-sandpaper-grit-chart/
Waegter, J. (2009). Stress concentrations in simple tubular joints. In.

Appendix A Material Properties

Attachment 1 – Tensile Coupon Testing

A total of eight tensile coupon tests of the pipes used in the fatigue test were conducted at the UiS workshop in INSTRON 5985 Dual Column Floor Frames tensile test machine. The specimens were constructed according to ASTM A370 (ASTM, 2019). The 3/4" specimens were cut out from the brace pipe D114.3 and the 1" specimens were cut out from the chord pipe D219.1.

It is important to note that the machine is not certified and the pipe thickness is not constant, with a variation of 1% to 4% between min and max thickness within a single specimen.

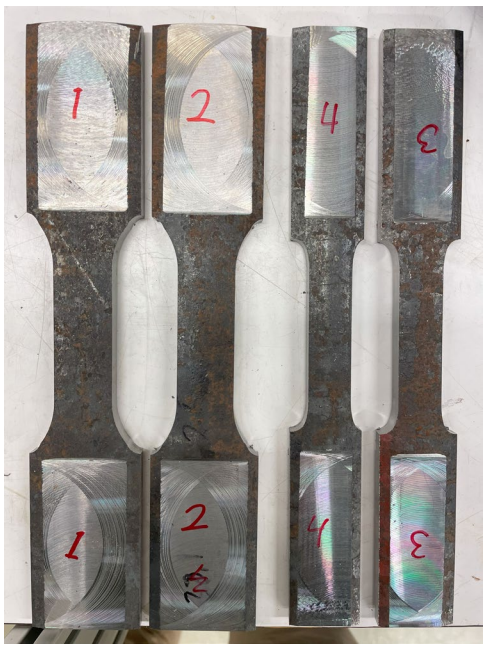

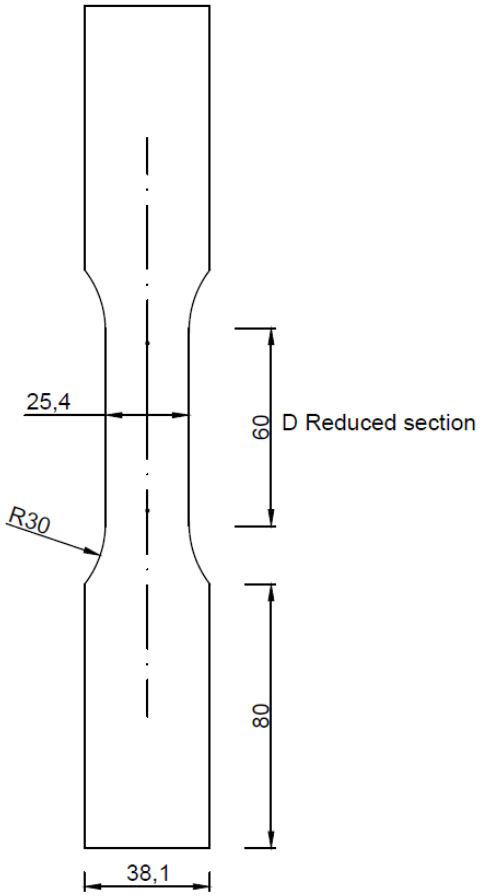

Pipe no. 2 D219.10 x t8.20 mm

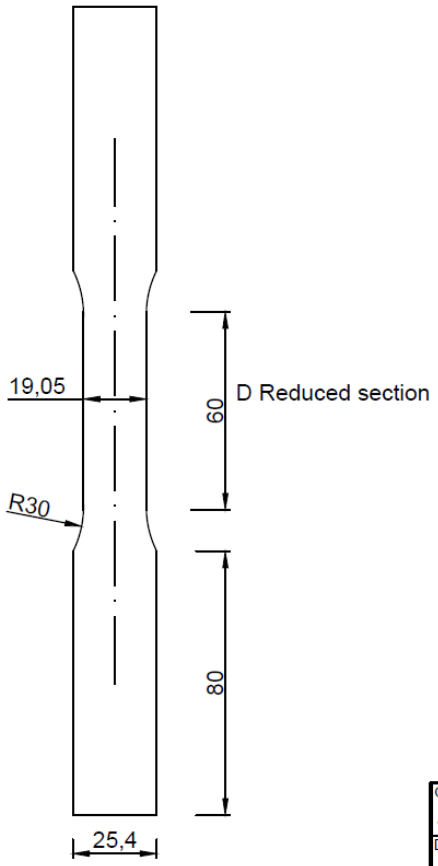

Pipe no. 1 D114,3 x t8,56 mm

Qty	TENSILE COUPON SPECIMENS				
4					
Designed	Checked	Approved Date	Drawn Date	Scale	Sheet size
SR			27.02.2023	1:2	A4
IMBM-UIS		Part number	Material		
			S355 G14 + N		
		Drawing number		Edition	Sheet
				01	1/1

Specimen label	Modulus (Automatic Young's) [GPa]	Tensile stress at Yield (EN\\ISO lower yield) [MPa]	Tensile stress at Yield (EN\\ISO upper yield) [MPa]	Tensile stress at Yield (Offset 0.2 %) [MPa]	Tensile stress at Tensile strength [MPa]	Tensile stress at Break (Standard) [MPa]	% Elongation at tensile strength at Nonproportional elongation (Standard) [%]	% Elongation at break at Nonproportional elongation (Standard) [%]
3/4" - 1	191.16	389.54	396.49	391.4	535.53	347.64	23.23	44.73
3/4" - 2	347.02	414.6	422.29	380.98	543.13	363.91	22.69	40.71
3/4" - 3	202.15	414.1	423.37	394.21	544.15	357.27	22.73	42.74
3/4" - 4	245.96	400.92	403.18	400.39	535.22	358.04	25.22	44.37
Mean	246.57	404.79	411.33	391.74	539.51	356.71	23.47	43.14
STD	71.02	11.98	13.56	8.1	4.79	6.74	1.19	1.84

Specimen label	Modulus (Automatic Young's) [GPa]	Tensile stress at Yield (EN\\ISO lower yield) [MPa]	Tensile stress at Yield (EN\\ISO upper yield) [MPa]	Tensile stress at Yield (Offset 0.2 %) [MPa]	Tensile stress at Tensile strength [MPa]	Tensile stress at Break (Standard) [MPa]	% Elongation at tensile strength at Nonproportional elongation (Standard) [%]	% Elongation at break at Nonproportional elongation (Standard) [%]
1" - 1	211.03	-	-	381.16	510.69	356.06	22.61	40.96
1" - 2	229.2	387.61	394.89	387.42	518.87	359.12	23.82	43.54
1" - 3	221.28	390.84	398.66	379.53	512.87	355.49	24.14	43.51
1" - 4	-	-	-	391.24	524.86	355.81	24.51	43.81
Mean	220.50	-	-	384.84	516.82	356.62	23.77	42.96
STD	9.11			5.46	6.38	1.68	0.82	1.34

Stress strain curve of ¾" coupon test specimen from brace pipe D114.3mm

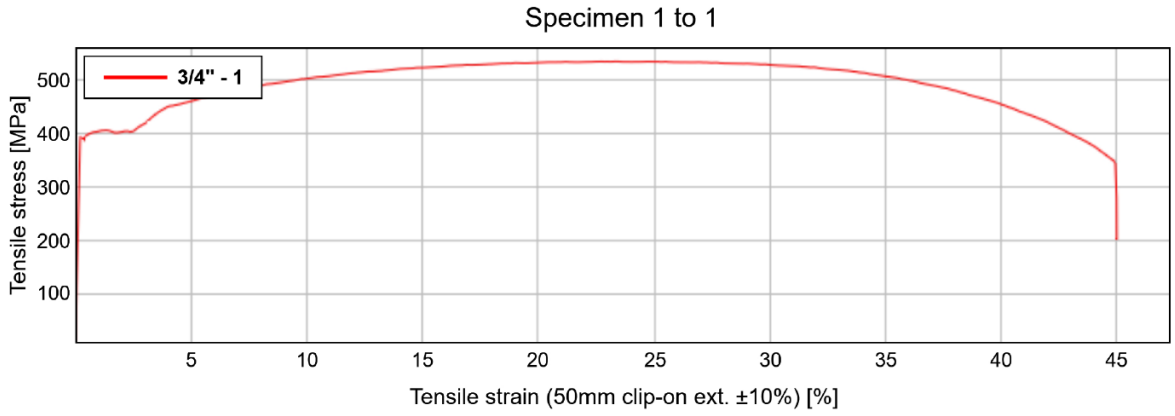

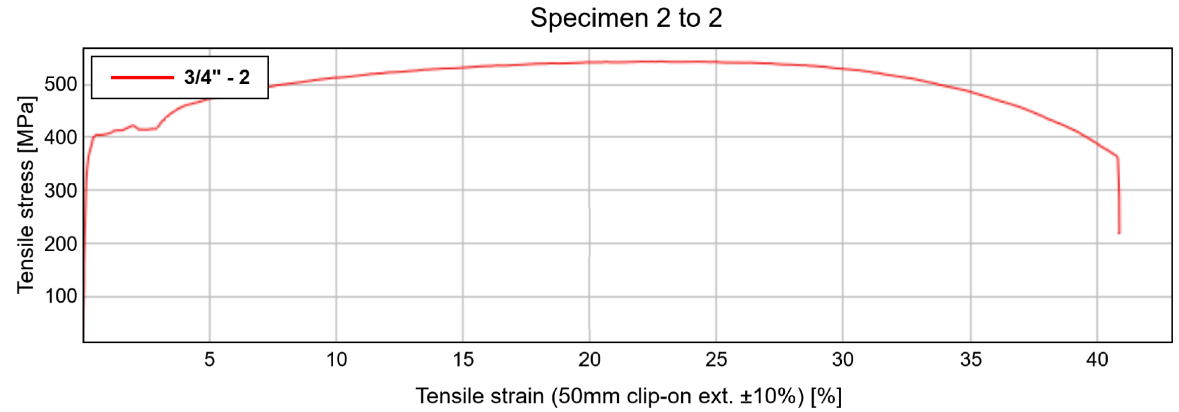

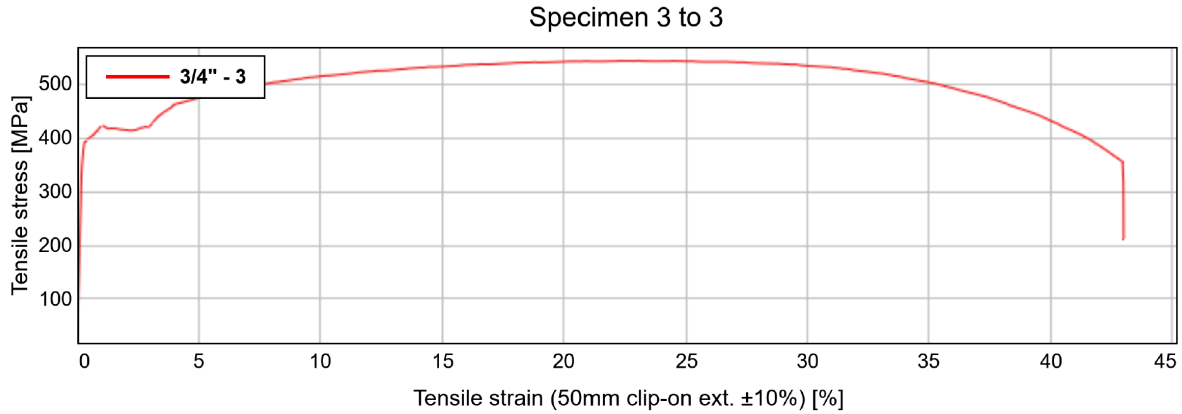

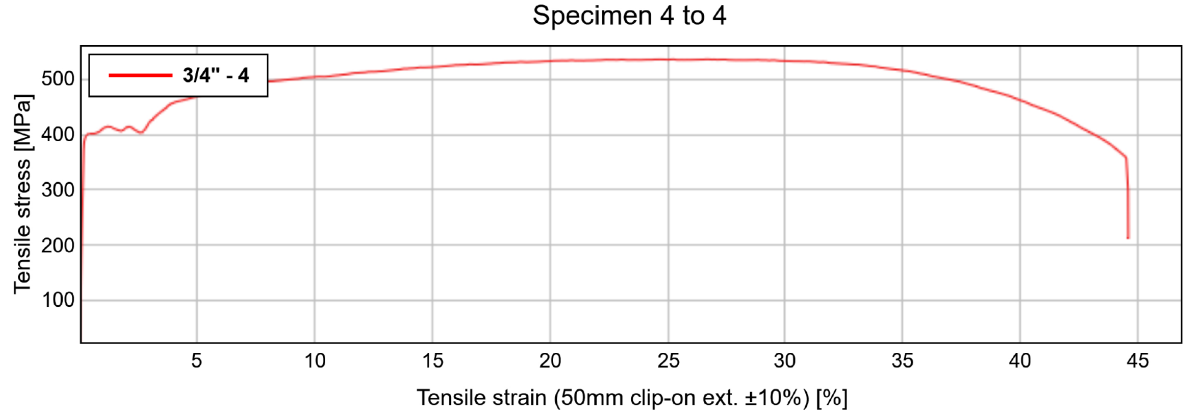

Stress strain curve of 1” coupon test specimen from chord pipe D219.10mm

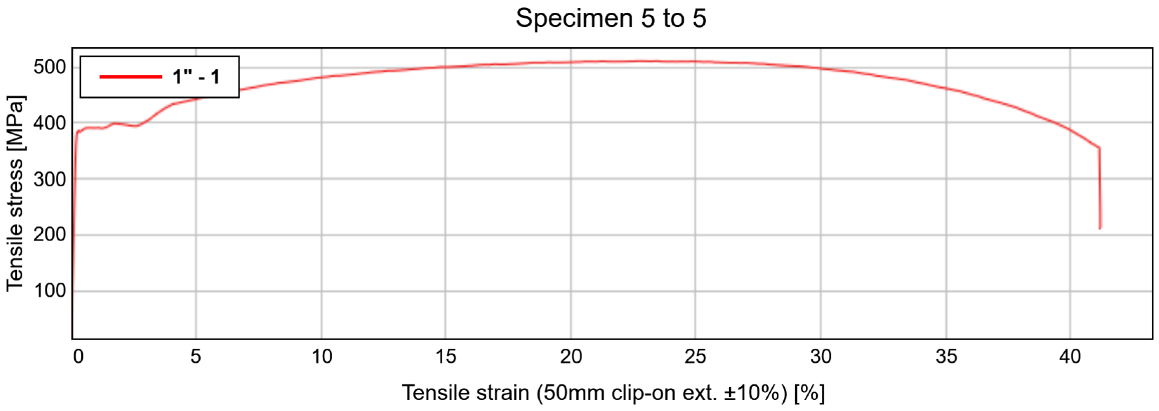

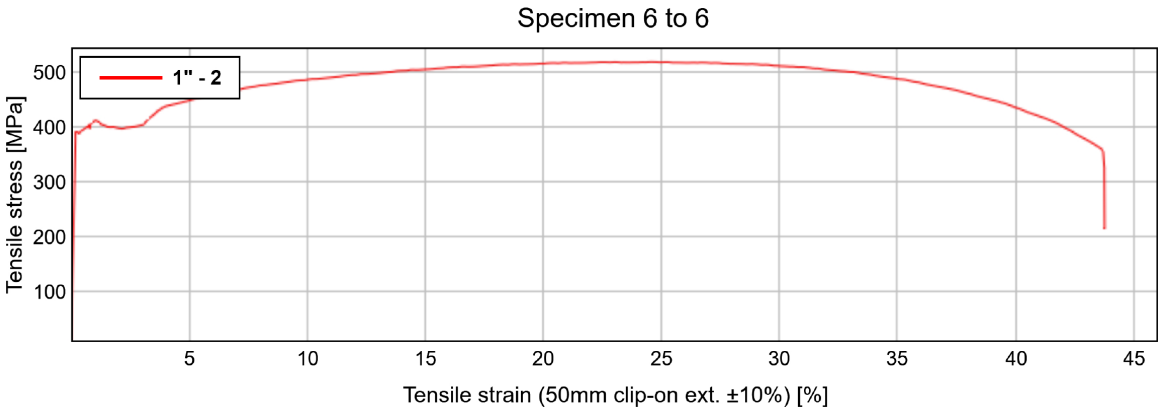

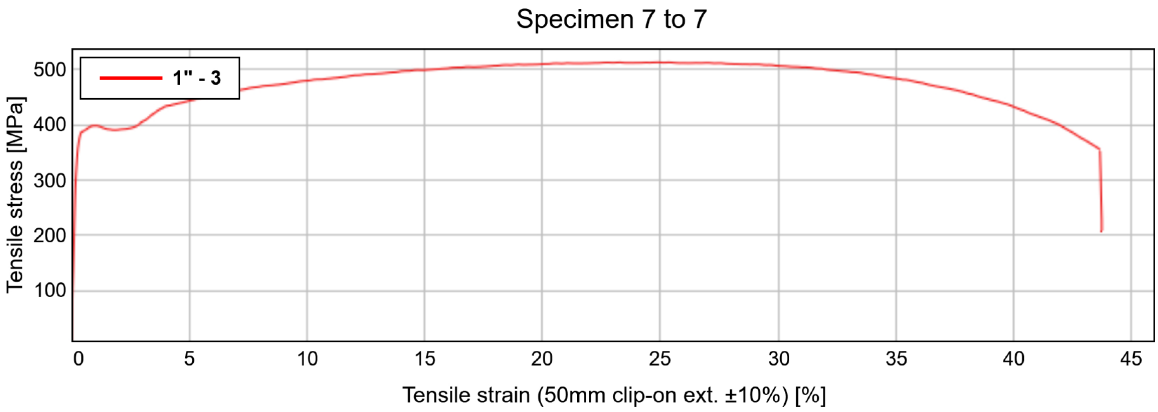

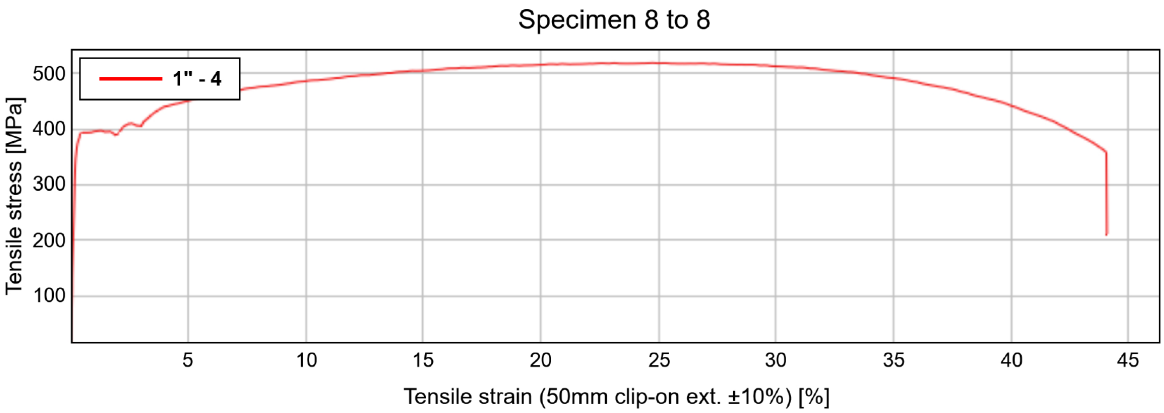

Attachment 2 – Material Certificate

Brødrene Dahl AS
Brynsengv 5
N-0667 Oslo
NORWAY
NO 945 757 280 MVA
www.dahl.no

Certificate Dept
sertifikatkontoret@dahl.no
Tel +47 22 72 54 32

Print date: 2023-02-21

Your order:
Contact person:
Customer's ref:
Project:
Sales order:
Print date: 2023-02-21

Certificate List

Sales Order #	Customer Order #	Item #	Qty	Heat #	Code #	Article #	Item Text #1	Item Text #2	Cert. #
		P-2	0	50747K		1093352			2023010391458
		P-2	0	1202570		1093361			2020100767556

Item #	Heat #	Code #	Item Text #1	Item Text #2
P-2	50747K			

BRØDRENE DAHL

LIBERTY

A02 **Inspection certificate "3.1" (EN 10 204)**

A03 Document No.: **20015/23**

A07	Customer's Order (P.O.) No./Item No.: **50120958**	A08	Manufacturer's Works Order No.: **25390/0/22**
A11	Supplier's Order No.: **3151019814**	A10	Advice - Note No.: **8150094760**
B08, B12/13	Quantity delivered: B13 Actual mass pcs / mtrs / kgs bdls / feet / lbs **28** / **170,870** / **3834**	A06	Customer / Consignee: **BRODRENE DAHL A/S** **ETTERSTAD P.B. 6146** **0602 OSLO** **Norway**
B09-11	Dimensions: ART.NO.: 1093352 **114,3 x 8,56 mm (4"SCH80)**		
B02	Steel designation: **S355G14+N S355G15+N L360N/X52N PSL2 S355NLH**		

B01,B03, B04 Product, conditions and terms of delivery:

Hot finished hollow sections / Seamless steel tubes / Structural hollow sections,
ASME B36.10M-18, EN 10225-09, EN 10210-1/06, 2/19 (CE),
ISO 3183-19, API Spec.5L-46th edit.18 PSL2 – PED 2014/68/EU Annex I. part 4.3,
ANSI/NACE MR0175/ISO 15156-2:2015 Annex A 2.1.2., ANSI/NACE MR0103/ISO 17945-15.
NORSOK MDS C22 Rev.5,October 2013, NORSOK Y 27 Rev.4: 06-2007 S355G14+N to EN 10225:2009,
NORSOK Y 22 Rev.5: 06-2007 S355G15+N to EN 10225:2009
Normalized hot finished. BRODRENE DAHL Specification, NORWAY 23.05.2019

A04, B06 Marking: Manufacturer's mark, mill inspector's stamp

LO (1) (2) CE 07 0045-CPR-0807-1 LO a.s. LO-009-CPR2020-01-06 EN 10210:2006 S355NLH/1.0549

C71-92 Heat (H) and product (P) chemical analyses (%) C70 Steel made by basic oxygen process, fully killed, strand cast.

B07 Heat No.:	C	MN	SI	P	S	CU	NI	CR	ALt	N	MO	V	TI	NB	B
P-2 **50747K**	**0,15**	**1,22**	**0,318**	**0,016**	**0,002**	**0,08**	**0,03**	**0,04**	**0,029**	**0,0097**	**0,009**	**0,064**	**0,002**	**<0,003**	**0,0003**
	0,15	1,22	0,316	0,015	0,002	0,08	0,03	0,04	0,031	0,0067	0,008	0,065	0,002	<0,001	0,0003
	0,15	1,24	0,321	0,015	0,002	0,08	0,03	0,04	0,032	0,0070	0,009	0,065	0,002	<0,001	0,0003
											AS	SB	PB	BI	CEQ
50747K H											**0,003**	**0,000**	**0,000**	**0,000**	**0,38**
P											0,003	<0,001	0,001	0,000	0,38
P											0,003	0,001	0,002	0,000	0,38

Z99

B07 Heat No. C00 Specimen No.			C11 Yield Point MPa	C12 Tensile Strength MPa	C13 Elongation %	YP/TS	C40-43 Impact test				C30-32 Hardness HRB
C04 Requirements:	**L360N/X52N**		**360 - 530**	**460 - 760**	**min. 23,0** (2")		**A) L-5-27J / -46°C**				**max. 99**
							B) INF. Shear Area (%)				
	S355G14+N, S355G15+N		**min. 355**	**460 - 620**	**min. 22,0** (A_5)	**max. 0,88**	**C) L-5-25J / -40°C**				
	S355NLH		**min. 355**	**470 - 630**	**min. 22,0** (A_5)		**D) L-5-33J / -50°C**				
			Longitudinal strip specimen 25,4 mm				Ø	min			
50747K/1	**L360N/X52N**	11324	**392**	**527**	**28,2**		**A) 81**	**92**	**66**	**86**	**81**
							B) 89	**100**	**67**	**100**	
	S355G14/15+N	11309	**398**	**527**	**28,2**	**0,76**	**C) 86**	**86**	**86**	**87**	
							D) 50	**51**	**48**	**51**	

Z99

D01	Visual and dimensional inspection with satisfactory results	X	D51	Hydrostatic test - min. test pressure MPa / sec 100% of each lot	**20,5 / 5**
C50	Flattening test (EN ISO 8492) - satisfactory		D02	The pipes tested on tightness by NDT in acc. to	
C51	Expanding test (EN ISO 8493) - satisfactory				
C52	Bending test (EN ISO 8491) - satisfactory				
C53	Ring expanding test (EN ISO 8495) - satisfactory		D03	Nondestructive Testing Ultrasonic examination	
C54	Ring tensile test (EN ISO 8496) - satisfactory			acc. to **EN ISO 10893-10/11 (U2C) L/T imperfections – satisfactory.**	X

The manufacturer has an established and certified management system according to ISO 9001:2015, ISO 14001:2015, ISO 50001:2011, ISO 45001:2018.

Z99 X continues on page 2/2

Z01 All pipes conform to the above mentioned standards and ordering requirements and agreements.

Z02 Date of issue **3.1.2023/Vo** Tel.:++420 595683644

A01 Liberty Ostrava a.s.
A05 QA Department
Vratimovská 689/117
719 00 Ostrava-Kunčice
Czech Republic

LIBERTY
Liberty Ostrava a.s.
Vratimovská 689/117, 719 00 Ostrava - Kunčice
QA - WORKS INSPECTOR
IDENTIFICATION No. 4

Bc. Petr Pastucha
Work's Inspector
Z02 Validation

E.z. 2574/16/15/P

A02 **Inspection certificate "3.1" (EN 10 204)**

A03 Document No: **20015/23** Page: **2/2**

add. D03) US acc. to EN ISO 10893-8/11 (U2) – laminarity pipe body – satisfactory.
add. D03) US acc. to EN ISO 10893-8/11, laminarity at the ends (up to in distance 25 mm) - satisfactory
Residual magnetic field [mT] max.3 - satisfactory Location Specimen: add C11-13).....1L.
QA System has been subjected to a specific assessment acc. to directive 2014/68/EU, annex I, point 4.3 and AD 2000-Mbl. W0 by TÜV NORD Systems GmbH & Co. KG. Welding process, personnel for welding and NDT are approved acc. to PED 2014/68/EU.
22HRC=99HRBmax.
MANUFACTURER OF BILLETS: LIBERTY OSTRAVA

C71-92	Heat (H) and product (P) chemical analyses (%)																
B07	Heat No.																

	Test results:			MPa	MPa	%				
B07	Heat No.	C00 Specimen No.		C11 Yield Point	C12 Tensile Strength	C13 Elongation	YP/TS	C40-43 Impact Test		C30-32 Hardness

Z02 Date of issue **3.1.2023/Vo**

Tel.:++420 595683644

A01 Liberty Ostrava a.s.
A05 QA Department
Vratimovská 689/117
719 00 Ostrava-Kunčice
Czech Republic

LIBERTY
Liberty Ostrava a.s.
Vratimovská 689/117, 719 00 Ostrava - Kunčice
QA - WORKS INSPECTOR
IDENTIFICATION No. 4

Bc. Petr Pastucha
Work's Inspector
Z02 Validation

E.z. 2574/16/15/P

Manufacturer:
ArcelorMittal Tubular Products Roman S.A.
STEFAN CEL MARE STR., BL 15, SC.A, PARTER I
ROMAN, NEAMT COUNTY

MILL TEST CERTIFICATE

according to EN 10204/3.1/2004

-

Page 1/3

B 20307/3

30.09.2020

ArcelorMittal

Buyer: Brodrene Dahl AS

BRYNSENGVEIENS 5, N-0602 OSLO
NORWAY

SEAMLESS STEEL PIPES

Total weight:	Total Length:	Pieces	Bundles
1.764 tons - lbs	41.35 meters - feets	7	2

Buyer's reference: PO NO: 50087363/10.09.2020

Contract 50004739

Standard: API 5L ed.46-2018- PSL 2; ISO 3183-2019; EN 10225/2009; NACE MR 0175/ISO 15156-1&2-2015; ANSI/NACE MR 0103/ISO 17945-2015; Dahl Specification No.3+MDS C22 rev.5+MDS Y27 rev.4/2017+ MDS Y22 rev.5+ Spec.Norsok

Dimensions: 219.10 x 8.20 mm
-

Schedule: -

Length: 5.80 - 7.00 m
-

-
-

Item	Item Client
2	1093361

Hydro Test:	Bar	PSI	MPa	Time(sec)
	202	-	20.2	5

Steel Grade: X52N/S355G14+N/S355G15+N/L360 N

Chemical Analysis(%)

Heat	Bulletin No.	Product Req.		C	Mn	Si	S	P	Cr	Ni	Cu	As	Al	Mo	V	Nb	Ti	Ca	B	N	Sn	Pb	Sb	Bi
			Max	0.16	1.60	0.45	0.007	0.025	0.25	0.30	0.35	-	0.060	0.08	0.100	0.040	0.020	-	0.0005	0.0140	-	-	-	-
			Min	-	-	0.15	-	-	-	-	-	-	-	-	-	-	-	-	-	-	-	-	-	-
1192972		Heat analysis		0.14	1.22	0.19	0.004	0.010	0.07	0.09	0.14	0.007	0.028	0.01	0.060	0.000	0.003	0.0020	0.0004	0.0060	0.0090	0.0010	0.0020	0.0050
1202570		Heat analysis		0.13	1.25	0.20	0.002	0.009	0.05	0.08	0.14	0.009	0.026	0.01	0.067	0.002	0.003	0.0020	0.0004	0.0060	0.0070	0.0010	0.0020	0.0010
1192972	20-324	Product analysis		0.14	1.22	0.21	0.003	0.008	0.05	0.07	0.15	0.005	0.031	0.01	0.066	0.002	0.001	0.0013	0.0001	0.0055	0.0100	0.0010	0.0000	0.0000
1192972	20-324	Product analysis		0.14	1.20	0.21	0.003	0.007	0.05	0.08	0.15	0.005	0.031	0.01	0.065	0.002	0.001	0.0016	0.0002	0.0055	0.0100	0.0010	0.0000	0.0000
1202570	20-827	Product analysis		0.14	1.25	0.20	0.003	0.010	0.06	0.09	0.13	0.007	0.025	0.01	0.067	0.002	0.003	0.0021	0.0002	0.0063	0.0090	0.0010	0.0000	0.0000
1202570	20-827	Product analysis		0.14	1.24	0.20	0.002	0.010	0.06	0.09	0.13	0.007	0.024	0.01	0.067	0.002	0.003	0.0022	0.0002	0.0065	0.0090	0.0010	0.0000	0.0000

P-2

Chemical Analysis(%)

Heat	Bulletin No.	Product Req.		Al / N	Nb + V	Nb + Ti + V	Cr + Mo + Ni + Cu	CE_IIW
			Max	-	0.080	0.120	0.800	0.43
			Min	2.00	-	-	-	-
1192972		Heat analysis		4.67	0.060	0.063	0.310	0.39
1202570		Heat analysis		4.33	0.069	0.072	0.278	0.38
1192972	20-324	Product analysis		5.64	0.068	0.069	0.280	0.38
1192972	20-324	Product analysis		5.64	0.067	0.068	0.290	0.38
1202570	20-827	Product analysis		3.97	0.069	0.072	0.290	0.39
1202570	20-827	Product analysis		3.69	0.069	0.072	0.290	0.39

CEpcm = C+Si/30+Mn/20+Cu/20+Ni/60+Cr/20+Mo/15+V/10+5B CE_S = C+Mn/6 CE_{IIW} = C+Mn/6+(Cr+Mo+V)/5+(Ni+Cu)/15

We state on our sole responsibility that the delivered products are in conformity with the order requirements.

Quality Control Representative

Formular 12A, rev.9

Item #	Heat #	Code #	Item Text #1	Item Text #2
P-2	1202570			

BRØDRENE DAHL

Manufacturer:
ArcelorMittal Tubular Products Roman S.A.
STEFAN CEL MARE STR., BL 15, SC.A, PARTER I
ROMAN, NEAMT COUNTY

MILL TEST CERTIFICATE

according to EN 10204/3.1/2004

-

B 20307/3

30.09.2020

ArcelorMittal

Buyer: Brodrene Dahl AS

BRYNSENGVEIENS 5, N-0602 OSLO
NORWAY

SEAMLESS STEEL PIPES

Total weight:	Total Length:	Pieces	Bundles
1.764 tons - lbs	41.35 meters - feets	7	2

Standard: API 5L ed.46-2018- PSL 2; ISO 3183-2019; EN 10225/2009; NACE MR 0175/ISO 15156-1&2-2015; ANSI/NACE MR 0103/ISO 17945-2015; Dahl Specification No.3+MDS C22 rev.5+MDS Y27 rev.4/2017+ MDS Y22 rev.5+ Spec.Norsok

Buyer's reference: PO NO: 50087363/10.09.2020

Contract 50004739

Dimensions: 219.10 x 8.20 mm
-

Schedule: -

Length: 5.80 - 7.00 m
-

-
-

Item	Item Client
2	1093361

Hydro Test:	Bar	PSI	MPa	Time(sec)
	202	-	20.2	5

Steel Grade: X52N/S355G14+N/S355G15+N/L360 N

Tensile Test

Heat	Orientation	Length		Width/Diameter		Thickness		Section		Mechanical test Bulletin No.	YS MPa	YS (PSI:1000)	UTS MPa	UTS (PSI:1000)	E %	YS/UTS max: 0.88
		mm	inch	mm	inch	mm	inch	mm²	inch²							
1192972	Longitudinal Flat	50.8	-	40.00	-	8.40	-	336.0	-	20-2743	440.00	-	528.00	-	38.20	0.83
1192972	Longitudinal Flat	-	-	20.00	-	8.80	-	176.0	-	20-1680	437.50	-	539.80	-	34.70	0.81
1202570	Longitudinal Flat	50.8	-	40.00	-	8.80	-	352.0	-	20-2800	428.00	-	535.00	-	38.40	0.80
1202570	Longitudinal Flat	-	-	20.00	-	8.50	-	170.0	-	20-1727	423.50	-	529.40	-	33.00	0.80

Impact Test

Heat	Impact Test Bulletin No.	Orientation	Size (mm)	Temp. (°C)	Req.KV (min. J)	KV values (J)			Req.Avr. (min. J)	Avr. fracture energy (J)	KCU min:-J/cm² T:°C			Shear Area min. %			Lateral Expansion min. mm		
1192972	20-3744	Transversal	10x5x55	-46	15.0	87	105	93	20.0	95	-	-	-	90	90	90	0.74	0.90	0.78
1192972	20-3745	Longitudinal	10x5x55	-50	15.0	121	127	119	20.0	122	-	-	-	90	90	90	1.05	1.10	1.03
1202570	20-3837	Transversal	10x5x55	-46	15.0	67	80	76	20.0	74	-	-	-	85	85	85	0.55	0.66	0.62
1202570	20-3838	Longitudinal	10x5x55	-50	15.0	91	89	103	20.0	94	-	-	-	90	90	90	0.76	0.75	0.86

Hardness Test

Heat	Hardness Test Bulletin No.	HB max.-	HV 10 max.-	HV 10 max.-					HRC max.22
				OD	Midwall	ID	End A	End B	
1192972	20-2372	-	-	-	-	-	-	-	<20
1202570	20-2430	-	-	-	-	-	-	-	<20

We state on our sole responsibility that the delivered products are in conformity with the order requirements.

Quality Control Representative

Manufacturer: ArcelorMittal Tubular Products Roman S.A. STEFAN CEL MARE STR., BL 15, SC.A, PARTER I ROMAN, NEAMT COUNTY	**MILL TEST CERTIFICATE** **according to EN 10204/3.1/2004** -	Page 3/3 **B 20307/3** **30.09.2020**	ArcelorMittal

Buyer: Brodrene Dahl AS BRYNSENGVEIENS 5, N-0602 OSLO NORWAY	SEAMLESS STEEL PIPES	Total weight: 1.764 tons - lbs	Total Length: 41.35 meters - feets	Pieces 7	Bundles 2
Buyer's reference PO NO: 50087363/10.09.2020 **Contract 50004739**	**Standard:** API 5L ed.46-2018- PSL 2; ISO 3183-2019; EN 10225/2009; NACE MR 0175/ISO 15156-1&2-2015; ANSI/NACE MR 0103/ISO 17945-2015; Dahl Specification No.3+MDS C22 rev.5+MDS Y27 rev.4/2017+ MDS Y22 rev.5+ Spec.Norsok				
	Dimensions: 219.10 x 8.20 mm -	Schedule: -	Length: 5.80 - 7.00 m -	-	

Item	Item Client
2	1093361

Hydro Test:	Bar	PSI	MPa	Time(sec)
	202	-	20.2	5

Steel Grade: X52N/S355G14+N/S355G15+N/L360 N

Heat

Heat	Pieces	Length (m)	Weight (kg)
1192972	1	-	-
1202570	6	-	-

Remarks

PIPES IN COMPLIANCE WITH PED: 2014-68-EU/15.05.2014, ANNEX 1, SECTION 4.3.
"Issued in agreement with TÜV SÜD Industrie Service GmbH (07.2008)"
"QS approved acc. to PED, Annex I, Para. 4.3 by Notified Body 0036"
"(Certification no. DGR-0036-QS-W 361/2008/MUC)"
Manufacturing process – hot rolling.
Hot finished, steel is fully killed, fine grained and vacuum degassing, produced by electric furnace, source G300706.
Heat treatment: normalizing at temperature 890-940°C, time soaking 6 min.
Visual inspection and dimensional check without objection.
NDT full body:
- ultrasonic inspection for: longitudinal imperfections, outside & inside surface, acceptance level U2/C (5% of WT)-acc. EN 10893/10-satisfactory.
- detection of laminar imperfection on the pipe body with 100% surface coverage (U3).
NDT for the pipe ends:
-ultrasonic inspection for: longitudinal imperfections, outside & inside surface, acceptance level U2/C (5% of WT)-acc. EN 10893/10-satisfactory.
-detection of laminar imperfection on the pipe body with 100% surface coverage (U3).
Magnetism residual max 30 Gauss.
Hydrostatic test hold for 5 sec. no leakage noticed.
The products was manufactured, sampled, tested, marked and inspected in accordance with the Standards, the supplementary requirements, and any other requirements designated in the purchase order, and has been found to meet such requirements.

We state on our sole responsibility that the delivered products are in conformity with the order requirements.

Quality Control Representative

Appendix B Specimen Fabrication

Attachment 3 – Fabrication Sheet DT Joint

- Made by Atteya (Atteya, to be published)

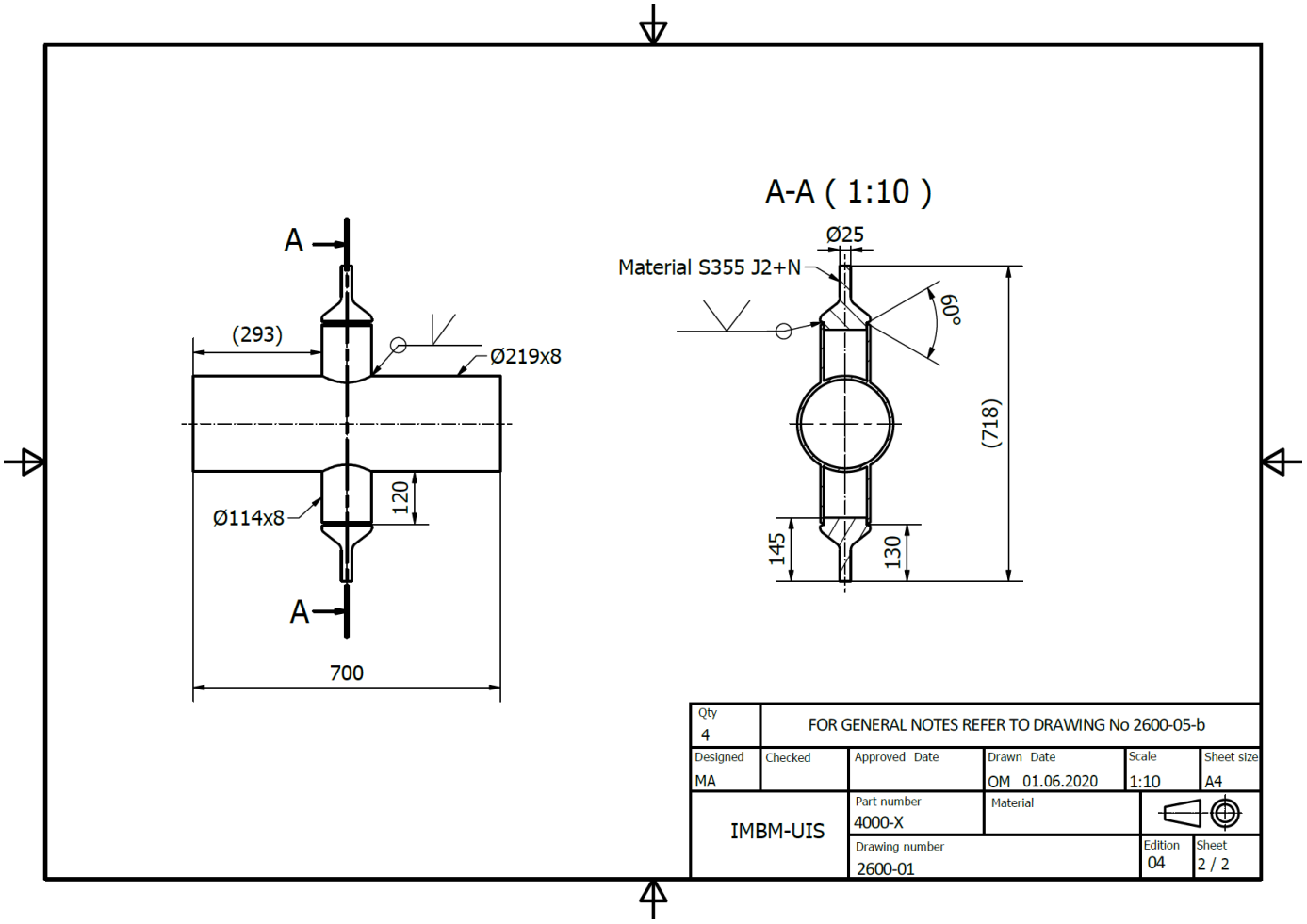

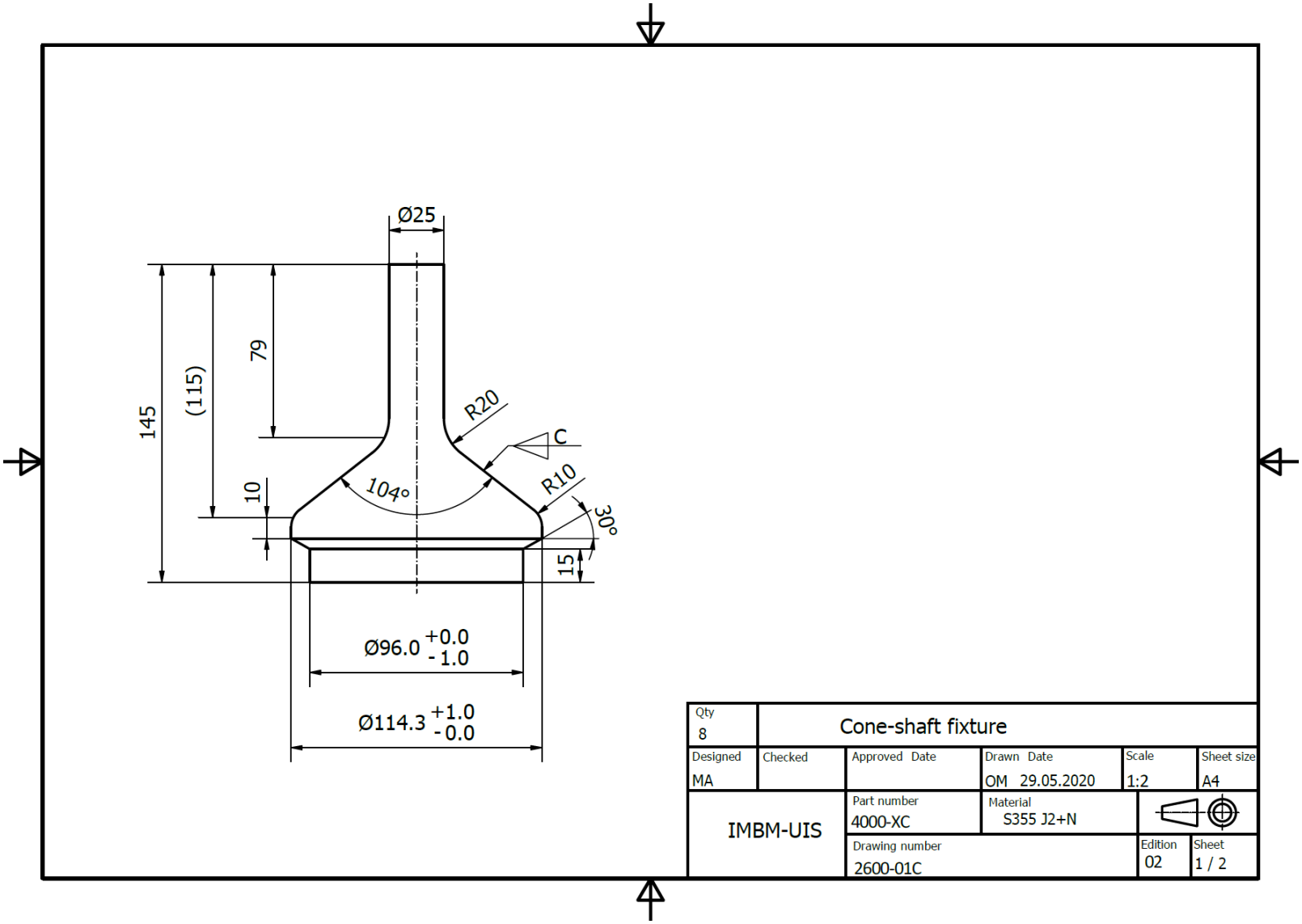

Qty 8	Cone-shaft fixture				
Designed MA	Checked	Approved Date	Drawn Date OM 29.05.2020	Scale 1:2	Sheet size A4
IMBM-UIS		Part number 4000-XC	Material S355 J2+N		
		Drawing number 2600-01C		Edition 02	Sheet 1 / 2

Welding Details

THE WELD PROFILE RADIUS 'R' IS A WELDED SHAPE AND DOES NOT CALL FOR SURFACE GRINDING, UNLESS SPECIFIED ON DESIGN DRAWINGS

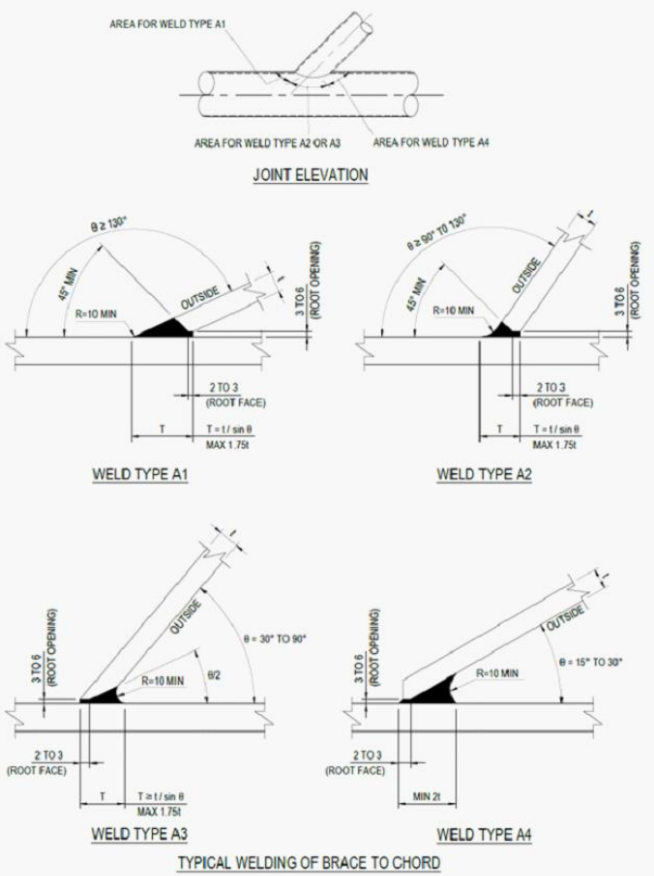

General Notes

All steelwork fabrication, inspection and testing shall generally be in accordance with DNV OS-C401.
All welds shall be in accordance with DNV OS-C401 approved welding procedure.
All structural welds shall be continuous.
All tubular joints shall be framed to a common work point at the intersection of the tubular centerlines
The following non-destructive testing requirements shall apply to all welded joints at brace-chord intersections:
100 % VISUAL, 100 % MPI, 100 % UT
Acceptance criteria for NDT shall be in accordance with DNV OS-C401

Material
If not otherwise specified

Category	Grade
Tubular	S355 G14+N
End plates	S355 J2+N

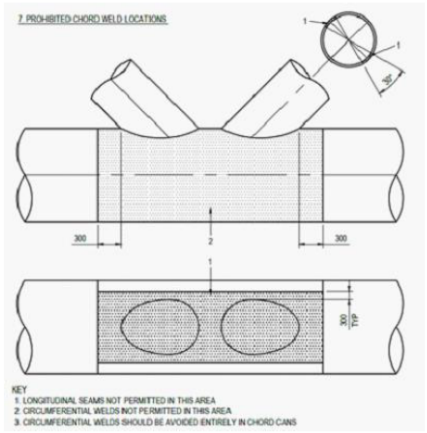

GENERAL NOTES REFER to DRWG No 2600-01, 2600-04

Designed	Checked	Approved Date	Drawn Date	Scale	Sheet size
MA			OM 23.04.2020	1:10	A3

	Part number	Material	
IMBM-UIS			
	Drawing number 2600-05-b	Edition 02	Sheet 3/3

Attachment 4 – Welding and Fabrication Documentation

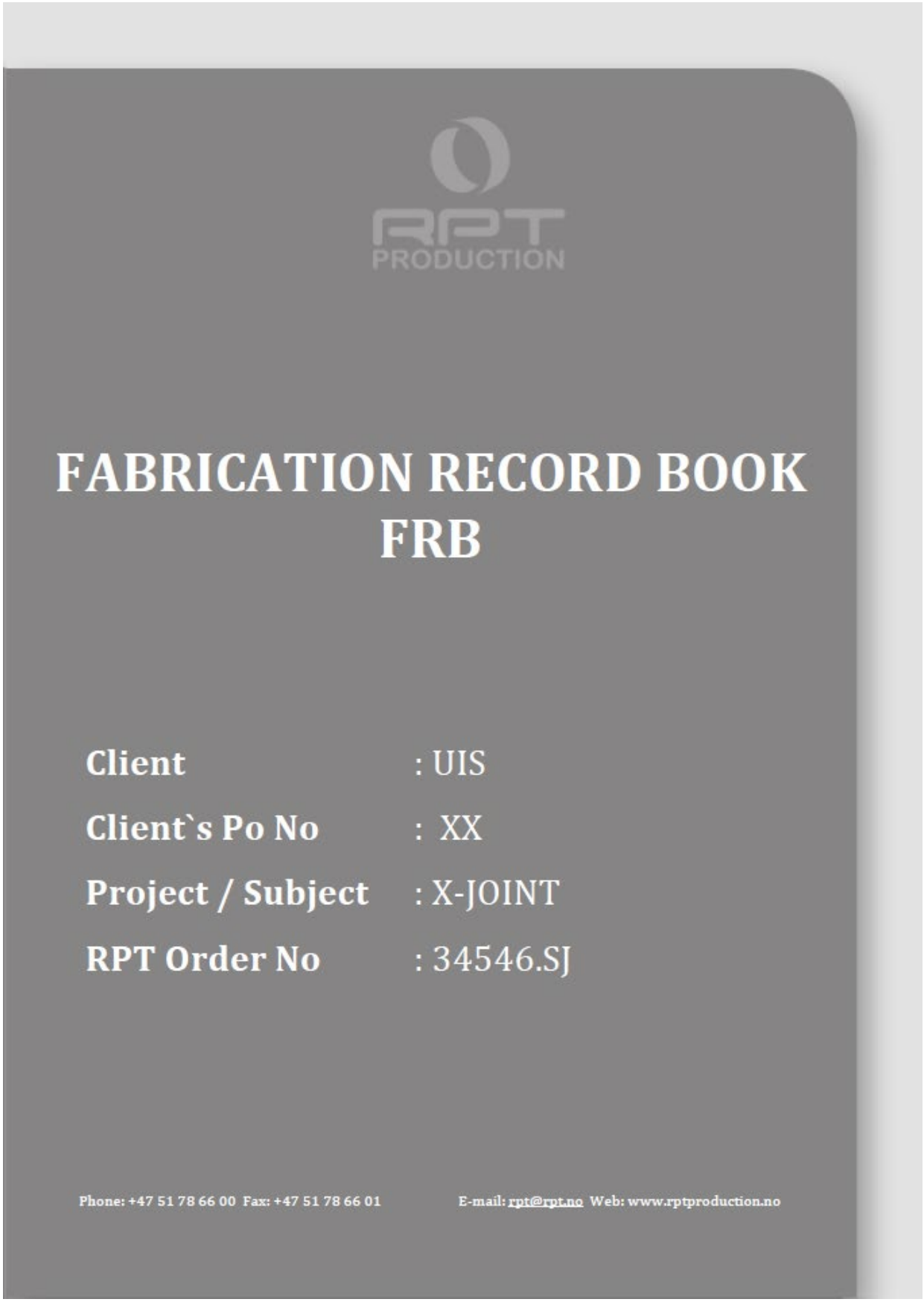

1.	PO	ATTACHED ✓ NA
2.	FABRICATION DRAWING`S	✓ ATTACHED NA
3.	WELD AND NDE LOG	✓ ATTACHED NA
4.	WELDER`S CERTIFCATES	✓ ATTACHED NA
5.	WELDING PROCEDURE	✓ ATTACHED NA
6.	NDE REPORTS	✓ ATTACHED NA
7.	NDE CERTIFICATES	✓ ATTACHED NA

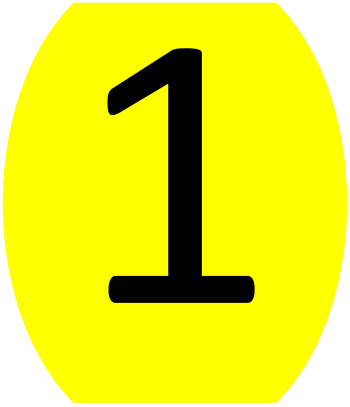
1

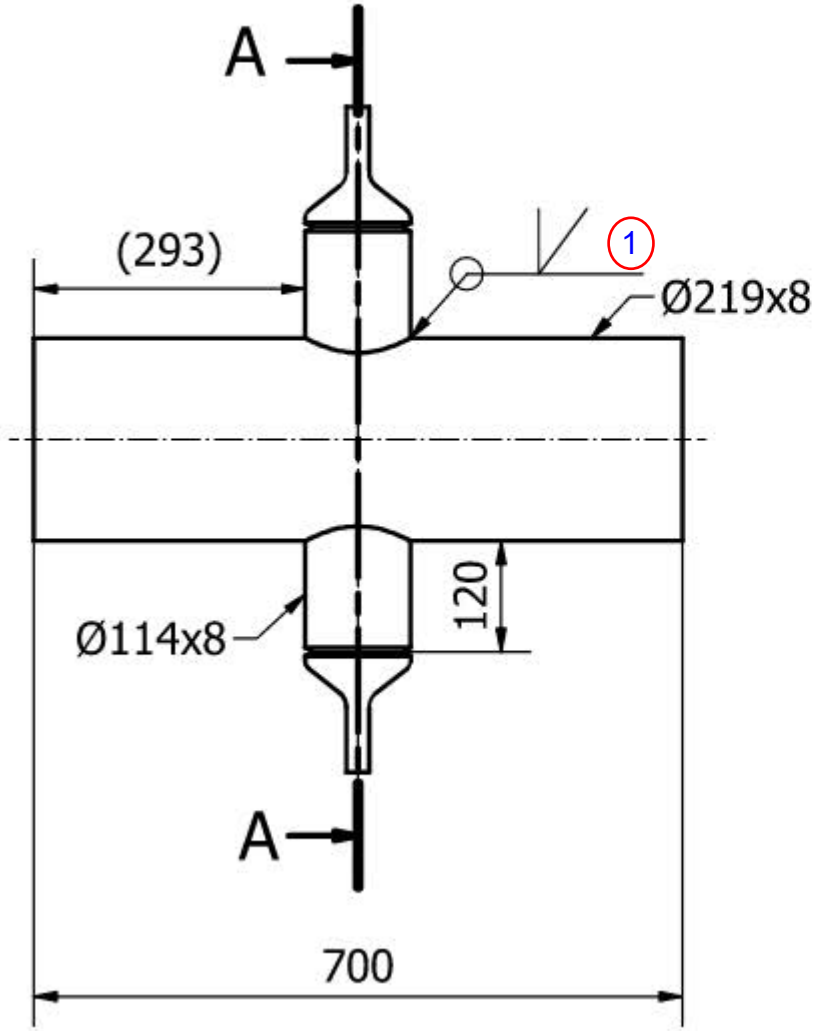

A-A (1:10)

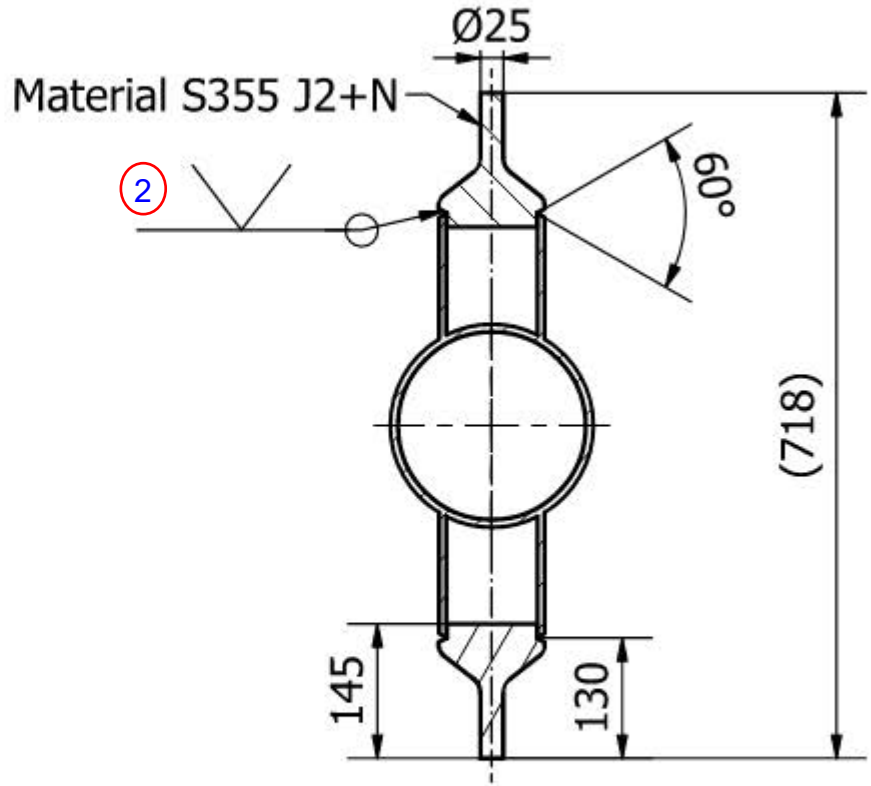

S34546-01

X-JOINT

RPT PRODUCTION

AS BUILT

Dato: 310123 Sign: MZ


2

WELD SUMMARY AND VISUAL INSPECTION REPORT

RPT Ord No.:	S34546	Drawing.:	S34546-01
Client.:	UIS	Prod Spec.:	Norsok / DNV OS-C401 (NDT)
Client`s Po No.:			

INSPECTION INFO			
VT Proc.:	VT 101 Rev.08	RT Proc.:	NA
PT Proc.:	NA	PMI Proc.:	NA
MT Proc.:	MT 103 Rev.3	UT Proc.:	UT 106 Rev.04

				ENGINEERING INFO			PRODUCTION INFO				100 % Visual Inspection				Report Number Reference				
Weld No.	Spool No. / Serial No.	Dia/ Length	Weld Type	NDT % RT / UT	NDT % MT / PT	NDT % PMI	WPS	Wire Heat No.	Weld Date	Welders ID	Acc	Rej	Date	Sign	RT / UT	MT/PT	PMI	VT	COMMENTS
1	SN: S34546-01 / X-JOINT	114	BW	100 %	100 %		103-2	105628	31.01	1025	X		03.02	KT	23-40	23-184		23-146	TYP x 2 PIPE/PIPE
2	SN: S34546-01 / X-JOINT	114	BW		100 %		103-2	105628	31.01	1025	X		03.02	KT	23-40	23-184		23-146	TYP x 2 CONE FIXTURE


3

Welder's Qualification Test Certificate

Sertifikat for sveiser

NS-EN ISO 9606-1:2017

NORSK AKKREDITERING PERS 003

Designation: *Betegnelse:* NS-EN ISO 9606-1:2017 138/136 T BW 1.3 FM2 M/R t12.3 s12.3(3.0/9.3) D168.0 H-L045 ss nb

Welders's name: *Sveisers navn:* Nguyen, Sau Van

ID: *Id* 1025

Issued 1st time: *Utstedt 1. gang:* 1993-10-15

Date, place of birth: *Dato, fødested:* 1972-11-15, Vietnam

Method of identification: *Identifikasjon:* Known

Employer: *Arbeidsgiver:* RPT Production AS

Certificate's ref. no.: *Godkjenningsbevisets ref.nr:* 124095

		Test Piece(s) *Teststykke(r)*		Range of qualification *Godkjenningsområde*
Welding process(es) *Sveisemetode*		138	136	135+138+136
Transfer mode *Lysbueteknikk*		Short Circuit	Spray	135+138:ALL 136:Spray
Plate (P) or Pipe (T) *Plate (P) eller Rør (T)*		T		T+P
Type of weld *Type sveis*		BW		135+138:BW 136:BW+FW (see note 5.4 e)
Supplementary FW test *Tilleggstest for kilsveis*		Nei/No	Ja/Yes	
Material group(s) *Materialgruppe(r)*		1.3		1+2+3+4+5+6+7+8+9+10+11
Welding consumables *Tilsettmaterialer*	**Group** *Gruppe*	FM2	FM2	FM1+FM2
	Type *Type*	M	R	138: S+M 136: R+P+V+W+Y+Z
	Designation *Betegnelse*	MXA 55T / DWA 55L		
Type of current and polarity *Strømart og polaritet*		DC+		
Material thickness (mm) *Godstykkelse (mm)*		t= 12,3		3,0 -
Deposited thickness, s (mm) *Avsettykkelse, s (mm)*		s= 12,3		
s1/s2 thickness (mm) *s1/s2 tykkelse (mm)*		s1= 3,0	s2= 9,3	3,0 - 6,0 3,0 - 18,6
Outside pipe diam. (mm) *Utvendig rørdiam.*		168,0		84,0 -
Welding position *Sveisestilling*		H-L045		PA+PC+PE+PF
Weld details *Sveis detaljer*		ss nb		138:ss nb+ss mb+bs+ss gb+ss fb 136:ss mb+bs
Single or multi-layer *Ett- eller flerlag*				FW: sl+ml
Shielding gases *Beskyttelsesgasser*		M21		M21
Auxiliaries *Annet*				

Notified body no.: *Teknisk Kontrollorgan nr.*
RTPO PED Art. 20

Examiner: *Kontrollinstans:*
TI-Sertifisering

Photo (if required): *Foto (dersom krav):*

Identification of test pieces: *Identifikasjon av prøvestykker:*
VSN

Welding Procedure Specification No.: *Sveiseprosedyrespesifikasjonsnr.:*
IFOS 23

Job knowledge: *Fagkunnskap:*
[X] **Acceptable** *Akseptert* [ ] **Not tested** *Ikke prøvet*

Additional information in enclosures: *Tilleggsinformasjon i vedlegg:*
[ ] **Yes** *Ja* [X] **No** *Nei*

Type of test *Testtype*	**Performed and accepted** *Utført og akseptert*	**Not required** *Ikke påkrevd*
Visual *Visuell*	X	
Radiography *Radiografi*	X	
Ultrasonic *Ultralyd*		X
Magnetic particle *Magnetpulver*		X
Penetrant *Penetrant*		X
Macro/micro *Makro/mikroundersøkelse*	X	X
Hardness *Hardhet*		X
Fracture *Brudd*		
Bend *Bøy*		
Notch Tensile *Strekkprøving med kjerv*		X
Additional tests *Tilleggstester*		X

Date of welding: *Dato for oppsveising* 2019-09-20

Validity of qualification until: *Sertifikatet er gyldig til* 2023-09-20

9.2 Confirmation of the validity (6 months)
9.2 Bekreftelse av gyldighet (6 mnd)

Date *Dato*	**Position/title** *Stilling/tittel*	**Signature** *Signatur*
2021-03-19	Sveisekoord.	Aas
2021-09-20	Sveisekoord.	Aas
2022-03-21	Sveisekoord.	Aas
2022-09-20	Sveisekoord.	Aas

Remarks *Merknader*

9.3 Revalidation of welder qualification
9.3 Fornyelse av sveiserkvalifikasjon

Revalidation method: *Fornyelsesmetode:* b

Date *Dato*	**Prolonged to** *Forlenget til*	**Position/title** *Stilling/tittel*	**Signature** *Signatur*
2021-09-20	2023-09-20	Sert. ansv.	Jan Sletten

Date of issue *Utstedelsesdato* 2019-09-23

Examining body *Godkjenningsorgan* Jan Sletten

Index no.: 137034

This certificate fulfills the requirements of Directive 2014/68/EU Pressure equipment

Produced by WeldEye®

Welder's Qualification Test Certificate

Sertifikat for sveiser

NS-EN ISO 9606-1:2017

NORSK AKKREDITERING PERS 003

Designation: *Betegnelse:* NS-EN ISO 9606-1:2017 141 T BW 1.3 FM2 S t9.0 s9.0 D48.3 H-L045 ss nb

Welders's name: *Sveisers navn:* Nguyen, Sau Van

ID: *Id* 1025

Issued 1st time: *Utstedt 1. gang:* 2005-03-30

Date, place of birth: *Dato, fødested:* 1972-11-15, Vietnam

Method of identification: *Identifikasjon:* Known

Employer: *Arbeidsgiver:* RPT Production AS

Certificate's ref. no.: *Godkjenningsbevisets ref.nr:* 120453

		Test Piece(s) *Teststykke(r)*		Range of qualification *Godkjenningsområde*
Welding process(es) *Sveisemetode*		141		141+142+143+145
Transfer mode *Lysbueteknikk*				
Plate (P) or Pipe (T) *Plate (P) eller Rør (T)*		T		T+P
Type of weld *Type sveis*		BW		BW+FW (see note 5.4 e)
Supplementary FW test *Tilleggstest for kilsveis*		Ja/Yes		
Material group(s) *Materialgruppe(r)*		1.3		142:1.3 141+143+145:1+2+3+4+5+6+7+8+9+10+11
Welding consumables *Tilsettmaterialer*	**Group** *Gruppe*	FM2		FM1+FM2
	Type *Type*	S		141: S+M
	Designation *Betegnelse*	Elgatig 162		
Type of current and polarity *Strømart og polaritet*		DC-		
Material thickness (mm) *Godstykkelse (mm)*		t= 9,0		3,0 - 18,0
Deposited thickness, s (mm) *Avsettykkelse, s (mm)*		s= 9,0		
s1/s2 thickness (mm) *s1/s2 tykkelse (mm)*		s1=	s2=	- -
Outside pipe diam. (mm) *Utvendig rørdiam.*		48,3		25,0 -
Welding position *Sveisestilling*		H-L045		PA+PC+PE+PF
Weld details *Sveis detaljer*		ss nb		ss nb+ss mb+bs+ss gb+ss fb
Single or multi-layer *Ett- eller flerlag*				FW: sl+ml
Shielding gases *Beskyttelsesgasser*		I1		I1
Auxiliaries *Annet*				

Notified body no.: *Teknisk Kontrollorgan nr.*
RTPO PED Art. 20

Examiner: *Kontrollinstans:*
TI-Sertifisering

Photo (if required): *Foto (dersom krav):*

Identification of test pieces: *Identifikasjon av prøvestykker:*
S 5143

Welding Procedure Specification No.: *Sveiseprosedyrespesifikasjonsnr.:*
TI-141-1,3

Job knowledge: *Fagkunnskap:*
[X] **Acceptable** *Akseptert* [ ] **Not tested** *Ikke prøvet*

Additional information in enclosures: *Tilleggsinformasjon i vedlegg:*
[ ] **Yes** *Ja* [X] **No** *Nei*

Type of test *Testtype*	**Performed and accepted** *Utført og akseptert*	**Not required** *Ikke påkrevd*
Visual *Visuell*	X	
Radiography *Radiografi*	X	
Ultrasonic *Ultralyd*		X
Magnetic particle *Magnetpulver*		X
Penetrant *Penetrant*		X
Macro/micro *Makro/mikroundersøkelse*	X	X
Hardness *Hardhet*		X
Fracture *Brudd*		X
Bend *Bøy*		X
Notch Tensile *Strekkprøving med kjerv*		X
Additional tests *Tilleggstester*		X

Date of welding: *Dato for oppsveising* 2019-02-27

Validity of qualification until: *Sertifikatet er gyldig til* 2023-02-27

9.2 Confirmation of the validity (6 months)
9.2 Bekreftelse av gyldighet (6 mnd)

Date *Dato*	**Position/title** *Stilling/tittel*	**Signature** *Signatur*
2021-02-27	Sveisekoord.	Aas
2021-08-27	Sveisekoord.	Aas
2022-02-28	Sveisekoord.	Aas
2022-08-26	Sveisekoord.	Aas

Remarks *Merknader*

9.3 Revalidation of welder qualification
9.3 Fornyelse av sveiserkvalifikasjon

Revalidation method: *Fornyelsesmetode:* b

Date *Dato*	**Prolonged to** *Forlenget til*	**Position/title** *Stilling/tittel*	**Signature** *Signatur*
2021-03-02	2023-02-27	Sert. ansv.	Jan Sletten

Date of issue *Utstedelsesdato* 2019-02-27

Examining body *Godkjenningsorgan* Jan Sletten

Index no.: 133574

This certificate fulfills the requirements of Directive 2014/68/EU Pressure equipment

Produced by WeldEye®


4

RPT PRODUCTION

WELDING PROCEDURE SPECIFICATION (WPS)

WPS No.: RPT 103-2

Date: 09.03.2021 Rev.: 4

Prod. by:	RPT Production as.	Fabricator:	RPT Production
Project:	General	Ref. spec.:	Norsok M101, Q00075
Location:	Orstad	Ref. WPQR:	RPT 25101 rev.0 / RPT 25102 rev.1

Ref. stand: EN-ISO 15614-1

Welding process:	1	141	2	Ar 75% / Co2 25%	3		
Shielding gas types		Argon 99,996%		136			

Purging gas type	Na l/min
Gas trailing shoe	Na l/min
Weaving yes/no	Yes Max: 5 mm
Welding positions	All uphill
Joint type	BW, FW multi pass
Joint preparation	Machining / Grinding
Cleaning method	Solvent degreasing
Backing	Na
Back gouging	Yes if requierd
Flux designation	Na
Flux handling	Na
Tungsten electrode	WC20 / EWLa-2 2,4 mm
Torch angel	70 - 90 °
Stand off distance	10 - 15 mm
Nozzle diameter(s)	12 mm
Tack welding proc.	8-01-TE-0007

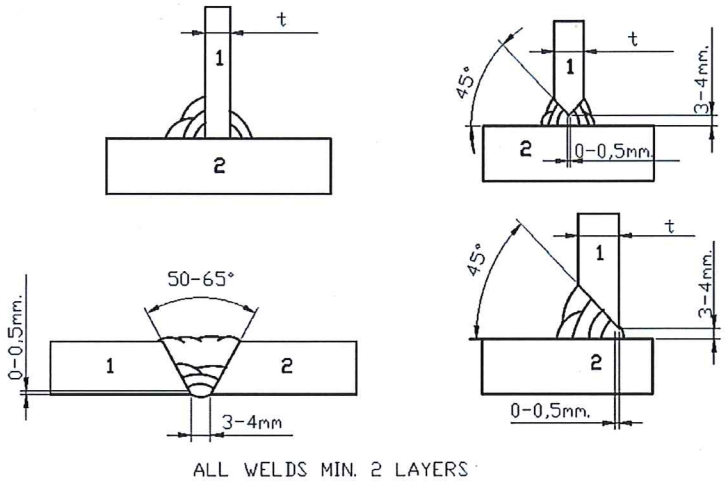

Identification of parent metal

1 C max: CE max: 0,44 PCM max: **2** C max: CE max: 0,44 PCM max:

Part	Name/Grade	Standard	Group	Delivery cond.	Thickness range.(mm)	Diameter range (mm)
1	S355	EN 10025	1.2	Normalized	3 to 50	84 to Plate
2	S355	EN 10025	1.2	Normalized	3 to 50	84 to Plate

Identification of filler metal

Index	Trade name	Classification	Filler handling
A	Boehler Ni 1-IG	EN ISO 636-A-W3Ni1	8-01-TE-0006
B	Boehler Ti 60 T-FD SR	ISO T50 5 1 Ni P M21 1 H5	8-01-TE-0006
C			

Welding parameters

Equipment

Pass no.	Filler metal	Dia. mm	Welding process	Wire feed speed (m/min)	Current (A) min	Current (A) max	Voltage (V) min	Voltage (V) max	Current / polarity	Welding speed mm/min min	Welding speed mm/min max	Run-out lenght (mm)	Gas l/min min	Gas l/min max	Heat input (kj/mm) min	Heat input (kj/mm) max
1	A	2,0	1	-	110	150	12	14	DC-	40	90		16	18	1,4	2,3
2	B	1,2	2	-	170	220	22	26	DC+	140	250		18	20	1,1	1,8
Fill	B	1,2	2	-	180	220	22	28	DC+	140	500		18	20	0,7	2,2
Cap	B	1,2	2	-	170	220	22	28	DC+	150	520		18	20	0,7	1,8

Heat treatment

Method:

Preheat min; 50 ° C Interpass temp.max: 220 ° C Heat treatment proc.: Na Temp.control: Digital

Remarks:

Additional info enclosed (yes/no)

Date: 09.03.2021 Sign.:

Approved

Date:

RPT PRODUCTION
Orstadveien 114, 4353 Klepp St.


5

quality NDT
Orstadveien 112
4353 Klepp stasjon

VISUAL / GENERIC INSPECTION

Doc.Status	Approved
Report	VT-23-146
Purchase Order	I08172/S34546
Date	February 01, 2023
Revision	A

Customer	RPT Production AS	**Customer Address**	Orstadveien 114
Manufacturer	RPT Production	**Q-NDT Project**	SP-27245
Drawing	S34546-01	**Procedure**	VT-101 Rev.08
Acceptance Standard	DNVGL-CG-0051	**Material Quality**	CS
Inspection Extent	100% of welds	**Location**	RPT Production Workshop
Part Number	N/A		
Numbers Of Items Tested	1 ea		
Lighting	≥ 1076 lux		

Weld / Part ID	Status	Comments
Welds	ACCEPT	

N/A

Completed by:	Document Approved By	Client / 3rd Party / Level 3 By Request
Kristoffer Torvund Visual Testing Level 2 12659-N2-V	Even Wiik	
Kristoffer Torvund		

quality NDT
Orstadveien 112
4353 Klepp stasjon

MAGNETIC PARTICLE INSPECTION

Doc.Status	Approved
Report	MT-23-184
Purchase Order	I08172/S34546
Date	February 01, 2023
Revision	A

Customer	RPT Production AS	**Customer Address**	Orstadveien 114
Manufacturer	RPT Production	**Q-NDT Project**	SP-27245
Drawing	S34546-01	**Procedure**	MT-103 Rev.03
Acceptance Standard	DNVGL-CG-0051	**Material Quality**	CS
Inspection Extent	100% of welds	**Location**	RPT Production Workshop
Part Number	N/A		
Numbers Of Items Tested	1 ea		

Joint Type	BW	**Thickness**	Various
Surface	As Welded	**Lighting**	≥ 1076 lux
Weld Process	See weldlog	**WPS**	See weldlog
Magnetic Equipment	Yoke Magnet	**Paint**	Elite WBL5
Powder	Magnetic	**Wet**	X
Dry	N/A	**Black**	Elite BW2
Fluorescent	N/A	**Current**	240V - AC
Field Strength	5 Kg	**Prod Spacing**	75-200mm

Weld / Part ID	Status	Comments
welds	ACCEPT	

N/A

Completed by:	Document Approved By	Client / 3rd Party / Level 3 By Request
Kristoffer Torvund Magnetic Particle Inspection Level 2 12659-N2-M	Even Wiik	
Kristoffer Torvund		

quality NDT
Orstadveien 112
4353 Klepp stasjon

ULTRASONIC INSPECTION

Doc.Status	Approved
Report	UT-23-40
Purchase Order	I08172/S34546
Date	February 01, 2023
Revision	A

Customer	RPT Production AS	**Customer Address**	Orstadveien 114
Manufacturer	RPT Production	**Q-NDT Project**	SP-27245
Drawing	S34546-01	**Procedure**	UT 106 Rev.03
Acceptance Standard	DNVGL-CG-0051	**Material Quality**	CS
Inspection Extent	100% of accessible weld	**Location**	RPT Production Workshop
Part Number	N/A		
Numbers Of Items Tested	1 ea		

Couplant	Elite UT Gel	**Reference / Calibration Block**	Ø 3mm SDH
Evaluation Level	20% DAC	**Thickness**	Various
Heat Treatment	N/A	**WPS**	See weldlog
Surface	As Welded	**Ultrasonic Equipment**	USM Go+ SN: GOPLS20110017. Calibration Date: 02 DEC 2022

Probe	Angle	Frequency	Primary Reference	Transfer Correction	Sensitivity	Range	Result
MSEB 4 / SN: 57462/77324	0°	4Mhz	2nd BWE to 80% FSH	N/A	52 db	0-100mm	ACCEPT
MWB 60-4 SN: 56928-81995	60°	4Mhz	53db	+6 db	+14dB	0-200mm	ACCEPT
MWB 70-4 SN: 56929-90270	70°	4Mhz	55 db	+6 db	+14dB	0-200mm	ACCEPT

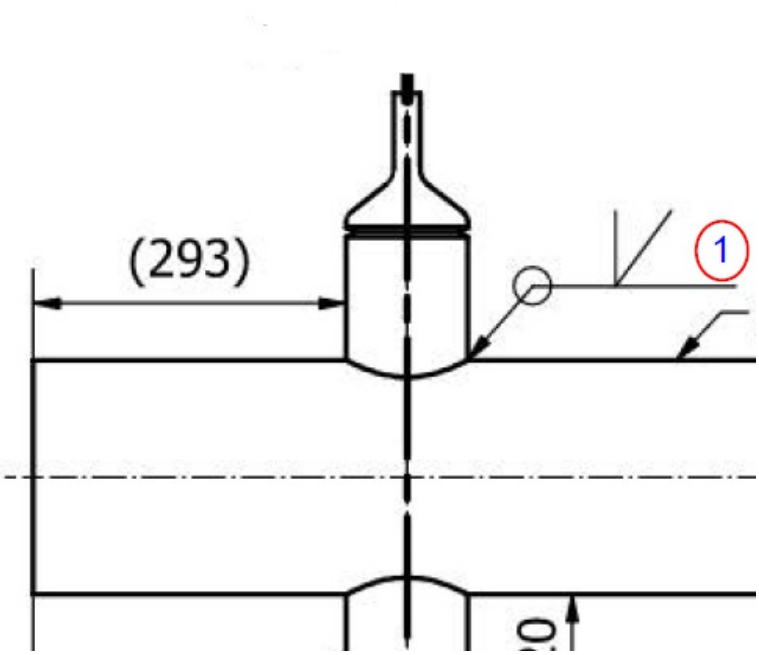

Completed by:	Document Approved By	Client / 3rd Party / Level 3 By Request
Kristoffer Torvund Ultrasonic Testing Level 2 12659-N2-U	Even Wiik	
Kristoffer Torvund		

Appendix C Calculations

References: (Atteya, to be published; British Standard, 2015; DNV, 2019; HSE, 1999; Standard Norge, 2015; Tweed & Freeman, 1987)

Attachment 5 – Fatigue Life Calculation

FATIGUE LIFE CALCULATIONS TUBULAR DT-JOINT

Geometric properties:

Diameter chord: $D := 219\ mm$

Diameter brace: $d := 114.3\ mm$

Thickness chord: $T := 8.5\ mm$

Thickness brace: $t := 8.5\ mm$

Cross-sectional area brace: $A_b := \frac{\pi}{4} \cdot \left(d^2 - (d - 2 \cdot t)^2\right) = (2.825 \cdot 10^3)\ mm^2$

HSS calculation intact DT-Joint:

Load range pre-cracking: $\Delta P := 40\ kN$

SCF Q3 from experimental work: $SCF := 19.4$

Hot spot stress range: $\delta\sigma := \frac{\Delta P}{A_b} \cdot SCF = 274.667\ MPa$

SN T - Curve Design, mean and upper bound:

Design SN T-curve: $T_{desig1}(\sigma) := 10^{(12.48 - 3 \cdot \log(\sigma))}$

Design SN T-curve w/low cycle:

$$T_{desig}(\sigma) := \text{if } T_{desig1}(\sigma) < 100000 \quad \| \; T_{desig} \leftarrow 10^{(23.665 - 7.486 \cdot \log(\sigma))} \quad \text{else} \quad \| \; T_{desig} \leftarrow 10^{(12.48 - 3 \cdot \log(\sigma))}$$

Mean SN T-curve: $T_{mean1}(\sigma) := 10^{(12.95 - 3 \cdot \log(\sigma))}$

Mean SN T-curve w/low cycle:

$$T_{mean}(\sigma) := \text{if } T_{mean1}(\sigma) < 100000 \quad \| \; T_{mean} \leftarrow 10^{(24.8379 - 7.486 \cdot \log(\sigma))} \quad \text{else} \quad \| \; T_{mean} \leftarrow 10^{(12.95 - 3 \cdot \log(\sigma))}$$

Upper bound SN T-curve: $T_{upper.bound1}(\sigma) := 10^{(13.42 - 3 \cdot \log(\sigma))}$

$$T_{upper.bound}(\sigma) := \text{if } T_{upper.bound1}(\sigma) < 100000 \quad \| \; T_{upper.bound} \leftarrow 10^{(26.0107 - 7.486 \cdot \log(\sigma))} \quad \text{else} \quad \| \; T_{upper.bound} \leftarrow 10^{(13.42 - 3 \cdot \log(\sigma))}$$

Result of pre-crack:

Crack initiation: $N1 := 342 \cdot 10^3$

Through thickness crack: $N3 := 1551 \cdot 10^3$

Result of Post-repair 2nd attempt:

Crack initiation +33 hole: $N1_{33} := 93 \cdot 10^3$ *Crack initiation +50 hole:* $N1_{50} := 208 \cdot 10^3$

Through thickness crack +33 hole: $N2_{33} := 145 \cdot 10^3$ *Through thickness crack +50 hole:* $N2_{50} := 250 \cdot 10^3$

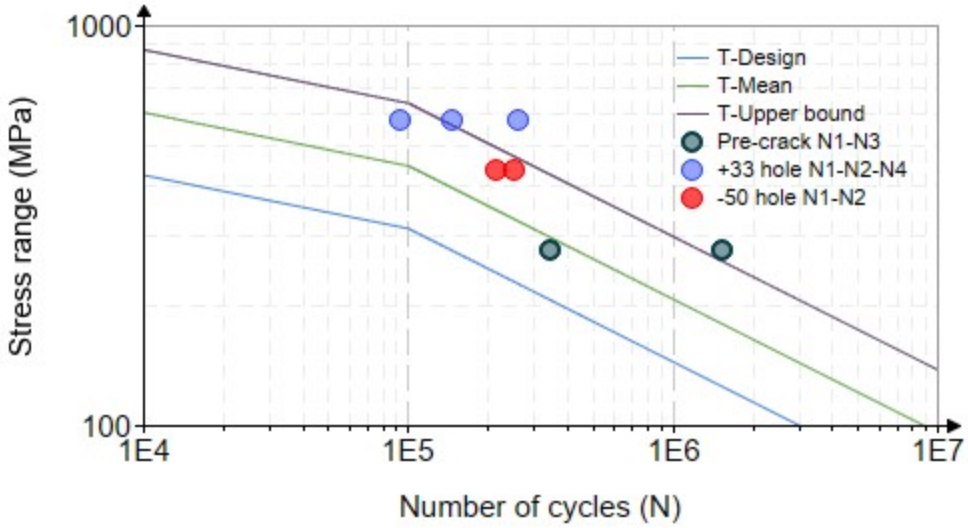

Improved T-Curve due to weld toe grinding according to DNV-RP-C203 and BS 7608

Improved SN DNV-RP-C203: $DNV(\sigma) := 10^{13.909 - 3.5 \cdot \log(\sigma)}$

Improved SN BS 7608: $BS(\sigma) := 10^{14.00 - 3.5 \cdot \log(\sigma)}$

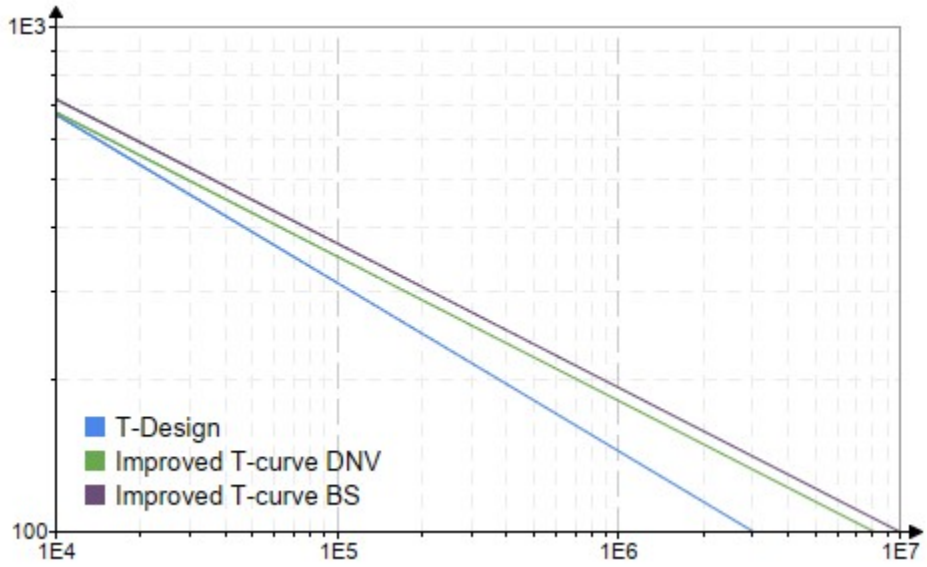

Excepted number of cycles based on DNV and BS for directional and HSS range post-repair:

Maximum radial stress range post-repair: $\delta\sigma_{radial} := 249.5\ MPa$

Maximum principal stress vs directional stress ratio in FE-model: $DFE := 108\%$

Maximum principal stress range: $\delta\sigma_{prin} := \delta\sigma_{radial} \cdot (DFE) = 269.46\ MPa$

Excepted number of cycle based on Radial stress:

Fatigue life T-design: $N_{rd} := 10^{(13.496 - 3 \cdot \log(249.5))} = 2.017 \cdot 10^6$

Fatigue life DNV-RP-C203: $N_{rDNV} := DNV(249.5) = 330.562 \cdot 10^3$

Fatigue life BS 7608: $N_{rBS} := BS(249.5) = 407.618 \cdot 10^3$

Ratio DNV and BS vs Design: $R_{DNV} := \frac{DNV(249.5)}{T_{desig}(249.5)} = 1.7$ $R_{BS} := \frac{BS(249.5)}{T_{desig}(249.5)} = 2.096$

Excepted number of cycles post-repair on basis of SN curve shifted to pre crack:

Fatigue life T shifted to pre-crack: $N_{rub} := T_{upper.bound}(249.5) = 1.694 \cdot 10^6$

Fatigue life DNV-RP-C203: $N_{rubDNV} := N_{rub} \cdot R_{DNV} = 2.879 \cdot 10^6$

Fatigue life BS 7608: $N_{rubBS} := N_{rub} \cdot R_{BS} = 3.55 \cdot 10^6$

Excepted number of cycle based on HSS:

Fatigue life T shifted to pre crack result $N_{rd} := T_{desig}(269) = 155.147 \cdot 10^3$

Fatigue life DNV-RP-C203: $N_{rDNV} := DNV(269) = 254.019 \cdot 10^3$

Fatigue life BS 7608: $N_{rBS} := BS(269) = 313.233 \cdot 10^3$

Ratio DNV and BS vs Design: $R_{DNV} := \frac{DNV(269)}{T_{desig}(269)} = 1.637$ $R_{BS} := \frac{BS(269)}{T_{desig}(269)} = 2.019$

Excepted number of cycles post-repair on basis of SN curve shifted to pre crack:

Fatigue life T shifted to pre crack result: $N_{rub} := 10^{(13.496 - 3 \cdot \log(269))} = 1.61 \cdot 10^6$

Fatigue life DNV-RP-C203: $N_{rubDNV} := N_{rub} \cdot R_{DNV} = 2.636 \cdot 10^6$

Fatigue life BS 7608: $N_{rubBS} := N_{rub} \cdot R_{BS} = 3.25 \cdot 10^6$

Result Post Repair testing 1st attempt:

Surface crack into 50-hole: $Ni1_{50} := 540000$

Surface crack into 30-hole: $Ni1_{30} := 900000$

Through thickness crack 50-hole: $Ni2_{50} := 910000$

Through thickness crack 30-hole: $Ni2_{30} := 930000$

Total number of cycles post repair 1st attempt: $N_{tot} := 3515000$

Number of Cycles after through thickness crack: $N''_{tot} := N_{tot} - Ni2_{30} = 2.585 \cdot 10^6$

The 930 000 cycles post-repair upon reaching through thickness crack into both holes give an equivalent stress range of 135.9 MPa for 977 000 cycles with rain flow counting.

Rainflow counting

```
rainflow(Channel_1_Data);
[c,hist,edges,rmm,idx] = rainflow(Channel_1_Data);
T = array2table(c,'VariableNames',{'Count','Range','Mean','Start','End'});
TT=table2array(T);
% axes 2
xlim([0 1320])
ylim([0 800])
zlim([0 60000])
view([-38 30])
```

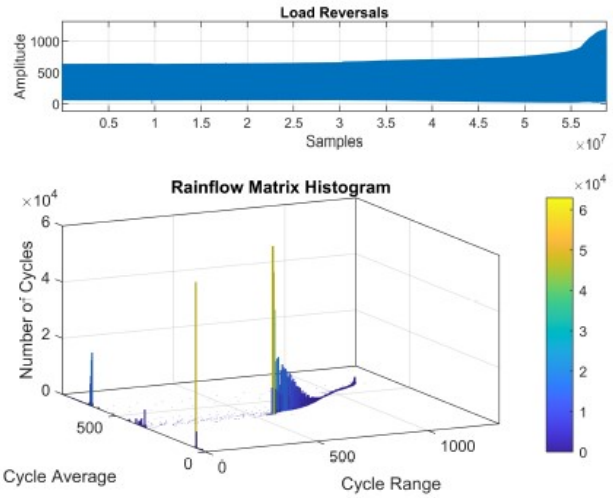


```
Count=TT(:,1);
Range=TT(:,2);
```

Removing cycles with strain range less than 0.3 MPa

```
for i = 1:length(Count);
    if Range(i)<1.45;
        Range1(i)=0;
        Count1(i)=0;
    else
        Range1(i)=Range(i);
        Count1(i)=Count(i);
    end
```

```
end
```

Calculating equivalent strain range (um)

```
ma=3;
Straineq=((sum((Range1.^ma).*Count1))/sum(Count1))^(1/ma)
```

```
Straineq = 693.0641
```

Equivalent stress range and cycle count

```
Cycles=sum(Count)
```

```
Cycles = 977281
```

```
Stresseq = Straineq*0.207
```

```
Stresseq = 143.4643
```

```
rtrtg=sum(Count1)
```

```
rtrtg = 8.3119e+05
```

Calculation of N1 according to OTH 87 259 and Atteya:

For tubular with beta = 0.5 subjected to axial loading, category B can be considered.
The approximate lower bound corresponds to 80th quantile of the entire dataset.

Number of cycles to N3 in experiment: $N3 := 1515000$

Crack length at N1: $c2 := 0.5\ t$

Lower bound estimation: $\frac{c2}{t} = 12 \cdot \left(\frac{N1}{N3}\right)^{3.5}$ $N1 := \left(\frac{c2}{t \cdot 12}\right)^{\frac{1}{3.5}} \cdot N3 = 611036$

N1 estimate according to Clayton: $70 = 100 \cdot \left(1 - \frac{N11}{N3}\right) \xrightarrow{solve, N11} 454500$

N1 estimate according to M. Atteya lower bound: $N1 := \left(\frac{c2}{t \cdot 7}\right)^{\frac{1}{4}} \cdot N3 = 783.214 \cdot 10^3$

N1 estimate according to M. Atteya upper bound: $N1 := \left(\frac{c2}{t} + 0.5\right) \cdot \frac{1}{12} \cdot N3 = 126.25 \cdot 10^3$

Attachment 6 – Burr Diameter Calculation (weld-toe grinding)

WELD TOE DRESSING - BURR DIAMETER CALCULATION (DNV RP C203 and BS 7608)

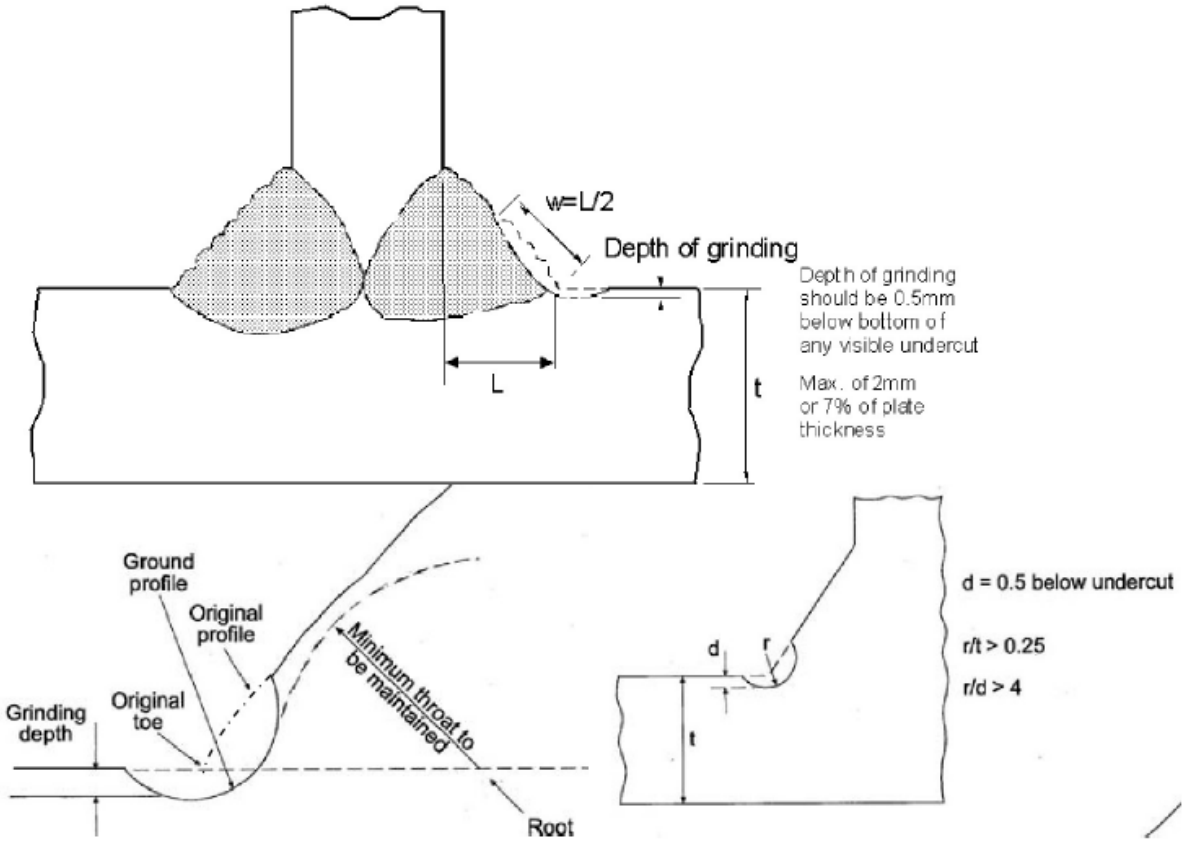

Chord thickness: $t := 8.5\ mm$

Min grinding depth: $d := 0.5\ mm$

Minimum burr radius: $min\_r := 0.25 \cdot t = 2.125\ mm$

Minimum burr radius: $min\_r := 4 \cdot d = 2\ mm$

Maximum depth: $max\_d := 0.07 \cdot t = 0.595\ mm$

Min diameter burr $D := 4.3\ mm$

Attachment 7 – SCF Calculation (DNV RP C203)

SCF - CALCULATIONS TUBULAR DT-JOINT

Geometric properties:

$D := 219\ mm$
$d := 114.3\ mm$
$T := 8.5\ mm$
$t := 8.5\ mm$

$\theta := \frac{\pi}{2}\ rad$
$L := 700\ mm$

$\beta := \frac{d}{D} = 0.522$

$\alpha := \frac{2 \cdot L}{D} = 6.393$

$\gamma := \frac{D}{2 \cdot T} = 12.882$

$\tau := \frac{t}{T} = 1$

$0.2 \le \beta \le 1.0$
$0.2 \le \tau \le 1.0$
$8 \le \gamma \le 32$
$4 \le \alpha \le 40$
$20° \le \theta \le 90°$
$\frac{-0.6\beta}{\sin\theta} \le \zeta \le 1.0$

Stress concentration factors:

SCF - Chord saddle and crown:

$SCF_{c.saddle} := 3.87 \cdot \gamma \cdot \tau \cdot \beta \cdot \left(1.1 - \beta^{1.8}\right) \cdot \left(\sin(\theta)^{1.7}\right) = 20.55$

$SCF_{c.crown} := \gamma^{0.2} \cdot \tau \cdot \left(2.56 + 5 \cdot (\beta - 0.65)^2\right) - 3 \cdot \tau \cdot \beta \cdot \sin(\theta) = 2.839$

SCF - Brace saddle and crown:

$SCF_{b.saddle} := 1 + 1.9 \cdot \gamma \cdot \tau^{0.5} \cdot \beta^{0.9} \cdot \left(1.09 - \beta^{1.7}\right) \cdot \sin(\theta)^{2.5} = 11.346$

$SCF_{b.crown} := 3 + \gamma^{1.2} \cdot \left(0.12 \cdot \exp(-4 \cdot \beta) + 0.011 \cdot \beta^2 - 0.045\right) = 2.417$

Appendix D Crack Mapping

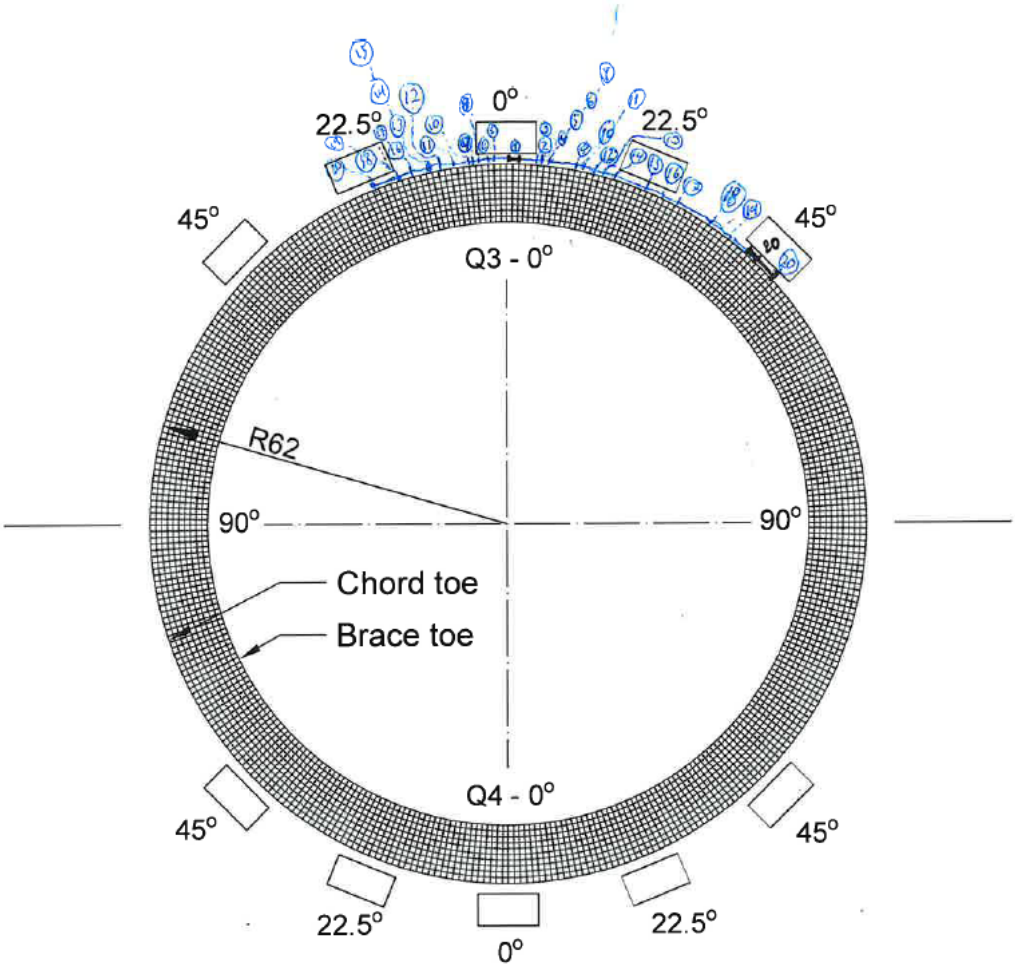

Check No.	Cycles
1	200 000
2	300 000
3	355 000
4	375 000
5	400 000
6	430 000
7	495 000
8	580 000
9	670 000
10	745 000
11	810 000
12	910 000
13	970 000
14	1055 000
15	1170 000
16	1250 000

Comments

17 1330 000

18 1450 000

19 1510 000

~~20 1515 000~~

20 1515 000

CRACK MAPPING - PRE REPAIR
Q3 & Q4

10mm

First detected cracking

Extend of final cracking

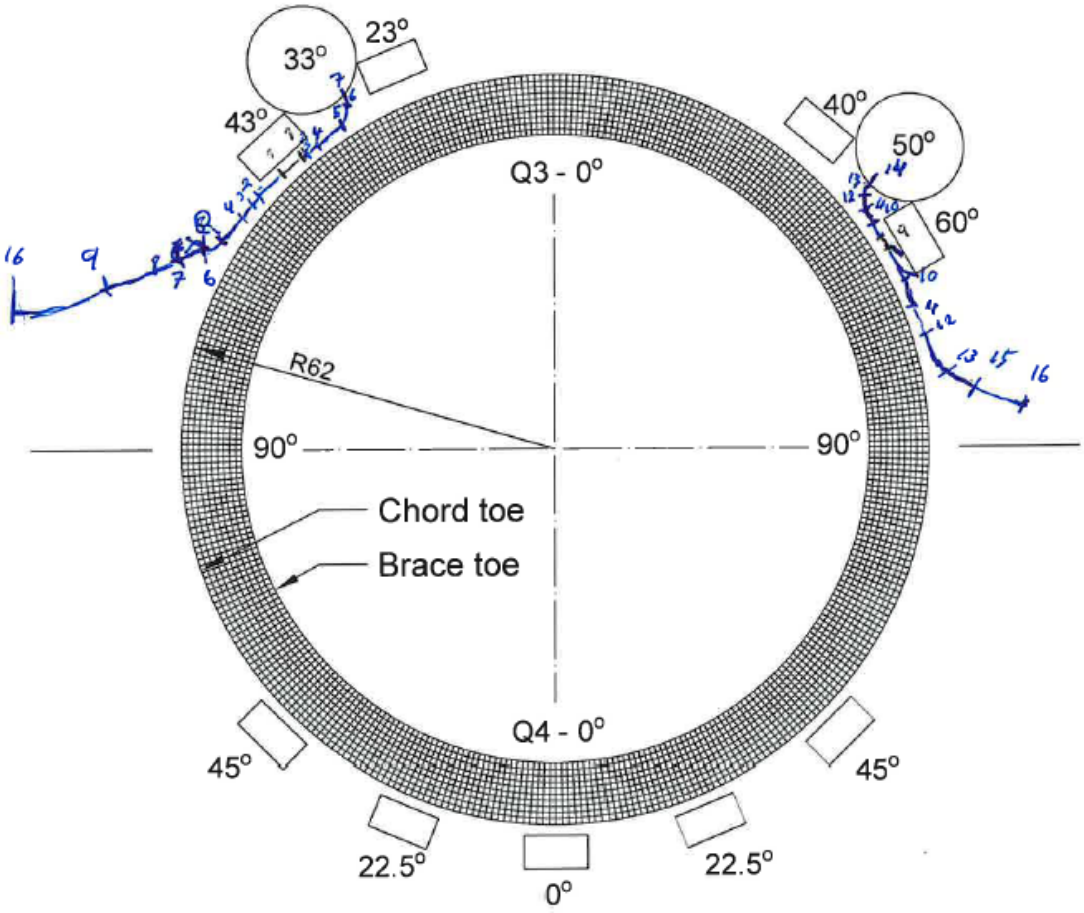

Check No.	Cycles	Comments
1	84 000	
2	98 000	
3	95 000	
4	110 000	
5	120 000	
6	130 000	
7	145000	
8	150 000	
9	198 000	
10	210 000	
11	220 000	
12	236 000	
13	244 000	
14	250 000	
15	260 000	
16		

CRACK MAPPING - POST REPAIR
Q3 & Q4

10mm
First detected cracking
Extend of final cracking